2004

Laser vaporization synthesis of single wall carbon nanotubes

Jeffrey M. Elich

Laser Vaporization Synthesis of Single Wall Carbon Nanotubes

Jeffrey M. Elich

Jeffrey M. Elich

3/12/04

Date

Table of Contents

List of Figures

List of Tables

Acknowledgements

I would like to take this opportunity to thank my advisor, Tom Gennett, for his guidance and help in synthesizing the materials needed to carry out my graduate research. Thank you for never accepting sub-par work, the invaluable scientific discussions, and direction in this thesis project. Above all thanks for being patient; it has truly been a pleasure working in NanoPower thus far.

I'd like to thank my other advisor, Ryne Raffaelle, for constructive critical evaluation of my work. Your perspective as a physicist has helped broaden my scientific knowledge, especially in the areas of semiconductor and solid state physics. I look forward to working with you on more projects in the future.

I wish to thank my committee members, Dr. KSV Santhanam and Dr. Tom Smith. Thank you for your input on my project. Your questions and correspondence at my presentations have helped to define my research experience.

Many thanks to my friends and family, especially my father, who have continued to support me throughout my already extensive college experience. Your help is appreciated more than any words could ever express.

Lastly I'd like to thank my friend and labmate Brian Landi. Your demonstration of leadership and tremendous work ethic has set an impressive example at RIT. Your friendship is truly an asset.

Abstract

The effects of five experimental parameters in pulsed laser vaporization (PLV) synthesis of single wall carbon nanotubes (SWNTs) were examined. Parameters investigated include the laser beam raster pattern, reactor chamber temperature, graphite particle size in the target, reactor chamber configuration, and incident laser beam power density. The type and quality of resultant SWNTs synthesized were strongly influenced by altering these experimental conditions. This information can then be utilized to allow the experimentalist to exhibit a considerable degree of control over the physical and chemical properties of the as-produced SWNT materials. Characterization of the SWNT products was achieved using a combination of Raman spectroscopy, thermogravimetric analysis, UV-Vis-NIR spectroscopy and scanning electron microscopy.

SWNTs synthesized using the corner to corner type laser beam raster pattern have pronounced differences in contrast to those synthesized using a linear type raster pattern. Smaller SWNT diameters result from use of a corner to corner raster pattern. Production rate of SWNT material is doubled using a one shot corner to corner raster pattern versus a one shot move linear raster pattern. These results indicate that there is a diminution of metal enrichment at the target surface was observed using the corner to corner raster pattern due to a reduction of induced localized heating of the target. Increasing reactor chamber temperature produces SWNTs with larger diameters. SWNT yields within the as-produced material increase with increasing temperature up to 1100°C. Defect densities are decreased with increasing temperature. Smaller graphite particle sizes give higher SWNT yields. An increase in reactor chamber volume increases SWNT yield. Increasing power densities result in a decrease in SWNT diameters. By carefully controlling the power density in combination with raster pattern the amount of graphite in the final product can be minimized.

1.0 Introduction

The study of single wall carbon nanotubes (SWNTs) has been an intense area of research in the past decade. Since the independent discovery of SWNTs by Iijima[1] and Bethune[2] in 1993 there has been considerable progress made in elucidating the properties and applications of SWNTs. The empirical and theoretical electrical and mechanical properties of SWNTs make them especially attractive materials for use in a vast array applications.[3-9] Various synthetic methods have been developed for producing these materials.[1,10-12] A number of initiatives to obtain purified SWNTs have given rise to a variety of purification procedures.[13-19] Numerous techniques have been used to characterize both as-produced raw soot products and purified nanotubes.[20] In recent years, a number of devices that integrate SWNTs as one of the component materials have been fabricated.[21-24] Research in the field of carbon nanotubes has increased tremendously over the past few years and has assumed an integral role in the developing field of nanotechnology.

1.1 General Background

1.1.1 A Brief Historical Overview

Interest in the study of nanostructured forms of carbon began in 1985 with the discovery of the buckminsterfullerene by Kroto et. al.[25] Prior to the discovery of fullerenes, the only known ordered allotropic forms of carbon were diamond and graphite. Figure 1 displays a 3D representation of the structure of diamond, graphite, and some "new" forms of carbon.[26] Fullerenes have been extensively studied[27] and the Nobel prize in chemistry in 1996 was awarded for the discovery and research pertaining to these materials. Fullerenes of various sizes, including C_{60}, C_{70}, and others, were identified and

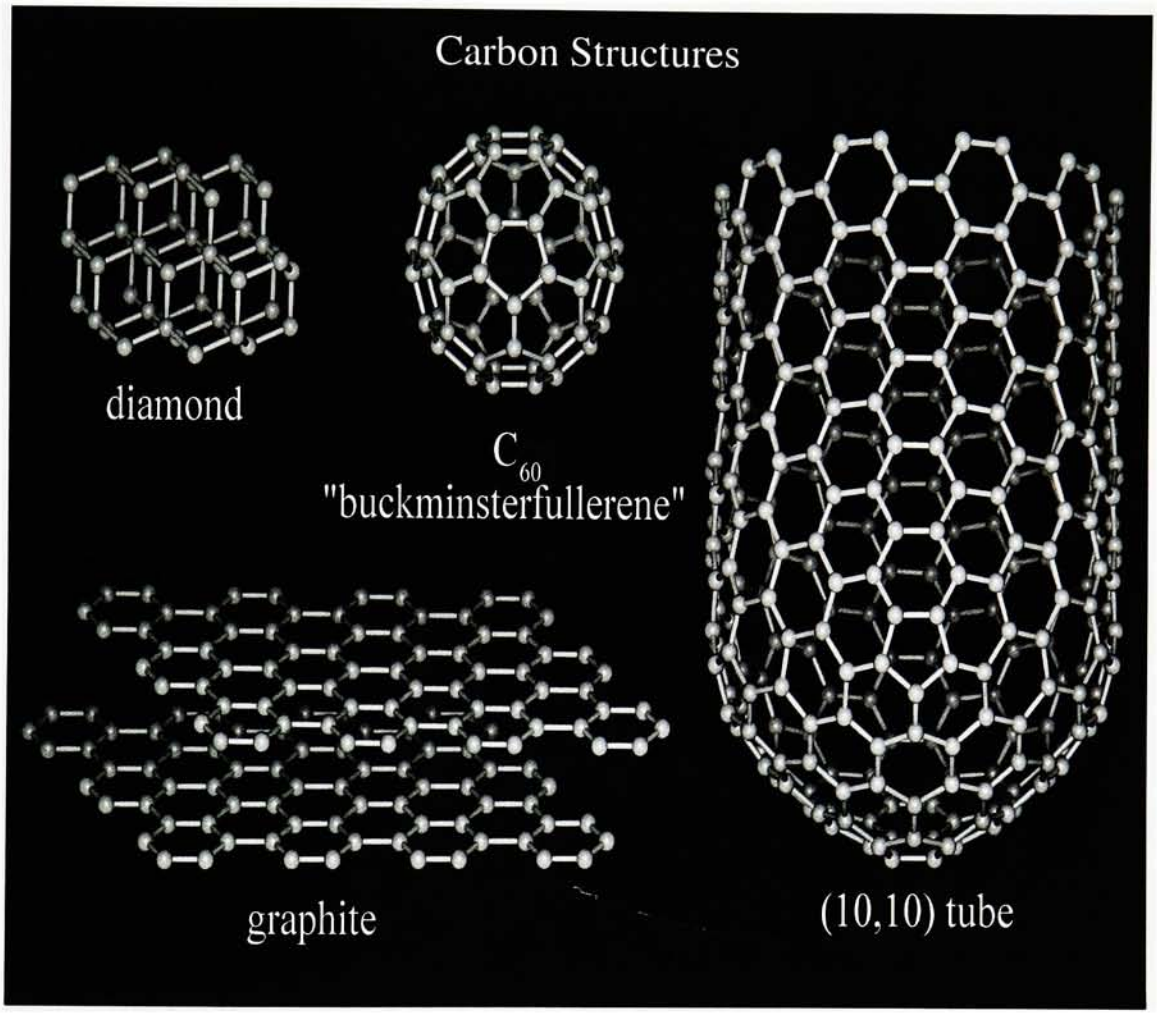

Figure 1: 3D representations of some ordered allotropes of carbon.[26]

characterized. Spherical concentric layers of graphitic carbon, sometimes called nanoonions, were discovered in 1992.[28] Nanoonions are epitaxially layered and, ideally, contain no open or dangling bonds. Some of these nanoonions were found to have an innermost core diameter corresponding to that of C_{60}.

The first example of tubular nanostructured carbon, multi wall carbon nanotubes (MWNTs), were discovered in 1991 by Iijima who used an electric arc discharge synthesis technique.[29] MWNTs are essentially concentric layers or shells of cylindrical graphene sheets with closed fullerene-like caps at the ends of the cylinders. A TEM micrograph of an MWNT is shown in Figure 2. It was recognized by many scientists that these "helical microtubules of graphitic carbon" had remarkable potential due to their unique properties. MWNTs have been studied extensively since their discovery.[30] There was also a great deal of theoretical work carried out on nanotubes. Many of these theoretical studies were performed with consideration of only one layer of a carbon nanotube.[31-34] Theoretical predictions of the properties and behavior of a single, capped, cylindrical shell of graphene were carried out even though they had yet to be synthesized.

SWNTs were discovered independently by two different groups in 1993.[1,2] As with the discovery of MWNTs, an arc-discharge synthesis method produced the first empirical evidence of SWNTs. The arc-discharge technique was the only known method to produce nanotubes until 1995 when Guo et. al. synthesized SWNTs using a laser vaporization technique.[10] A third method for synthesis of SWNTs was developed by Dai et. al. in 1996 who used a chemical vapor deposition (CVD) approach.[11] The ability to perform CVD syntheses on a larger scale led to the HiPco (High Pressure carbon monoxide) procedure being developed in 1999.[12] Efforts have been made toward

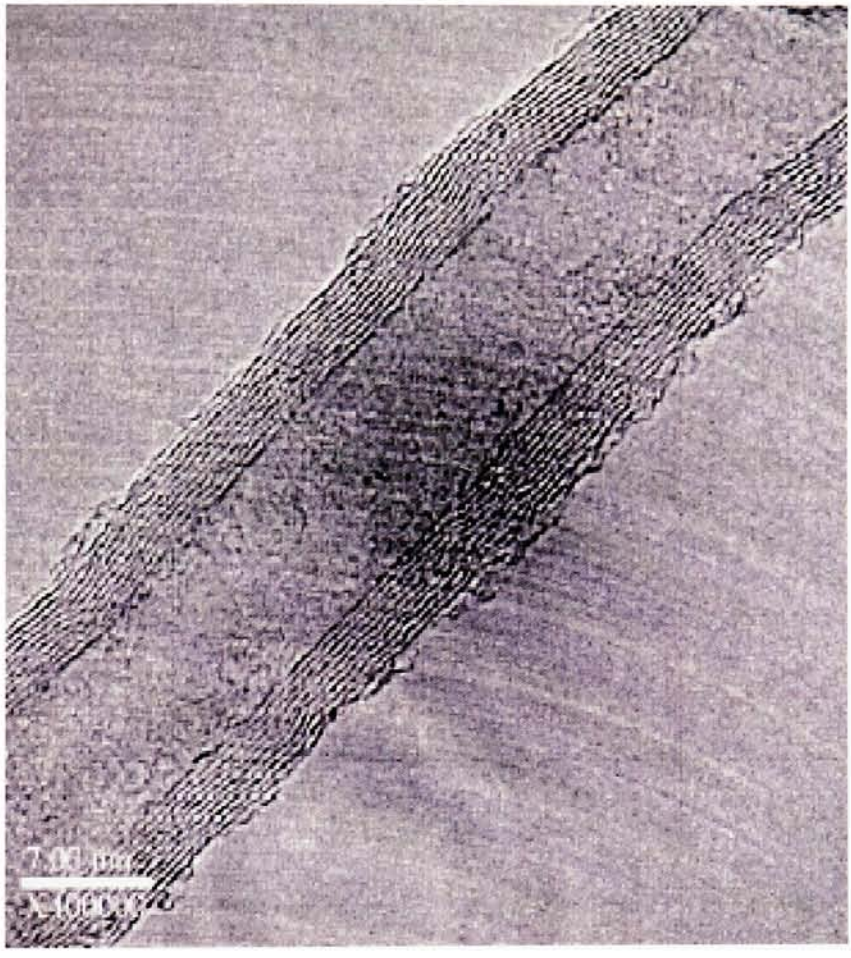

Figure 2: High Resolution TEM micrograph of an MWNT.

the optimization of all types of nanotube synthesis. The experimental details as well as advantages and disadvantages to each synthetic technique are discussed in section 1.2.

1.1.2 Properties of Single Wall Carbon Nanotubes

SWNTs have received a great deal of attention in the scientific community because of their unique physical properties. These physical properties are a direct result of their chemical structure. The structure of a single wall tube can be described as a single layer of graphite, also called graphene, rolled into an elongated tube such that the edges of the graphene sheet line up to produce a continuous cylindrical structure with no "dangling bonds." The rolled up graphene sheet has a hemispherical cap at each end that resembles half of a fullerene, resulting in a closed tubular SWNT structure. This description of SWNTs does not represent the true mechanism of assembly, however, it is meant to schematically represent the nanoscale structure. In an ideal case all carbon-carbon bonds in these structures are sp^2 hybridized resulting in a structure of many hexagons, but only 12 pentagons. Ideal fullerene and closed nanotubular structures will have exactly 12 pentagons, in accordance with Euler's formula.[35] Figure 3 depicts some SWNTs along with their corresponding fullerene caps.

Just as there is variation in sizes of fullerenes, SWNTs similarly vary in both length and individual nanotube diameter. Ideally, the diameter of a nanotube will be equal to the diameter of the corresponding fullerene cap. For example, if a nanotube were to have a diameter of 0.71nm then the corresponding cap would look like half of a C_{60} molecule, which also has a diameter of 0.71nm. As-produced batches of SWNTs typically have a distribution of diameters. The range of nanotube diameters and the frequency of each diameter within the distribution depend on the synthetic technique used

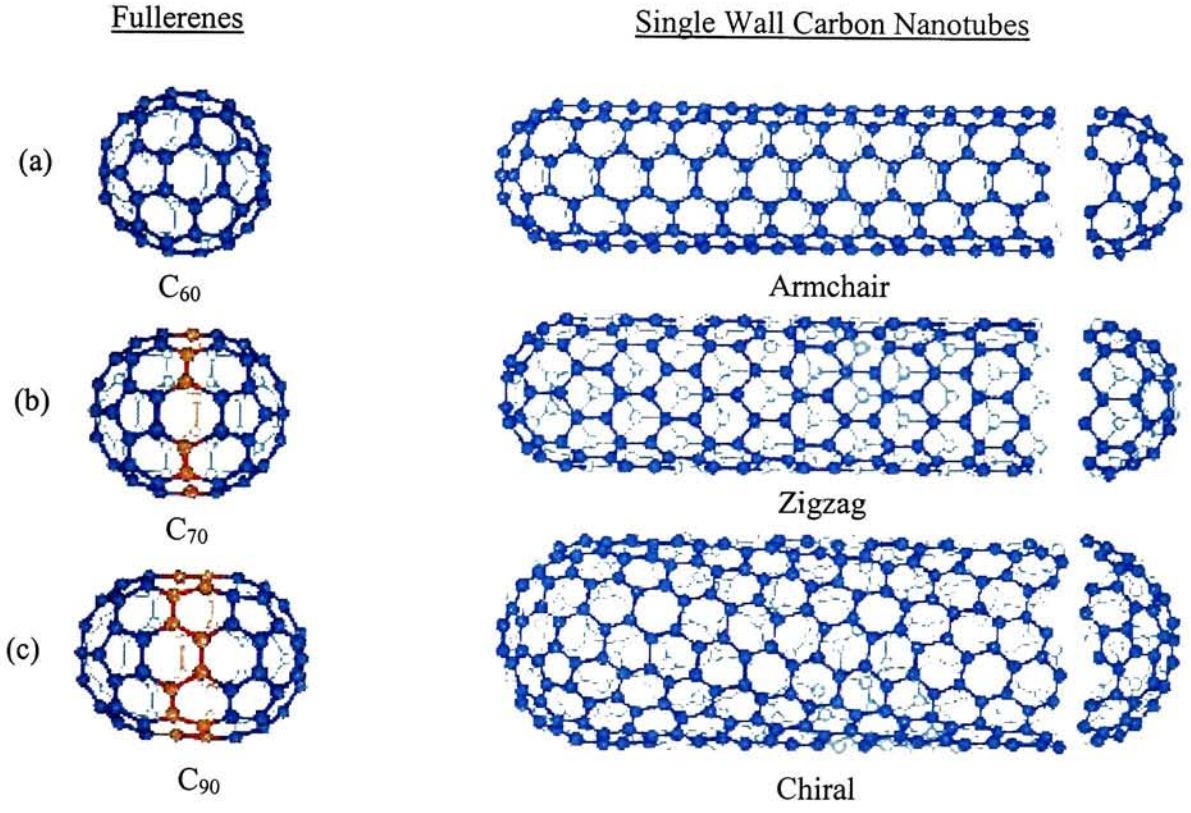

Figure 3: Schematic representation of fullerenes (left) and SWNTs (right) – The SWNTs have half of a fullerene as a cap with many carbon atoms inserted between the caps in a graphene sheet-like manner. The variation in size and chirality is also depicted.[27]

and the experimental parameters associated with that technique. The reported range of SWNT diameters is 0.4 nm to 5.6 nm.[36,37] Although the SWNT diameters are on the order of one nanometer, the lengths have been reported of up to hundreds of micrometers. The five orders of magnitude difference results in a very high aspect ratio. Due to the large aspect ratio SWNTs are often considered to be one-dimensional carbon systems[27] (compared to 2D graphite, 3D diamond, or 0D fullerene carbon systems).

The manner in which a nanotube is "rolled-up" is referred to as its chirality. Figure 4 demonstrates the different chiralities possible for SWNTs. Each individual nanotube has a chiral vector, C_h, defined within a graphene plane. This chiral vector is defined in terms of its unit vectors, a_1 and a_2, and its chiral angle θ. The equation which mathematically describes this vector is:

$$C_h = na_1 + ma_2$$

Where n and m are integers on the axes for the representative vectors.[27] It is conventional to describe a SWNT by its n and m integers or (n,m) designation. Representations of the chiral designations that are assigned to SWNTs are depicted in Figures 3 and 4. All SWNTs fit the description for one of three categories based on their chirality. If the (n,m) designation is such that n = m then it is classified as an armchair nanotube (Figure 3a); if (n,m) is (n,0) then the result is a zigzag nanotube (Figure 3b); other (n,m) combinations result in a chiral nanotube (Figure 3c). Figure 5 is a representation of these types of nanotubes and how they are rolled-up along a graphene sheet. An important ramification of chirality is that some nanotubes display metallic behavior while others display semiconducting behavior. If the (n,m) designation is such that (n-m)/3 is equal to an integer or zero then that nanotube will possess metallic

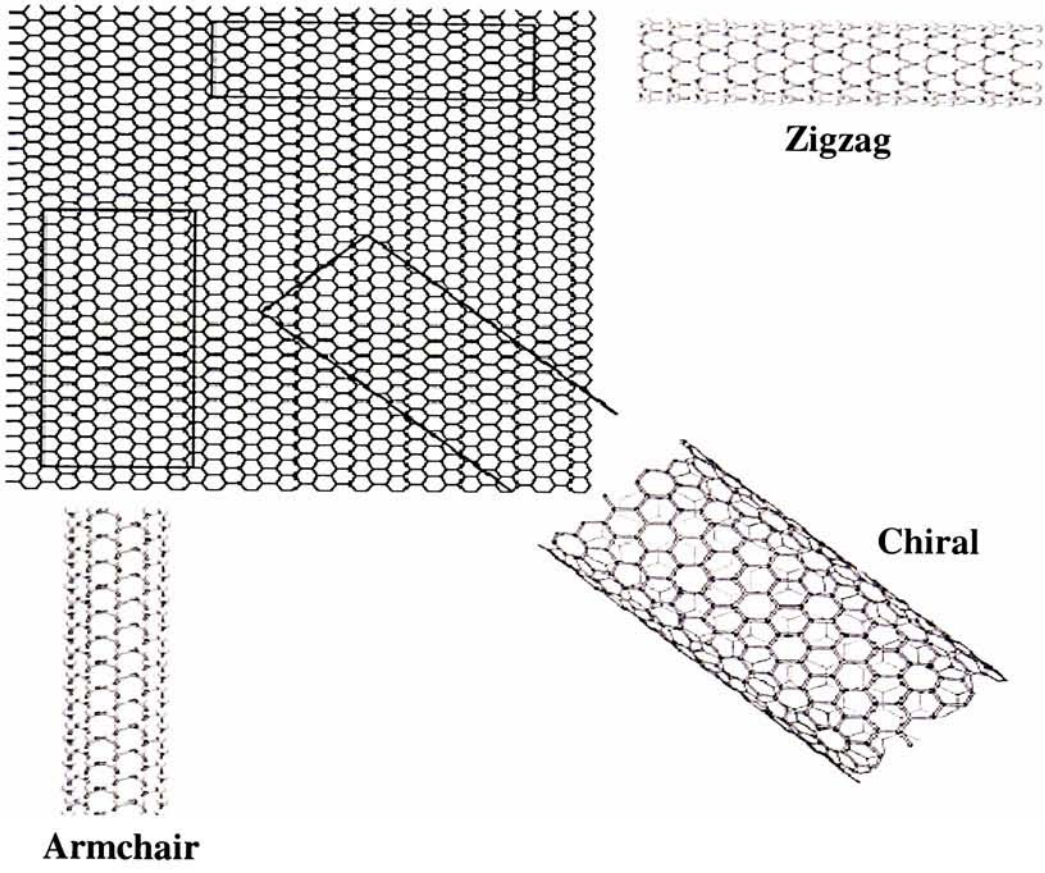

Figure 4: Representation of the three chirality classes of SWNTs – The manner in which they are said to be "rolled-up" from a graphene sheet is depicted.[27]

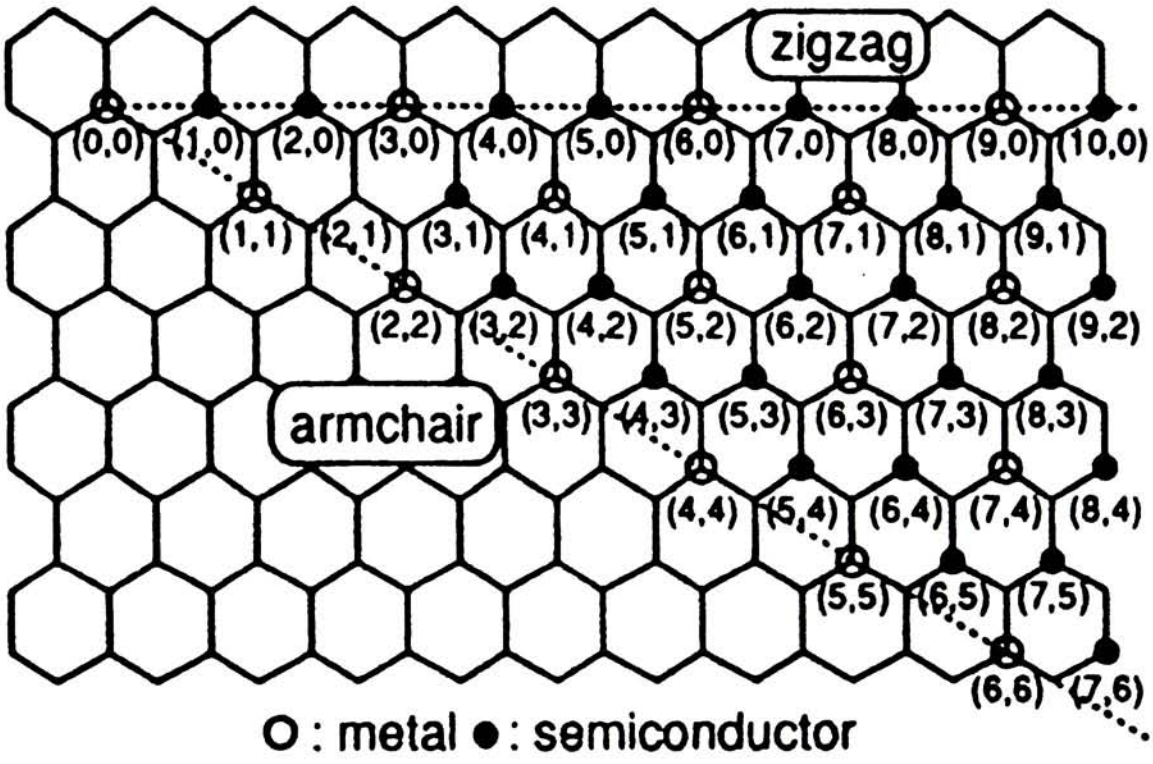

Figure 5: Graphene sheet with chiral vectors available – The integers (n,m) are shown. Chiral angle, θ, is measured from the zigzag axis. Metallic SWNTs will result when (n-m)/3 is equal to an integer value, otherwise semiconducting nanotubes will result.[27]

properties.[27] SWNTs with metallic properties are predicted to be ballistic conductors of electricity due to the delocalization of electrons in the conjugated π molecular orbitals. In other words, very little energy is required to promote electrons from the valence band to the conduction band. If (n-m)/3 is not an integer or zero then that nanotube will possess semiconducting properties. Semiconducting SWNTs require energy to promote electrons from the valence to conduction band. The importance of the metallic and semiconducting behavior of SWNTs is strongly manifested in their electronic properties.

The intermolecular forces of attraction between individual SWNTs cause a "bundling" of the nanotubes held together by Van der Waals interactions. SWNT bundles can contain a wide range of numbers of individual nanotubes. The average spacing between individual nanotubes in a bundle is 0.315 nm.[4] Figure 6 shows a TEM image of a representative bundle. Larger bundles, up to 1 μm in diameter were recently demonstrated.[38] The bundling behavior of SWNTs is in contrast to the behavior of MWNTs. Bundling of MWNTs is not observed. Interestingly the spacing between the coaxial layers in MWNTs is 0.34 nm, which is similar to the reported value of spacing between SWNTs in bundles.

Studies have indicated that SWNTs display interesting mechanical properties that could be useful in a number of applications. Since they consist of entirely sp^2 hybridized carbon atoms, with the typical carbon-carbon bond strength of 152 kcal/mol, a high degree of mechanical strength would be expected for these elongated structures. Indeed, work by Li et. al. resulted in an estimate of the tensile strength for an individual SWNT to be 22.2±2.2 GPa, which is 10-100 times greater than that of common steels.[39] Similarly, the Young's modulus of an individual SWNT has been reported to be on the

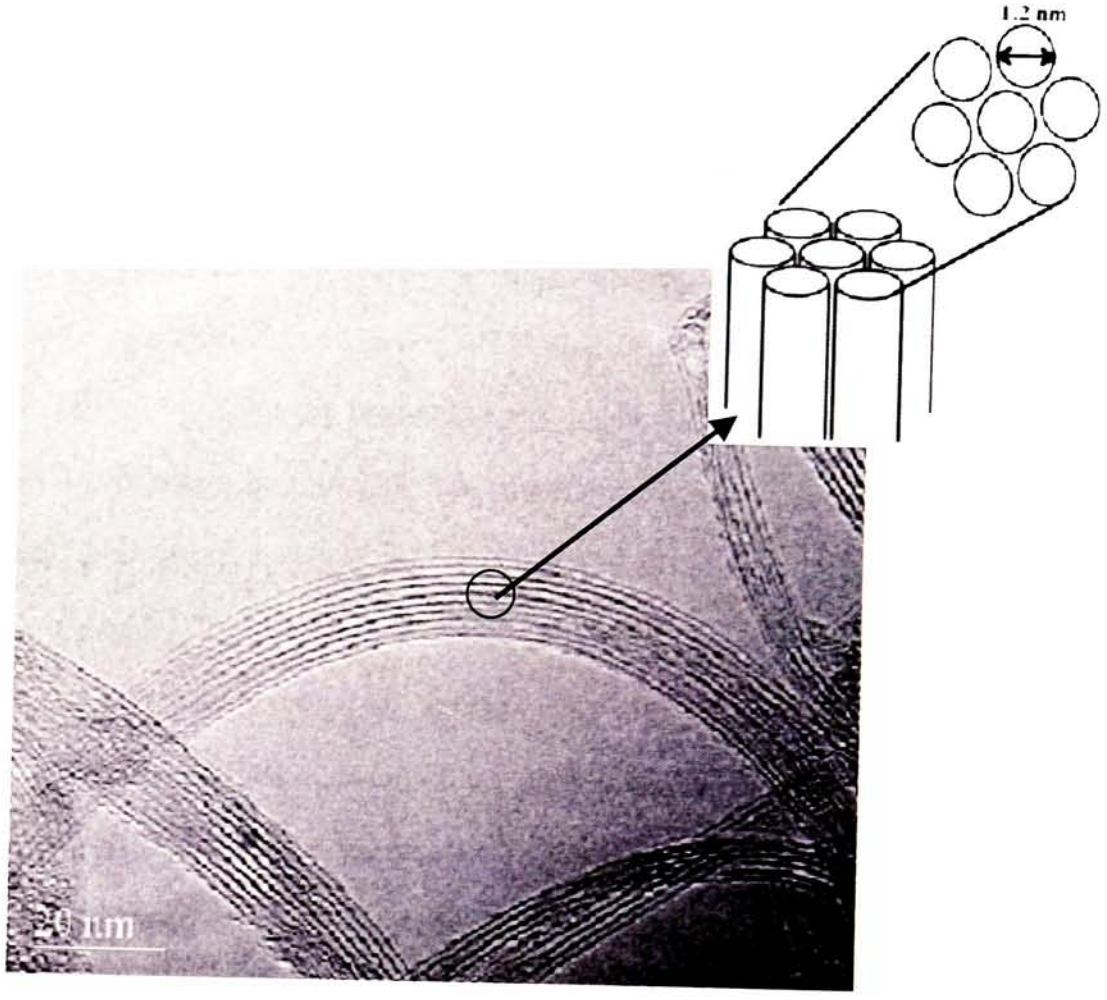

Figure 6: High resolution TEM image of an SWNT bundle.

order of 1TPa which is an order of magnitude higher than that of carbon fibers. As a consequence, SWNTs display considerable mechanical strength and will withstand large amounts of strain in the axial direction. In the lateral direction, however, these material are not brittle, but rather are quite flexible and will not easily undergo structural deformation from lateral stresses. In fact SWNT bundles are usually found intertwined and randomly tangled with one another.

SWNTs will almost always contain defects within their chemical structure. The types of defects include missing carbon atoms and Stone Wales defects. Missing carbon atoms result in "dangling bonds" on the SWNT structure. Stone Wales defects consist of carbon atoms in a heptagon-pentagon pair adjacent to one another, where normally there should be two hexagons.

1.2 Synthetic Methods

The various synthetic techniques that have been developed for SWNT synthesis can usually be classified in one of three general categories of arc discharge[40], chemical vapor deposition (CVD)[11], and laser vaporization[41]. Efforts to optimize these techniques used to produce SWNTs have been made, with respect to yield and purity, by investigation of the synthetic parameters involved. Presently there is no technique that will produce phase pure, monodisperse, or impurity free SWNTs. All syntheses give mixtures of chiralities, diameters, and lengths of SWNTs in the final product. Currently a major goal in production is to develop a synthetic technique that yields exclusively metallic or semiconducting SWNTs. Similarly, the as produced materials always contain some amount of impurities whether it is in the form of amorphous or graphitic carbon, metal catalyst particles, or both. Efforts are also being made toward syntheses that

require no purification of as-produced materials.[40] Variations in certain synthetic parameters, however, can influence SWNT type, yield, and production rate. There are also certain advantages and disadvantages associated with each technique with respect to yield, production rate, diameter distribution, and defect density.

1.2.1 Arc Discharge Synthesis

SWNTs were discovered by Iijima using the arc discharge method.[1] There have since been many subsequent studies incorporating experimental variations in the arc discharge technique to synthesize SWNTs.[42,43] Figure 7 shows the schematic of a typical arc discharge synthesis apparatus. In general, arc synthesis is carried out in a bell jar under 500 torr of an inert atmosphere. Using two graphite rods, one of which serves as the anode and is lightly doped with catalyst metal, and the other that serves as the cathode. Some common metal dopants used are various mixtures of Ni, Co, or Y ranging anywhere from 0.5 at. % to 5 at. % and above. Other catalysts that have successfully catalyzed SWNT growth include Rh, Pd, and Pt.[44] Typically there is a 1 mm gap between the two graphite rods with a voltage of 20-25 V across the rods with a current of 50-100A. During synthesis the anode is consumed and the raw soot product is deposited at the cathode. Most arc syntheses produce SWNTs with diameters ranging from 1-2 nm.[45] The smallest thermodynamically stable nanotube, with a diameter of 0.4 nm, was synthesized using arc discharge.[46] The most significant advantage of the arc discharge method is the large production rates that are attainable which can be as high as 1 g per minute.[40] The most serious drawback to this technique, however, is that the SWNT yield within the raw soot is quite low, on the order of 1% w/w. Figure 8 displays a TEM image of raw soot obtained from arc discharge synthesis.

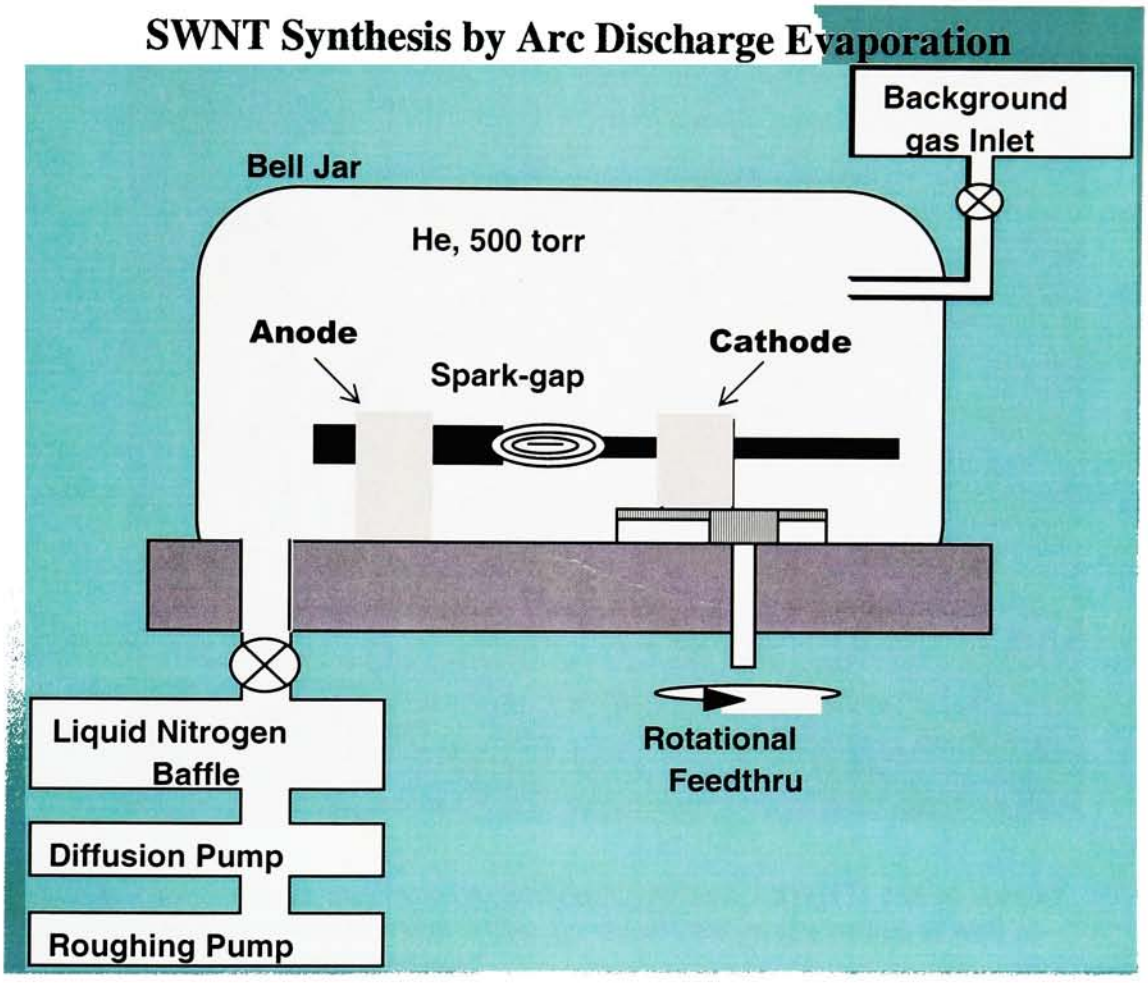

Figure 7: Typical arc discharge apparatus. The graphite rod at the anode is evaporated and material containing SWNTs is deposited at cathode.

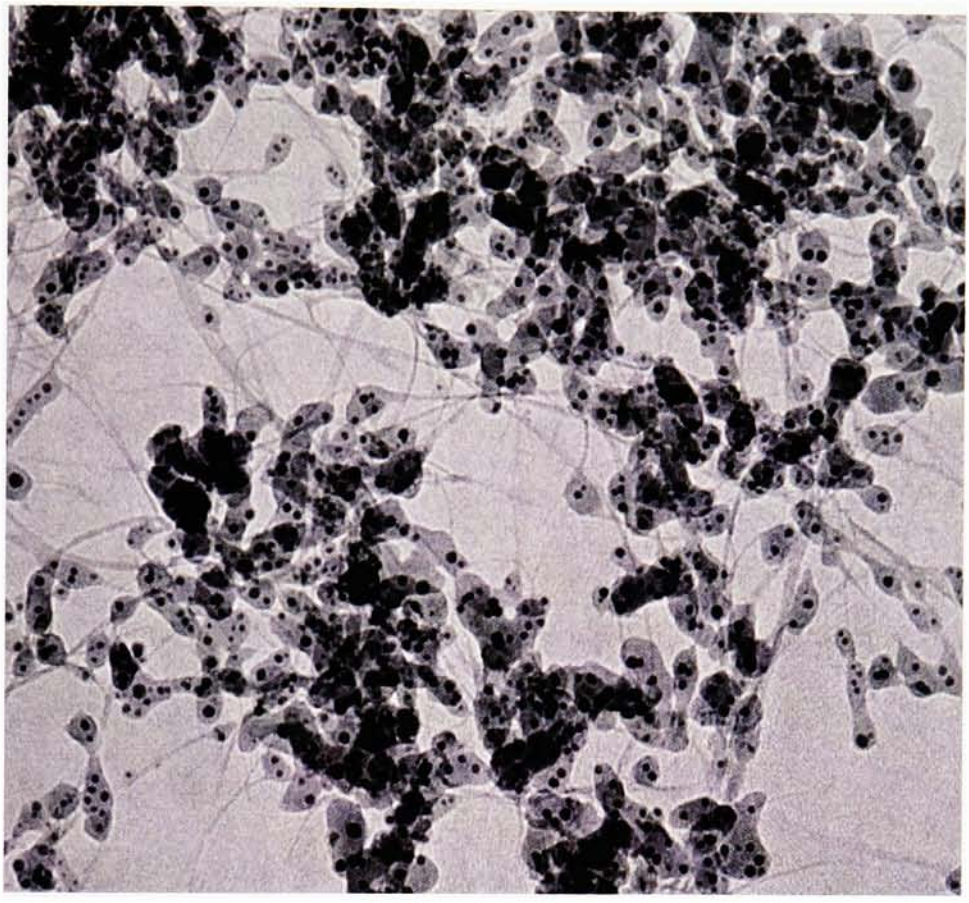

Figure 8: TEM image of arc discharge generated raw soot – SWNTs can be seen as threadlike material. Also visible are metal catalyst impurities as well as amorphous carbon clusters.

Purification of arc discharge SWNTs has shown to be a challenging objective. Encapsulated metal particles are often difficult to remove even if removal of the large amounts of undesired carbonaceous material is achieved. One successful method has been reported where size exclusion chromatography (SEC) was used.[47] It was reported that both purification and segregation according to length of nanotubes was possible using SEC. A more conventional method was recently reported using nitric acid treatment, water rinse, rotary evaporation, ultrasonic treatment, and finally an anneal.[15] This method developed by Huang et. al. produces greater than 98% w/w SWNTs and it was observed that alignment of the nanotubes was possible. A unique method developed by Harutyunyan et. al. employs using microwave radiation to induce heating and oxidation of metal catalyst followed by reflux in HCl.[13] It was reported that this purification method achieved 99.8%w/w SWNTs.

1.2.2 Chemical Vapor Deposition Synthesis

Chemical vapor deposition synthesis has been extensively studied and a wide range of experimental parameters have been investigated with this technique.[48-54] In general the process involves passing a flowing gaseous carbon feedstock over a catalytic substrate where upon carbon nanotubes are grown as decomposition products. A typical CVD synthesis apparatus is shown in Figure 9. Elevated temperatures are usually necessary for growth and range from 675-1200°C during the deposition. The choice of catalyst used to promote SWNT growth will affect the temperature range under which effective growth occurs. Typically, with catalysts such as Ni, Co, and Fe deposition temperatures are between 850-1000°C, however, Hornyak et. al. showed that using a Fe/Mo binary system that SWNT growth could occur at temperatures as low as 675°C.[53]

SWNT Synthesis by CVD

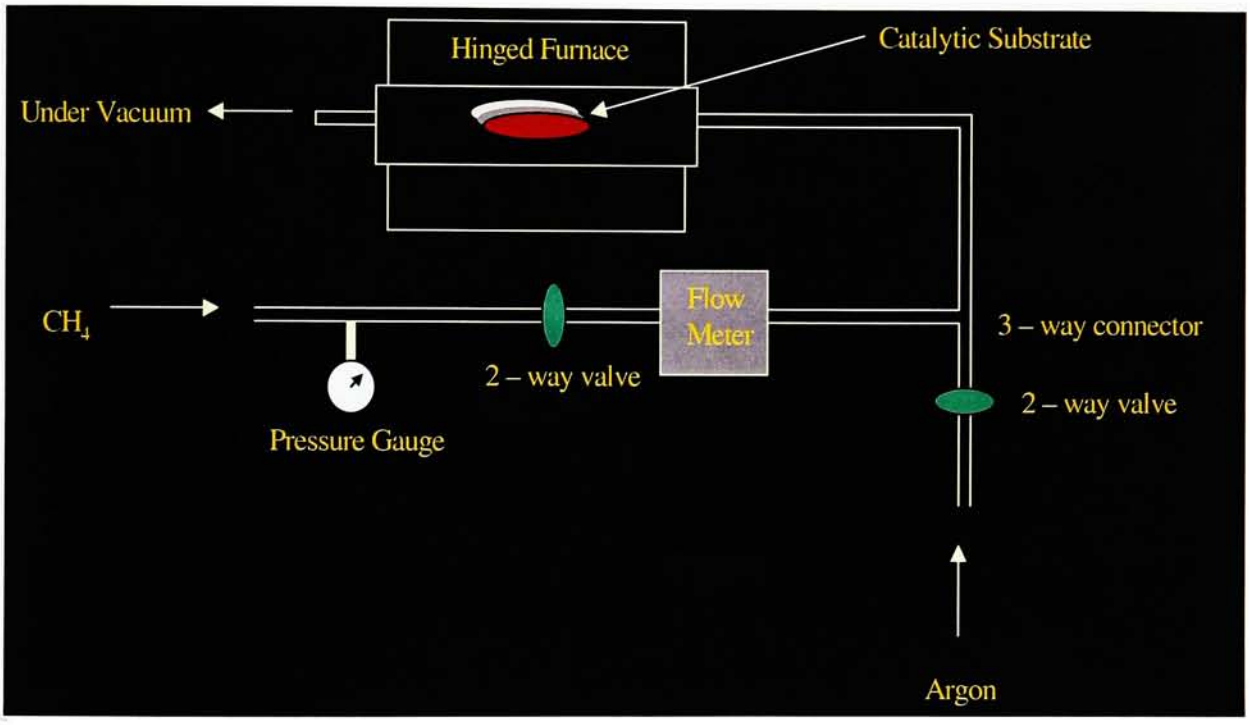

Figure 9: A common CVD apparatus. A carbonaceous feedstock (ie: methane gas) is introduced into the system under an inert atmosphere. SWNT self-assembly occurs on the catalytic substrate.

The first report of SWNTs produced using CVD used Mo catalyst at 1200°C.[11] This approach offered the first example of synthetic approach using pre-formed catalyst particles. The size of these pre-formed catalyst particles was reported to control the diameter of SWNTs produced. Similarly, preferential growth of SWNTs over MWNTs occurred because larger catalyst particles were "onionated," or rendered inactive, during the synthesis. There have since been a number of studies performed on the nature of catalyst or substrate surface and its roll in CVD synthesis.[48,51,52,55-59] A TEM image of as-produced material synthesized by CVD is displayed in Figure 10.

A CVD synthesis using the disproportionation of carbon monoxide, now known as the HiPco process, was developed in 1999.[12] The HiPco process is a "continuous-flow process" that uses $Fe(CO)_5$ catalyst for CO disproportionation. SWNTs produced by the HiPco process are now commercially available. The advantage of the HiPco process that allows its material to be commercially available is the ability to "scale up" production.

1.2.3 Laser Vaporization Synthesis

Synthesis of SWNTs by laser vaporization was first carried out in 1995 by Guo et. al.[10] This method of synthesis uses a laser to vaporize material from a solid carbonaceous target doped with metal catalyst. The vaporized material is transported away from the target via an inert carrier gas, it condenses as solid product, and it is finally collected. SWNTs are present within this collected product after a successful synthesis. A typical reactor chamber consists of a cylindrical quartz tube within a furnace. In order to successfully produce SWNTs the temperature of the reactor chamber must be heated and the temperature maintained between 800-1200°C. This heated region contains the target and the vaporized material travels down the quartz tube under 100 sccm flowing Ar.

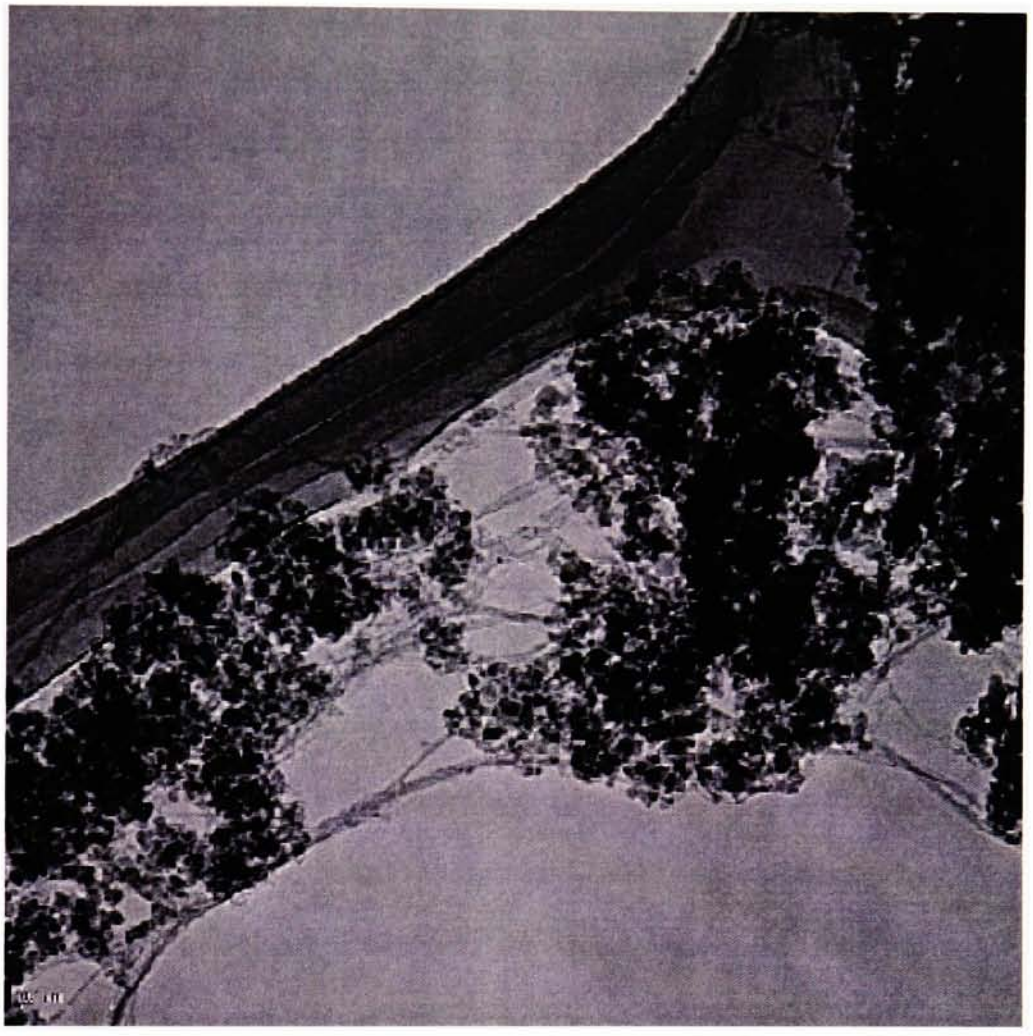

Figure 10: Example of CVD generated raw soot – SWNT bundles are present along with generous quantities of carbonaceous impurities.

When the vaporized material exits the heated portion of the furnace, product condenses on the walls of the quartz reactor tube. Often times a cold condenser will be used to collect the product. Figure 11 shows a generic laser vaporization synthesis apparatus. As with the other methods for synthesis, there has been considerable effort to elucidate the effect of the experimental variables on the final product. Figure 12 displays a TEM image of as-produced material synthesized by laser vaporization synthesis.

The most attractive feature of the laser vaporization technique, compared with other synthetic techniques, is the amount of control that is possible over the final SWNT product by using variation in experimental conditions. The effect of varying conditions such as reactor chamber temperature, laser beam characteristics, carrier gas flow dynamics, target composition, and reactor chamber configuration has been studied. The versatility of laser synthesis has been demonstrated in the ability to controllably influence diameter distributions, production rates, yield, and defect densities. Changes in a single variable may result in one or more variations in product characteristics.

The high temperature dependence for SWNT growth was observed in the first report of laser vaporization synthesis.[10] It was found that SWNT yield in the final product increased with increasing temperature up to 1200°C. A dramatic decrease in yield was observed for temperatures above 1200°C with the binary catalyst systems used in the targets. Perhaps the most profound impact of the synthesis temperature is its effect on the diameter distribution of the SWNTs in the final product. Higher synthesis temperatures, in general, lead to larger diameter SWNTs and lower temperatures produce smaller diameters. The width of the distribution does not necessarily increase with increasing temperature, however, the distribution will be centered about a higher

SWNT Synthesis by Laser Vaporization

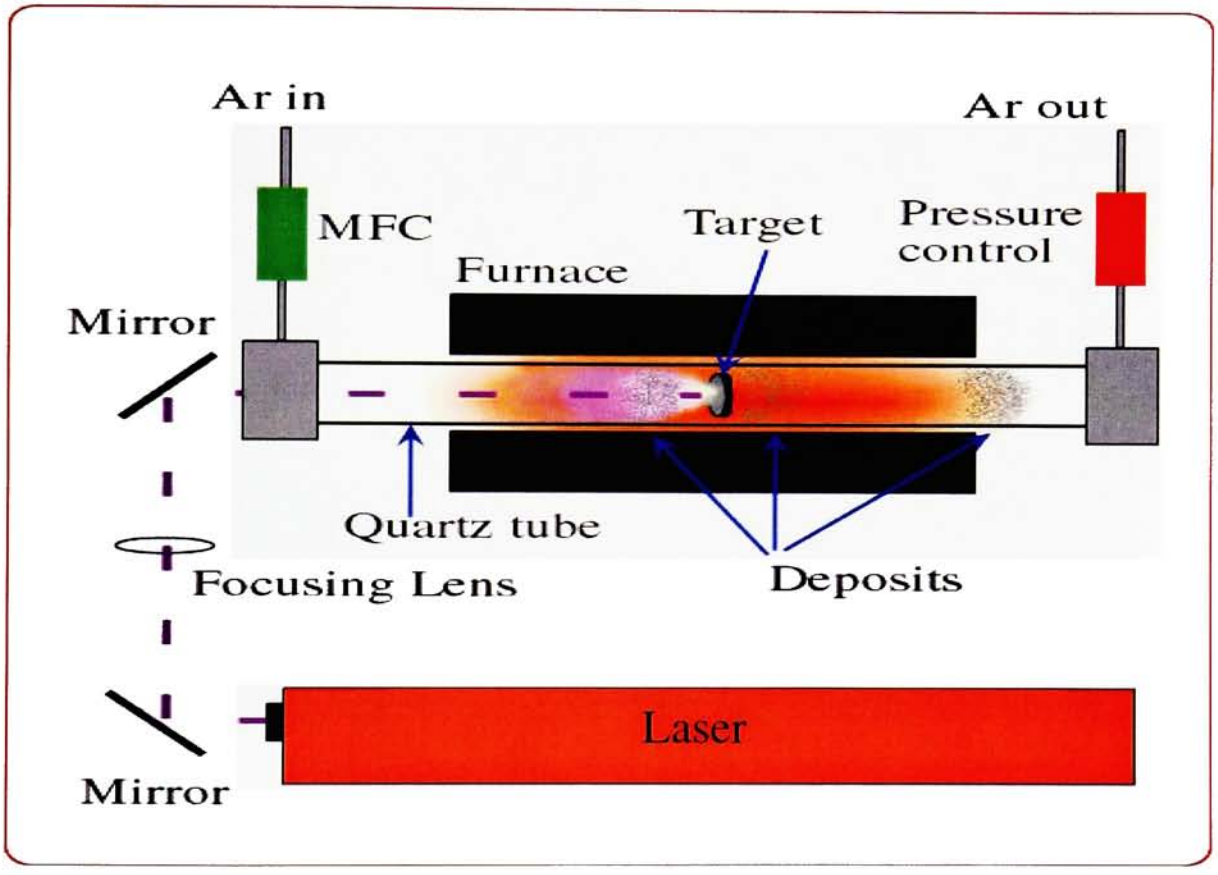

Figure 11: Typical laser vaporization apparatus. A pulsed or continuous laser is directed to strike a graphite target doped with catalyst metals. The quartz reactor chamber is kept under flowing inert atmosphere.

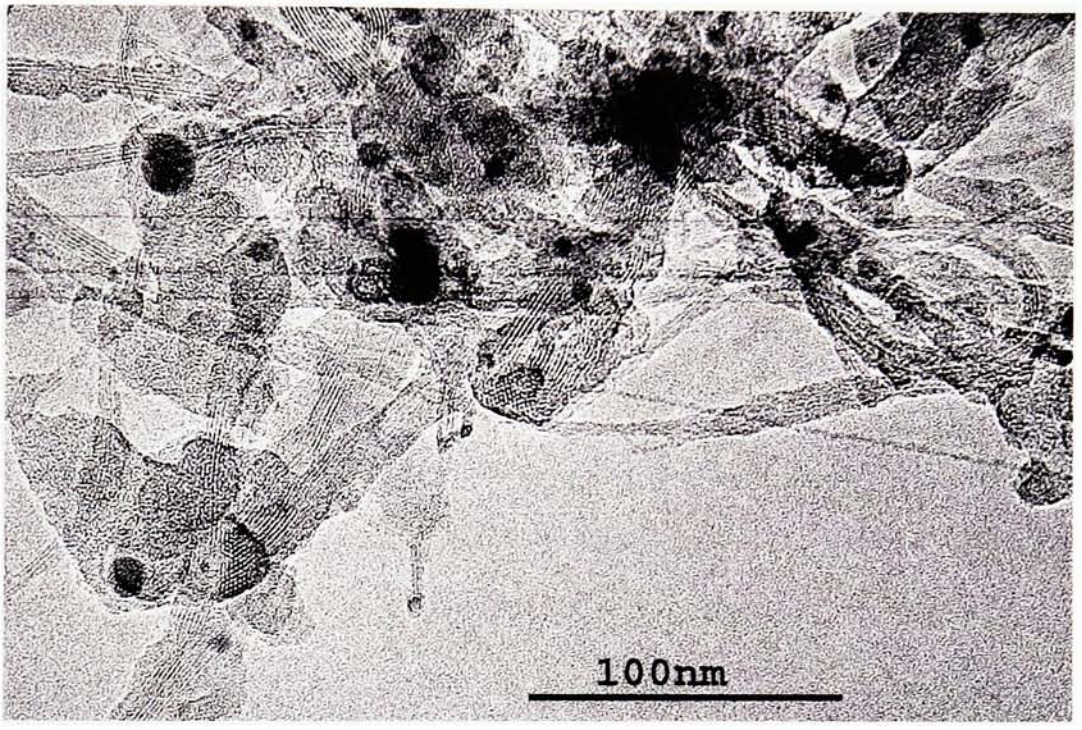

Figure 12: TEM image of as-produced laser vaporization SWNT material.

diameter.[60] It has also been reported that lower synthesis temperatures lead to higher SWNT defect density.

Characteristics of the laser that have been found to influence SWNTs produced are laser wavelength[61], incident beam power density,[62] pulsed or continuous beam[63], and pulse duration.[64] The various types of lasers that have been used to successfully synthesize SWNTs include Nd:YAG (1064 nm),[65] CO_2 (10.6 μm),[66] Alexandrite (755 nm)[67], UV (248 nm),[68] and free electron.[69] The minimum temperature at which SWNT growth can occur is influenced by laser wavelength. One of the lowest synthesis temperatures reported, 550°C, was achieved using a KrF laser with 248 nm wavelength.[68] Braidy et. al. demonstrated that yield and structural characteristics are highly sensitive to the laser intensity, or power density, regardless of the wavelength chosen.[62] An increase in the power density favors the production of smaller diameter SWNTs. The relative defect density of SWNTs was found to be a minimum for a power density of $1.7x10^9$-$2.9x10^9$ W/cm^2 (peak pulse power). Production rate increases with increasing power density, however, for power densities exceeding $2.9x10^9$ W/cm^2 a sharp decrease in SWNT production was observed. Maser et. al. found that production rates are greater for using a CO_2 laser in continuous wave mode than for the same laser in pulsed mode.[63] Localized heating of the target was also decreased using pulsed mode. Shorter pulse to pulse time intervals similarly result in increased production rate.[64] The pulse to pulse time interval has no influence on SWNT diameters or bundle thickness.

The carrier gas used, as well as its pressure and flow rate, has been shown to dramatically influence SWNT production. Argon is the most widely used carrier gas, however, others have successfully been used. In several instances SWNTs were

synthesized using N_2 carrier gas.[70-72] The final SWNT products were found to be quite similar when using Ar, N_2, or a mixture of the two gasses. No evidence of N_2 incorporation into SWNTs was observed, however, small amounts of functionalized nitrogen can be found in some of the amorphous carbon impurities in the product. Zhang claims that nitrogen atom incorporation into SWNTs is not feasible due to the sp^2 bonding arrangement.[70] Gorbunov and others carried out a study pertaining to the gas dynamics in laser synthesis. The optimal gas pressure was found to be 488 torr with a flow rate between 50-100 sccm at 1150°C.[73]

SWNT synthesis is especially sensitive to the catalyst systems chosen. Binary catalyst systems have demonstrated superior yields over single catalyst systems.[10] Some of the most successful binary systems include Ni/Co at 0.15-4.5 at. % each,[74] Ni/Y at 4.2 and 1.0 at % respectively,[75] Ni/Fe at 0.6 at % each,[60] and Rh/Pd at 1.2 at % each.[76] One popular catalyst system used is Ni/Co at 0.6 at % each. The catalyst system chosen strongly influences SWNT diameters and yields.[76] Kataura et. al. found that using Ni/Co catalyst there is an increase in yield up to about 1300°C and that yields decrease sharply beyond 1350°C. The most likely reason for this observation is that maintaining temperatures above the Ni-C and Co-C eutectic temperatures (1326°C and 1320°C respectively) does not allow for a eutectic phase transition to occur. This eutectic phase transformation is a critical step in SWNT self-assembly. When a Rh/Pt catalyst system is used there is an abundance of SWNTs even at 1450°C because the synthesis temperature is lower than the Rh-C and Pt-C eutectic temperatures (1694°C and 1705°C respectively).[67] Kataura also found that both Rh/Pt and Rh/Pd catalyst systems gave larger diameters than Ni/Co systems.[76]

The configuration of the reactor chamber has an influence on the quality of the material produced. In a study done by Rinzler et. al. an inner flow tube was introduced to confine the plume to a smaller area in front of the target.[19] This confinement allows for successive laser pulses to anneal the growing SWNTs and gives a product with lower defect densities.[77] The inner diameter of the reactor tube was varied as well, in increments of 1 inch, 2 inches, and 4 inches.[19] Production rates increased dramatically with increasing reactor tube diameter.

Laser vaporization synthesis is capable of producing high quality material in excellent yield in comparison to most other techniques. Relatively low production rates, however, have prevented bulk production of laser material. A significant issue that has emerged in laser synthesis is induced non-uniformities at the target surface during the synthesis. This problem was addressed by Yudasaka et. al. in 1997.[78] This study found that the composition of the surface of the target became enriched with metal catalyst. This enrichment in turn caused a decrease in the yield of nanotubes in the raw soot. Yields were lowered due to insufficient carbonaceous feedstock concentration in the plume after laser vaporization of the target material. The solution to this problem was to use two different targets, one of pure carbon and one of Ni/Co metal catalyst, which were simultaneously irradiated by the laser. This double target arrangement produced SWNTs when the power of the laser was 4.4 W or less. This method also averted pitted regions on the target which helped maintain uniformity of material concentration in the plume. Another attempt to preserve target surface uniformity was made by Eklund et. al.[69] The apparatus used in this study used a free electron laser capable of producing sub-picosecond pulses with a rotating graphite target. The sub-picosecond pulses reduced the

amount of localized heating on the target surface and the rotation of the target provided a clean surface for vaporization. This method achieved a production rate of 1.5 g/hr. All of the variables used to influence the final SWNT product make laser vaporization synthesis an extremely versatile technique.

1.2.4 Other Synthetic Methods

Various other synthetic methods have been shown to produce SWNTs that cannot be classified as one of the previous three techniques. One notable example of these methods is the solar furnace technique.[79] Although similar to laser vaporization, the solar furnace technique is unique in that it uses concentrated sunlight as the radiation source. The synthesis takes place within a vertical furnace with Ar carrier gas and powdered target mixtures can be used. Another interesting example of successful nanotube formation was using polyyne-containing carbons with electron beam irradiation at elevated temperatures.[80] There has even been a report of solution phase nanotube synthesis in organic halocarbon solvents using silicon nanowires.[81] These examples of alternate synthetic routes to produce carbon nanotubes demonstrate the likelihood of other synthetic developments.

1.3 Proposed Mechanisms for SWNT Self-Assembly Via Laser Vaporization Synthesis

An understanding of the fundamental mechanistic details involved in the self-assembly of SWNTs is highly sought after by those involved in the field of this research. Unfortunately, there is no universal consensus on the complete mechanism and facets of various proposed mechanisms are currently being debated. There has, however, been a significant amount of work carried out in determining many details of SWNT formation via laser vaporization. It is generally recognized that there are three stages of SWNT

formation; nucleation, growth, and termination. Nucleation involves the event of incipient formation of the first carbon-carbon bonds that will ultimately comprise a portion of the structure of an SWNT. Growth involves the addition and incorporation of carbon atoms into the SWNT structure from a carbon feedstock. Termination is the event that introduces the final carbon atoms into the nanotube structure and, in an ideal case, provides structural closure. It should be noted that, depending on the experimental conditions, complete closure of SWNTs may or may not occur. The details of the nucleation event, aspects of nanotube growth, and the process of termination are issues which have received a great deal of attention. It is likely that a complete and coherent model of the mechanism of SWNT formation will foster an understanding of how to optimize yields as well as lend insight into fundamental physical behavior of similar systems.

1.3.1 Early Models and the "Scooter" Mechanism

Proposed aspects of the mechanism of SWNT self assembly via laser synthesis came as early as the first report of using the laser technique.[10] This report is one of many by researchers at Rice University that have contributed to work in laser vaporization synthesis. One of the issues inherent in the synthesis process is the preferential formation of SWNTs over MWNTs. In the initial report, it was assumed that the particle size of the nucleated material in the vapor phase was too small to nucleate growth of MWNTs. An important observation made was that under the same synthetic conditions, in absence of metal catalyst in the graphite target, fullerenes were formed in the product and no SWNTs were observed. It was then proposed that the nucleation event involved production of fullerene caps and the metal particles adsorbed onto these caps to prevent

closure into fullerenes. The fullerene caps then act as nucleation sites for the condensation of metal clusters from the vapor phase. The growth phase of this model predicted that vaporized carbon fragments were able to diffuse through the metal clusters attached to the fullerene caps and became inserted into the "dangling bonds" of the cap. Although the metal clusters adsorbed onto the growing SWNT may also grow in size during growth, the creation of a large number of dangling bonds on a second wall would present a larger energy barrier than would the lower strain energy of a second wall. The small size of the catalyst particle, therefore, only prevents MWNT formation during nucleation.

Additional research pertaining to the preferential formation of SWNTs vs. MWNTs was performed by Guo et. al. in 1995.[82] They found that both MWNTs and spheroidal fullerenes were produced using the laser vaporization technique with an undoped graphite target. Although no SWNTs were found in the raw soot, mechanistic detail on why MWNTs form preferentially in this case is proposed. Using ab initio and tight binding calculations it was concluded that transient bridging carbon "adatoms" between adjacent MWNT walls stabilized the growing multi walled tubes. Insertion of these adatoms is energetically favorable compared to insertion of carbon directly into one of the growing walls. In this manner, closure of the MWNTs is prevented. The reason for the preferential formation of MWNTs in the case of undoped target, as well as other synthetic techniques, is the higher density of carbon in the feedstock. When the target is doped with catalyst metal, the resulting carbon feedstock is not sufficiently dense to produce MWNTs according to this model. Another conclusion drawn in this study was that nanotube formation occurs homogeneously in the gas phase.

Shortly after the discovery of laser synthesis researchers at Rice and other universities proposed the "scooter model" as the mechanism of SWNT formation.[41] Tight binding and density functional theory calculations were used to calculate the most energetically stable precursor and intermediate structures. It was proposed that initially, after vaporization, one catalyst atom chemisorbs onto a graphene cluster of less than 50 atoms. In order for this metal catalyst atom to be effective in promoting SWNT growth it must be sufficiently electronegative to avoid endohedral fullerene formation. The chemisorbed metal atom then promotes growth by "scooting" around the open edge of the graphene cluster, helping to add carbon atoms to the dangling bonds, and also annealing away carbon structures that are not energetically favored. One of the key features proposed in the scooter model is the ability for formation of strained triple bonds along the periphery. This model assumes SWNT growth occurs until a sufficient number of catalyst atoms aggregate onto the growing end of the nanotube. At the point of sufficient aggregation the catalyst particles either detach from the growing structure or the catalyst becomes ineffective as a result of a carbonaceous coating. The described termination step will leave the growing end with a closed fullerene cap or with an aggregate of catalyst metal. No account of the timescale for these events is postulated in this mechanistic model.[77] This model proposes that the most energetically favored nanotube is the (10,10) tube followed by (9,9) and (8,8) which are all armchair metallic SWNTs.

1.3.2 Kinetics and Thermodynamics of SWNT Formation

Studies conducted on the kinetic and thermodynamic aspects of SWNT formation have contributed to the overall completeness of proposed mechanisms. One notable

study was carried out by Jost et. al.[72] The target in these experiments consisted of a mixture of charcoal doped with 0.75 at. % Ni and Co. A 1.08 μm Nd:YAP laser with 700 mJ pulse power at 20 ns was used for synthesis. Determination of the rate-limiting processes was the focus of this set of experiments. Ultimately, rate-limiting steps were identified and mechanistic detail was provided from these data. The first was identified as a gas kinetic process. Optical absorption spectroscopy was used to evaluate SWNT content within the as-produced material. Yields of SWNTs dropped considerably at 950°C compared to 1150°C. At 1150°C the optimal pressures were found to be between 188-375 torr using Ar or N_2 carrier gasses. Using He, however, the optimal pressure increased to at least 500 torr. The carrier gas chosen, temperature, and pressure determine momentum transfer, heat diffusion, and mass diffusion within the vaporized material. These conditions can be quantitatively described by a gas kinetic coefficient D^g. The D^g values determined in this study for optimal conditions gave good uniform agreement over all conditions. From these results it can be concluded that this gas kinetic process is a rate-limiting step in the formation of SWNTs. The formation of fullerenes was identified as a thermally activated rate-limiting step. The activation energy for this process was given between 70-90 kJ/mol.

1.3.3 Current Models

The important discovery, that SWNT growth occurs as a condensed phase process, is now an important aspect to mechanistic considerations. Strong evidence for condensed phase, or solid state, growth of SWNTs came from laser annealing of nanoparticulate soot to yield lengthened SWNTs.[83] "Nanotube seeds" were produced using laser vaporization that were essentially SWNTs that had not completed growth due

to rapid quenching of the vaporized material inside the synthesis apparatus. Laser annealing was carried out with a CO_2 laser under 500 torr of flowing Ar. The SWNT seeds were found to lengthen in the temperature range of 1000-1300°C. This temperature range is quite similar to the range for optimal growth in laser synthesis.

A key feature of modern mechanistic models is a definitive time frame for the various stages of self-assembly of nanotubes. One study carried out by Puretzky et. al. highlights the time frame in which several component events take place.[84] Using in situ spectroscopy and imaging of Co, C_2, and C_3 fragments it was concluded that the entire process of self-assembly takes place on the order of one second. The temperature of the plume directly after incipient laser irradiation was determined to be between 3500-4000°C as determined by optical pyrometer. Initially the vaporization produced Ni and Co atoms, as well as C, C_2, and C_3 fragments that exist in the vapor phase for the first 100 μs after vaporization. At 100 μs the temperature drops below 3500°C and atomic clusters of carbon begin to condense while atomic Ni and Co remain in the vapor phase. A plateau in the plume temperature occurs between 0.3 ms and 0.7 ms. This plateau is attributed to an exothermic process, most likely formation of fullerene-like structures, which would signify the nucleation event. After about 1 ms, when the temperature decreases below 1750°C, the Ni/Co metal clusters begin to condense with the carbon clusters. At 2 ms after vaporization, when the temperature is about 1400°C, the vaporized material has completely condensed into clusters and nanoparticles. The onset of SWNT growth takes place after these clusters have cooled below their eutectic temperatures, between 2 and 3 ms. Growth can continue in the heated region of the reactor vessel so long as there is carbon feedstock available to diffuse through the clusters

to the growing nanotube ends. An important observation made in this study is that carbon nanoparticles aggregate much faster with lower ambient temperatures. As an example, the average particle radius, after 1 ms, of carbon clusters at a temperature of 700°C is 80 nm, but only 20 nm at 1100°C. The larger particle size leads to a decrease in mobility and hence lower yields. The overall range for the growth rate of SWNTs was given as 0.6-5.1 μm/s.

A study carried out by Scott et. al. gives insight into an overview of many mechanistic details of the synthesis process.[77,85] Using laser scattering experiments it was concluded that clusters form after vaporization and are not sputtered from the surface of the target by incident radiation. The amount of material that is vaporized is strongly dependent on the surface temperature of the target. The vaporized carbon species coalesce to form fullerenes. Metal particles condense after carbon and agglomerate onto the existing carbon clusters, fullerenes, and other fragments. The metal particles may prevent fullerene closure and additional laser pulses may serve to cause excitation of fullerenes so that they eject C_2 fragments. Growth is then propagated by carbon that diffuses through the metal or by carbon that is adsorbed on the metal surface. The growth rate they give is higher that that given by Puretzky. Their calculated value is 5 μm/ms.[85]

1.4 Characterization of SWNT Materials

Several techniques have been used to evaluate SWNT characteristics. Although the study of these materials is not bounded by any particular techniques, certain standard methods for evaluation of SWNT materials have evolved. These techniques include optical and vibrational spectroscopies, which are useful in evaluation of diameter

distributions. Various microscopic techniques yield images of nanotube materials with resolution on the nanometer scale. Thermogravimetric analysis (TGA) is useful in evaluating thermal decomposition characteristics and residual metal content.

1.4.1 Spectroscopic Techniques

Spectroscopic evaluation provides a wealth of information pertaining to SWNT characteristics. Electronic and vibrational spectroscopies have been quite successful in evaluating diameter distributions, metallic to semiconducting ratios, sample purity, and relative defect densities for products of individual syntheses. The two predominant techniques used to evaluate SWNTs are optical spectroscopy in the UV-Vis and near IR region, and Raman spectroscopy. Others, such as ^{13}C NMR and electron energy loss spectroscopy (EELS), have also been used and will be considered.

1.4.1.1 UV-Vis-NIR Spectroscopy

The electronic structure of carbon nanotubes depends primarily on helicity and diameter. Since the diameters are much smaller compared to their length, the allowed electronic states in the circumferential direction will be much smaller compared to the allowed electronic states in the axial direction. The 1D electronic density of states, therefore, is considered only with respect to the quantum confinement of electrons in the radial and circumferential directions.[86] UV-Vis-NIR spectroscopy is a macroscopic probe for SWNT samples and gives information on the bulk material with respect to the electronic density of states. A typical UV-Vis-NIR spectrum of as produced SWNT material will display three characteristic peaks. These peaks correspond to the first, second, and third Van Hove singularities predicted in the density of states. As a result, the peaks are commonly referred to as the first, second, and third Van Hove peaks going

from higher to lower wavelength. A representative UV-Vis-NIR spectrum of purified laser material can be seen in Figure 13.

Metallic and semiconducting SWNTs give rise to different Van Hove peaks in their optical spectra. The first and second Van Hove peaks arise from electronic transitions in the semiconducting SWNTs, whereas the metallic SWNTs give rise to the third Van Hove peak. Since absorbance is proportional to concentration of individual species of the sample, a relative ratio of semiconducting to metallic SWNTs can be gained from the optical spectra.

Information pertaining to the diameter distribution for a certain SWNT sample can be obtained using optical spectroscopy. It is standard to consider the first Van Hove peak in diameter analysis. In general, the λ_{max} of the first Van Hove peak will be at higher wavelengths for larger diameter SWNTs and at lower wavelengths for smaller diameter SWNTs. The diameter corresponding to the λ_{max} can be calculated from the equation $d = 8.041 \times 10^{-4} \lambda$, where d is the diameter in nm.[16] It is important to note that the diameter corresponding to the λ_{max} is not necessarily the mean diameter of the sample. The SWNT sample will contain a distribution of discrete diameters centered about the λ_{max} diameter.

A study on the evaluation of the % w/w SWNTs in as produced batches by NIR spectroscopy has been conducted by Itkis et. al.[87] Solution phase spectroscopy was carried out with the assumption made that only SWNTs, amorphous carbon, and metallic impurities were present in the as-produced sample. Carbon black was used as a background to determine the amount of carbonaceous impurities in the sample. The ratio

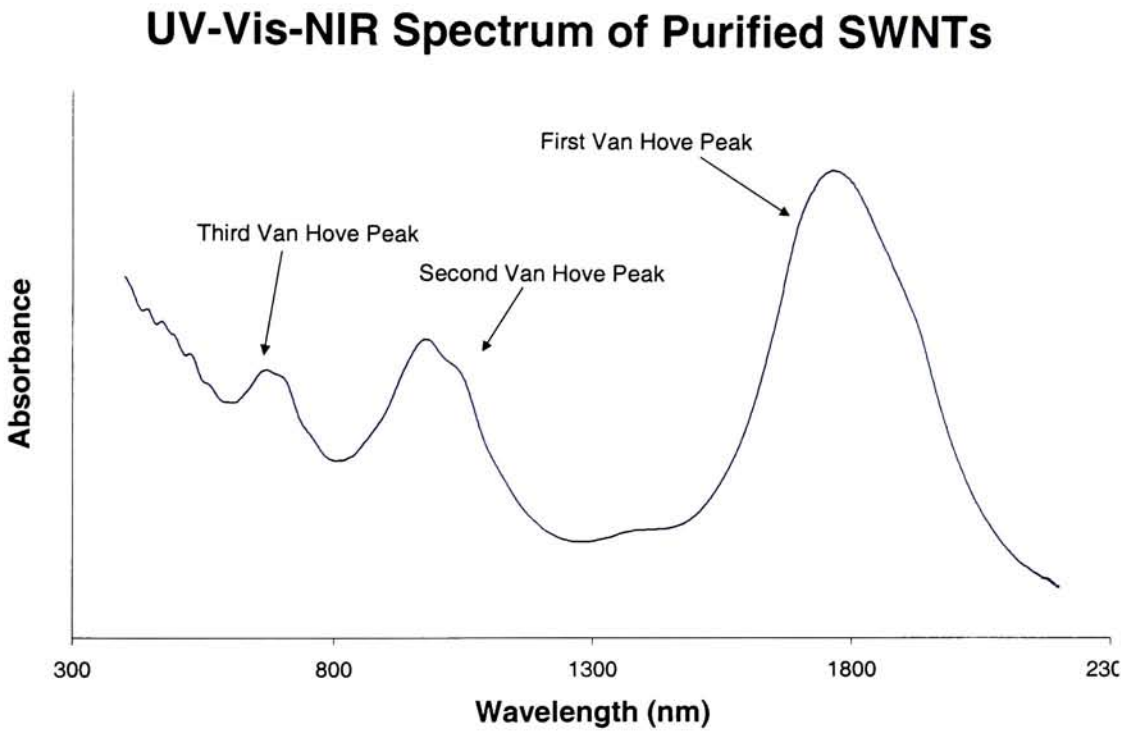

Figure 13: Representative UV-Vis-NIR spectrum of purified laser generated SWNTs.

of the absorbance of the second Van Hove peak to a pure reference was used to quantitatively determine SWNT purity.

1.4.1.2 Raman Spectroscopy

The use of Raman spectroscopy has been particularly useful in evaluating diameter distributions and relative SWNT defect densities. In general, SWNT samples will give a spectrum with three regions of interest in the Stokes domain. An example of a Raman spectrum of an as-produced laser sample is shown in Figure 14. The region from 50-350 cm^{-1} constitutes the radial breathing mode (RBM). The frequency of the peaks in the radial breathing mode increase with the reciprocal of the SWNT diameters that give rise to the signal. Assignment of diameters based on the individual peaks in the RBM is carried out by using the equation $d = 223.75 \text{ nm}/ \omega_r$ where ω_r is the frequency of the peak in the RBM.[60] It should be noted that there exist a number of variations in the equations used to determine SWNT diameters from these peaks, each of which gives a slightly different diameter assessment.[88-90] It has been reported that the peaks in the RBM can provide determination of the (n,m) designation for individual nanotubes.[91]

The region from 1300-1700 cm^{-1} contains two characteristic SWNT peaks of importance. The first peak, typically at about 1300 cm^{-1}, is known as the D band. The second set of peaks, typically at about 1500 cm^{-1}, is known as the tangential mode or the G band. The D band is associated with the amount of disorder within the structure of the SWNTs.[92] It is known that disordered graphite displays a similar peak at 1300 cm^{-1} in the Raman spectrum, whereas single crystal graphite does not show this peak.[93] In fact, it is predicted that an infinitely long SWNT with no defects would display no intensity in the D band.[94] Comparisons of the relative disorder in SWNTs are generally carried out

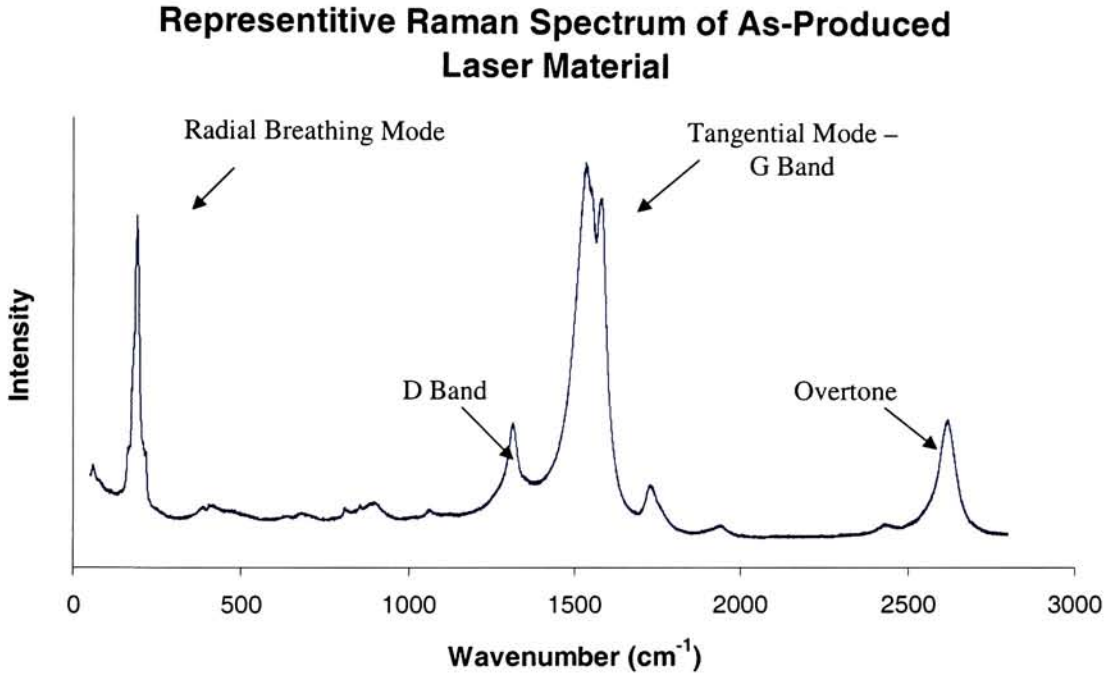

Figure 14: Example of a Raman spectrum of as-produced laser generated material Excitation wavelength = 633 nm.

by taking the ratio of the heights of the D band to the G band. Disordered and amorphous carbon, as well as disordered graphite will also contribute to the D band. The D/G ratio of a sample then can give an approximate SWNT abundance. The third region of the Raman spectra resides around 2600 cm^{-1}. This peak is an overtone of the D band at 1300 and is sometimes called the G' band or D^* band.

The excitation wavelength used to obtain the Raman spectra of SWNTs will influence the results in the RBM. Resonant enhancement of either metallic or semiconducting SWNTs occurs at different wavelengths for a given range of diameters. For example, laser generated material with a diameter range of 1.2-1.5 nm has metallic SWNTs that are resonantly enhanced with a 633 nm excitation wavelength and semiconducting SWNTs that are resonantly enhanced with a 488 nm excitation wavelength. As a result a 633 nm laser used to obtain a Raman spectrum will probe metallic SWNTs only in the RBM and a 488 nm laser will probe only semiconducting SWNTs.

1.4.1.3 Other Spectroscopic techniques

Two other predominant spectroscopic techniques that have successfully provided useful information pertaining to the metallic and semiconducting behavior of SWNTs are ^{13}C NMR and EELS. The ^{13}C NMR studies of SWNTs indicate two distinct ^{13}C nuclear spins are present due to two different spin-lattice relaxation rates.[95] The faster relaxation was attributed metallic SWNTs, whereas the semiconducting SWNTs have a slow relaxation time. The presence of O_2 interferes with these spectroscopic studies due to the paramagnetic nature of O_2. EELS has been performed on bulk macroscopic samples of SWNTs.[96] The results of this study indicate that the dispersion relation, similar to that of

graphite, is attributed to metallic SWNTs and the nondispersive transitions are due to semiconducting SWNTs.

1.4.2 Microscopic Techniques

Electron microscopies and surface microscopies have generated means to provide detailed images of SWNTs. Scanning electron microscopy (SEM) and transmission electron microscopy (TEM) have both been used extensively. SEM provides qualitative images of SWNT surface characteristics and contours. SWNT bundles can start to be seen at about 20kX magnification. Figure 12 displays an SEM image of as-produced material synthesized via laser vaporization. SWNT bundles, as well as other impurities, can be seen in this image.

TEM is used in a similar fashion to provide detailed images of SWNTs. High resolution TEM has been used to image individual SWNTs within bundles. Figure 10 shows one such TEM image. The use of this technique can distinguish between bundles of single wall and individual multi wall nanotubes. It is important to remember that both SEM and TEM provide images of an extremely small region. Images obtained may not necessarily be representative of the entire sample, as batches of SWNTs are often inhomogeneous.

Characterization of SWNTS by other microscopic techniques, such as atomic force microscopy (AFM) and scanning tunneling microscopy (STM), has provided insight into nanotube features.[20] STM studies have been used as local probes to determine structural characteristics. In one study by Odom et. al. correlation between SWNT structure and electronic properties was made.[8] Another STM study revealed that

the SWNT lattice may in a triangular arrangement instead of the expected hexagonal type.[97]

1.4.3 Thermogravimetric Analysis

TGA is useful in determining information about the decomposition characteristics of an SWNT sample. The onset of thermal decomposition usually corresponds to the oxidation of amorphous or otherwise functionalized carbon. Laser generated SWNTs generally oxidize in air ambient between 500-600°C. Smaller diameter SWNTs oxidize at a lower temperature than larger diameters. Often the first derivative, with respect to temperature, of the thermogram provides useful information of the inflection points and separate the corresponding peaks attributed to amorphous carbon and SWNTs. Figure 15 displays a TGA thermogram along with its first derivative curve. The residual metal oxide content from the thermal metal oxidation can also be obtained from the thermogram. The corresponding metal content in the as-produced soot then is 78.6% of the residual metal oxide content for Ni/Co catalyst (Oxidation to Ni(II) and Co(II)).

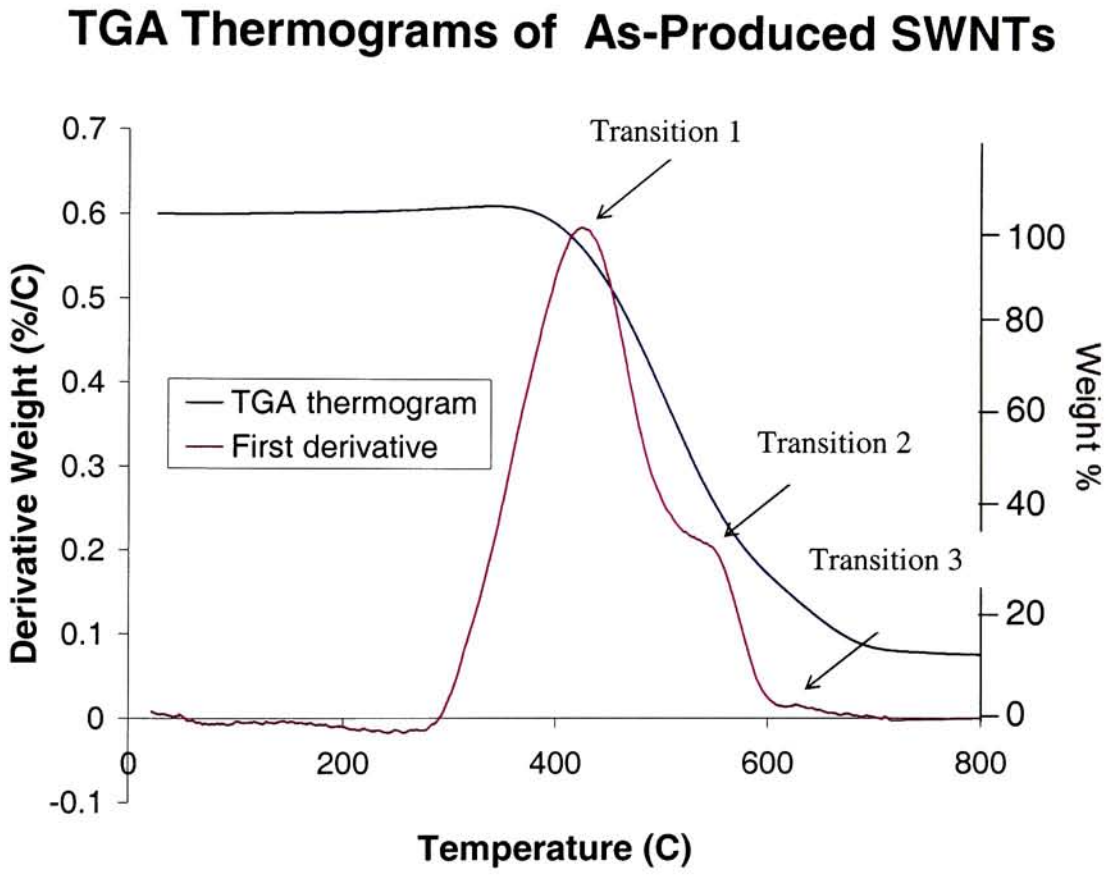

Figure 15: TGA thermogram of as-produced laser SWNTs with its first derivative.

2.0 Experimental

2.1 Synthesis Conditions

All SWNT materials were synthesized using pulsed laser vaporization. A schematic of the synthesis apparatus is depicted in Figure 16. A general description of synthetic conditions is given below. Details of how these parameters were altered for specific studies are described in Section 2.2. A graphite target is prepared from a mixture with the appropriate metal catalyst dopants. The solid target mixture, is prepared by combining 98.8% 1-2 μm graphite (Aldrich), 0.6 at. % 2 μm cobalt (Aldrich), and 0.6 at. % submicron nickel (Alfa Aesar) in a sealed rotating mixing apparatus and stirred for 48-96 hours to ensure relative homogeneity. The target is pressed from 4 g of this mixture at 20,000 psi in a Carver hydraulic pellet press (model # 3925) for four minutes to give a 30 mm diameter by 5 mm thick disc. The target is then loaded into the quartz reactor chamber tube. A quartz target holder keeps the disc upright in the center of the chamber with one face of the disc facing the laser beam. The reactor chamber is then sealed and evacuated using a Welch vacuum pump (model # 8920) to a pressure of about 0.1 torr. A total of three purge-backfill cycles are performed with argon to minimize the amounts of oxygen and moisture in the chamber. After the final backfill the pressure is brought to 500 torr and argon is introduced into the chamber at a flow rate of 100 sccm with a mass flow controller. Typically the temperature for the synthesis ranges from 900-1200°C. The length of the heated region of the quartz chamber is 83 cm. Normally the target would be placed in the center of this heated region so that it was 41.5 cm from either end of the furnace. The total length of the quartz reactor tube is 1.48 m and the inner diameter is 4.5 cm. Other important information on the parameters for the synthesis,

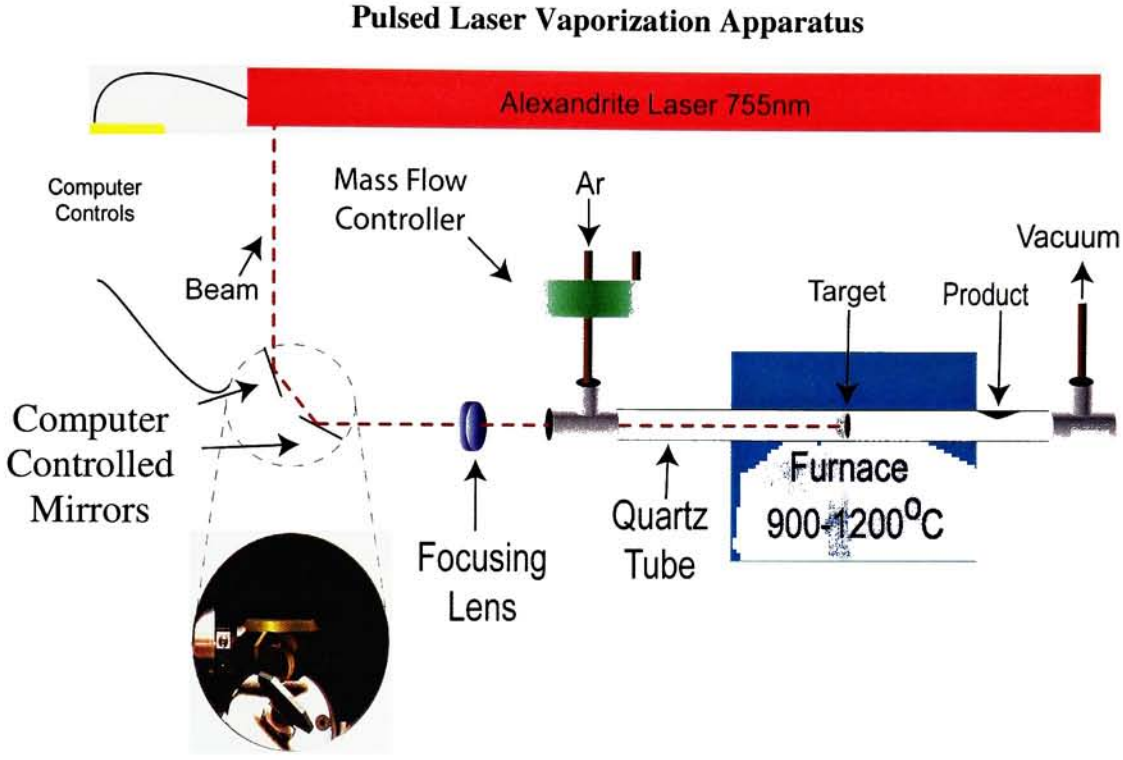

Figure 16: Pulsed laser vaporization apparatus – Diagram of the apparatus used to synthesize material for the comprehensive investigation of parameters of laser vaporization synthesis. A picture of the digitally controlled mirrors is shown.

including details of the target, the reactor, and the laser are listed in Tables 1-3.

Table 1: Parameters for the Laser

Parameter	Specification
Type	Pulsed Alexandrite (single crystal $BeAl_2O_4$ doped with Cr^{3+})
Wavelength	755 nm
Pulse duration	100 μs
Repetition rate	10 Hz
Incident beam power	4.7 W
Peak power	1 MW

Table 2: Target Characteristics

Parameter	Specification
Composition	4 g 1-2 μm graphite doped with 0.6 at. % submicron Ni and 0.6 at % 2 μm Co
Pressing pressure and duration	20,000 PSI for 4 min
Dimensions	30 mm diameter x 5 mm width
Vaporization area on surface	1 cm x 1 cm

Table 3: Reactor Specifications

Parameter	Specification
Carrier gas	500 torr Ar flowing at 100 sccm
Reactor chamber volume	2.4 L
Reactor temperature	900-1200°C
Mirror repetition rate	>10 Hz

During the synthesis the laser produces 100 μs pulses at a repetition rate of 10 Hz. In order to raster the beam across the surface of the target a set of computer controlled mirrors (GSI Lumonics SC 2000 scan controller) is used to direct the pulsed beam. These mirrors are capable of moving at a rate of up to 20 Hz. With these mirrors it is possible to use an appropriate computer program to control the mirrors to direct the beam to the desired area of the surface of the target. Between 0% and 100% overlap between adjacent spots on the target surface can be achieved using the mirrors. The net effect of using the mirrors is the creation of the desired pattern across the surface of the target with

the pulsed laser beam. Normally, in the current study, the raster pattern chosen was such that the laser beam scanned linearly across the surface using 50% overlap between adjacent spots. The option to vary the overlap of successive pulses before moving to the next spot was available in the range of 0-100%.

Each pulse of the laser vaporizes a small amount of material from the surface of the target creating a plume of vaporized material in front of the target. Care was taken to ensure that ablation of the surface, which introduces significant amounts of graphitic impurities in the product, did not occur. The vaporized material is carried down the length of the quartz reactor tube by the flowing argon and at a certain time it exits the portion of the tube that is in the furnace. The vaporized material then collects in the cold region of quartz tube outside the furnace to form the raw soot product on the upper portion of the tube.

2.2 Variations in Synthesis Parameters for Product Analysis

In order to ascertain how certain synthesis parameters influence the SWNT diameters, yield, and raw soot production rate, variations were made in the experimental conditions. The variations made for each parameter studied are summarized in Table 4. For most parameters, only one variable was altered per synthesis. Variation in reactor chamber temperature was investigated over the temperature range of 900-1200°C. In each case the furnace was allowed to reach the desired temperature prior to synthesis and this temperature was maintained throughout the entire procedure. Variation in the particle size of the graphite in the target was investigated. Graphite with particles sizes of 1-2 μm, 45 μm, and a 1:1 mixture of both 1-2 μm and 45 μm was used to prepare the targets used for synthesis. Two types of variations in reactor chamber configuration were

studied. First, the volume of the quartz reactor tube was altered. The volumes studied were 2.4 L and 1.6 L. Second, the target was placed in the center of a smaller quartz flow tube that was placed inside of the normal 2.4 L quartz reactor tube. This variation resulted in product present in three different collection regions. These regions were the carpet (rear of reactor tube), in front of the flow tube, and in the main reactor tube in the pattern of the furnace coils. The Raster pattern of the pulsed laser beam across the surface of the target was investigated. A total of four raster patterns were investigated. Figure 17 is an illustration the movement of how the precession of the laser pulses move across the surface of the target to carry out the raster pattern. The first pattern consisted of a linear scan with one pulse per spot. The second pattern also uses a linear scan, however, instead of one pulse per spot, 10 pulses were allowed to strike the same spot on the target before moving on to strike the adjacent spot. The third pattern uses a "corner to corner" raster where a pulse strikes the corner once then moves to another corner on the 1 cm^2 target vaporization area. The fourth pattern also uses a corner to corner raster, but strikes each spot with 5 laser pulses before moving to the next adjacent spot. Once each of the patterns is completed with one cycle over the target, the pattern starts again from the beginning. On average 100 pulses per cycle are used to scan over the surface of the target (With 2 mm spot size and 50% overlap). Incident beam power density was investigated over the range of 100-300 W/cm^2. The synthesis performed to study the effect of power density were all carried out using the one shot move to corner raster pattern. The average power of the incident beam was measured using an Ophir power meter. Spot size of the beam was measured by recording the diameter of the circular region a pulse left on black carbonaceous paper. Power density of the beam was

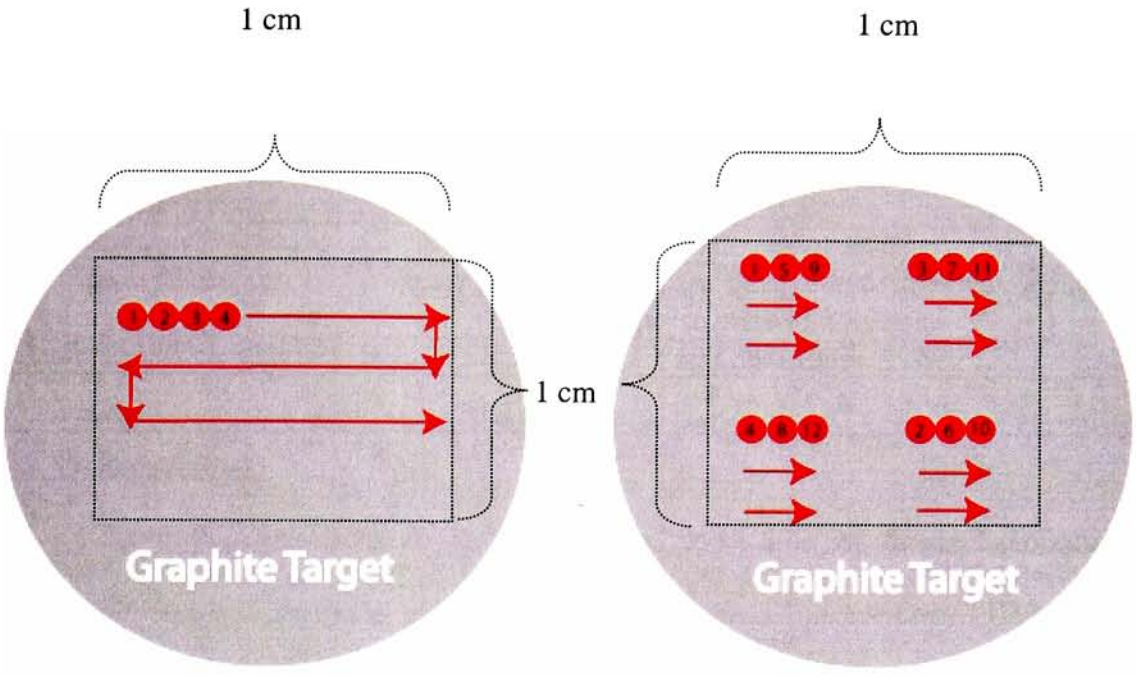

linear raster pattern **corner to corner raster pattern**

Figure 17: Schematic representation of the manner in which the laser beam is rastered across the surface of the target. The incident laser beam is controlled to hit a spot on the target a pre-established number of times before moving. The overlap of the spots was 50%. Once the program completes the programmed pattern dimensions it automatically resets to spot 1.

calculated by dividing the measured average power by the measured spot size.

Table 4: Parameter Variation Summary

Parameter	Increments in Variation
Temperatures (°C)	900, 1000, 1100, 1200
Catalyst Composition	0.6% Ni/Co
Graphite Particle Sizes	1-2 μm, 45 μm, 1:1 1-2 μm: 45 μm
Chamber Volumes	1.6 L, 2.4 L
Collection Regions	front, coil, carpet (rear)
Raster Patterns	linear one shot, linear ten shots, corner to corner one shot, corner to corner five shots
Power Densities (W/cm^2)	100, 200, 300

2.3 Characterization

All synthesized material was characterized using a set of standard procedures. The four standard methods used include TGA, Raman spectroscopy, UV-vis-NIR spectroscopy, and SEM.

A TA instruments model # 2950 Thermogravimetric Analyzer was used to acquire thermal decomposition data. A sample between 0.5-1.0 mg was used for analysis. Platinum pans were used to hold the sample during data acquisition. The initial temperature was 25°C and it was ramped up at 5°C per minute to 850°C. Often, if the thermogram indicated the material had completely oxidized the cessation of data acquisition occurred before 850°C. The oxidizing gas used was air flowing at a rate of 60 sccm.

UV-vis-NIR spectra were obtained on a Perkin Elmer Lambda 900 spectrometer. Samples were prepared by using 5 mg of the as produced SWNT material in 10 mL of acetone and dispersed in a Barnstead ultrasonic bath for 15 min. These dispersions were then immediately sprayed onto 1 in^2 quartz slides with an Anthem airbrush (model # 155-

7). The samples were allowed to dry in air and spectra were obtained between 300-2200 nm at a scan speed of 5 nm per second.

The Raman spectrometer used was a Jobin Horiba Labram HR. The instrument was calibrated to single crystal silicon at 0 and 520 cm^{-1}. For SWNT material, a small amount of the sample was placed on a glass microscope slide and a glass cover slip was placed over the sample. Two Raman spectra were obtained for each sample, one using a 632.8 nm HeNe laser (Jobin Horiba) and the other using a 488 nm Spectra Physics Stabilite Ar ion laser (model # 2017). Spectra were accumulated for 10 second time intervals with three repetitions. A 50x objective lens on a Olympus BX41 scope was used for all samples.

SEM images were obtained on a Hitachi S-900 near field scanning electron microscope. Samples were mounted on conductive carbon tape. Images were taken using a 2 kV accelerating voltage. The magnification of obtained images were between 40-60 kX. At least 10 images were taken of the individual samples over various locations on the sample.

3.0 Results and Discussion

The focus of this research is to investigate how variations in specific experimental conditions will affect the quality, yield, and content of PLV synthesized SWNTs. Conditions that were varied include laser beam raster pattern, reactor chamber temperature, graphite particle size in target, reactor chamber configuration, and incident laser beam power density. Characterization of the as-produced materials was completed for all parameters investigated using TGA, UV-vis-NIR spectroscopy, Raman spectroscopy and SEM. By understanding how the synthesis variables influence the final products, it is possible to exhibit control over in these parameters and synthesize the type of SWNT material desired.

3.1 Raster Pattern Variation

Previous experiments carried out by Yudasaka et. al.[78] and Eklund et. al.[69] demonstrated that repeated laser pulses directed onto the same location of the target caused an enrichment of the metal content at that spot on the target. In the course of performing these experiments it became evident that a similar phenomenon was occurring when a linear raster pattern was used. The 1 cm^2 area on the target surface displayed noticeable cone-like features, especially on targets used for syntheses at higher power densities. In order to ascertain the metal content within these cones, a portion of this material was scraped from the target surface and TGA was performed on the cone material. The results from this TGA compared to the standard target material are demonstrated in Figure 18. Material from the cones contains approximately twice as much metal as the standard target material. This metal build up at the target surface indicates that the laser causes metal catalyst enrichment at the surface of the target. It is

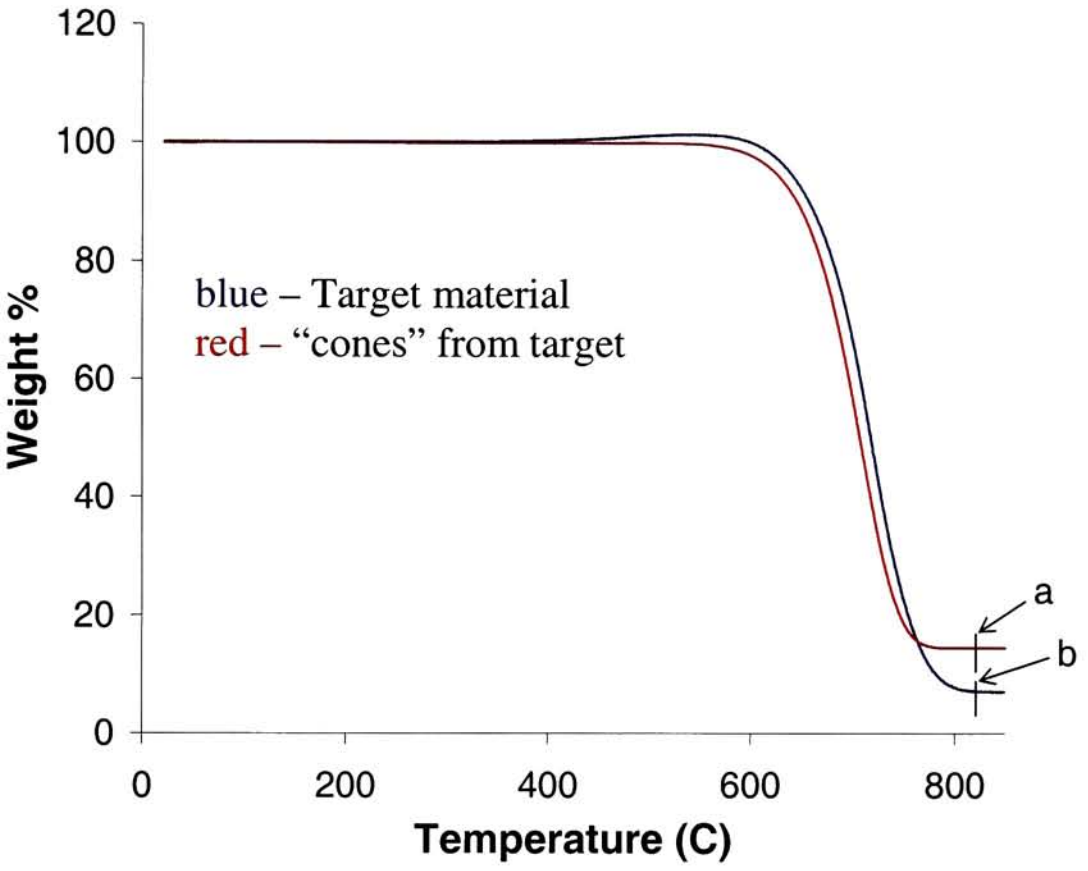

Figure 18: TGA Overlay of target material before synthesis and material on the target in the form of "cones" after synthesis. Target material consists of 1-2 μm graphite with Ni and Co catalysts at 0.6 at % each.

Thermogram	Residue %	Corresponding Metal %
a	14.46	11.37
b	7.121	5.597

likely that the energy from the laser causes localized heating on the target surface. Repeated laser pulses directed to the same spot on the target causes a significant amount of heating which eventually causes the metal catalyst to melt in the heated region. Once melted the metal catalyst migrates to the surface of the target resulting in localized inhomogeneous regions.

In an attempt to preserve surface homogeneity of the target, a corner to corner raster pattern was developed and used in a series of experiments. Resulting SWNTs synthesized using the corner to corner raster pattern were compared to those synthesized using a linear raster. In addition, the effect of successive laser pulses directed onto the same spot on the target was investigated. The four raster pattern variations studied are identified as one shot move linear, ten shots move linear, one shot move to corner, and five shots move to corner scans. The Raman spectra (Figures 19-22) for both 488 nm and 633 nm excitation indicate similar results. The RBM portions of the spectra show a shift to higher wavenumbers, therefore smaller diameters, for SWNTs synthesized with the one shot corner to corner raster pattern. The spectrum acquired at 633 nm excitation shows predominant peaks corresponding SWNT diameters of 1.22 nm and 1.15 nm for the one shot corner to corner raster pattern. In contrast, the linear raster patterns produced material with corresponding diameters of 1.34 nm and 1.24 nm. Similarly in the spectrum acquired at 488 nm excitation shows a predominant corresponding SWNT diameter of 1.23 nm for the corner to corner raster. The linear scans show predominant diameters of 1.38 nm and 1.30 nm.

The TGA data for the materials synthesized using the various raster patterns are shown in Figures 23 and 24. The SWNT materials synthesized with the one shot move to

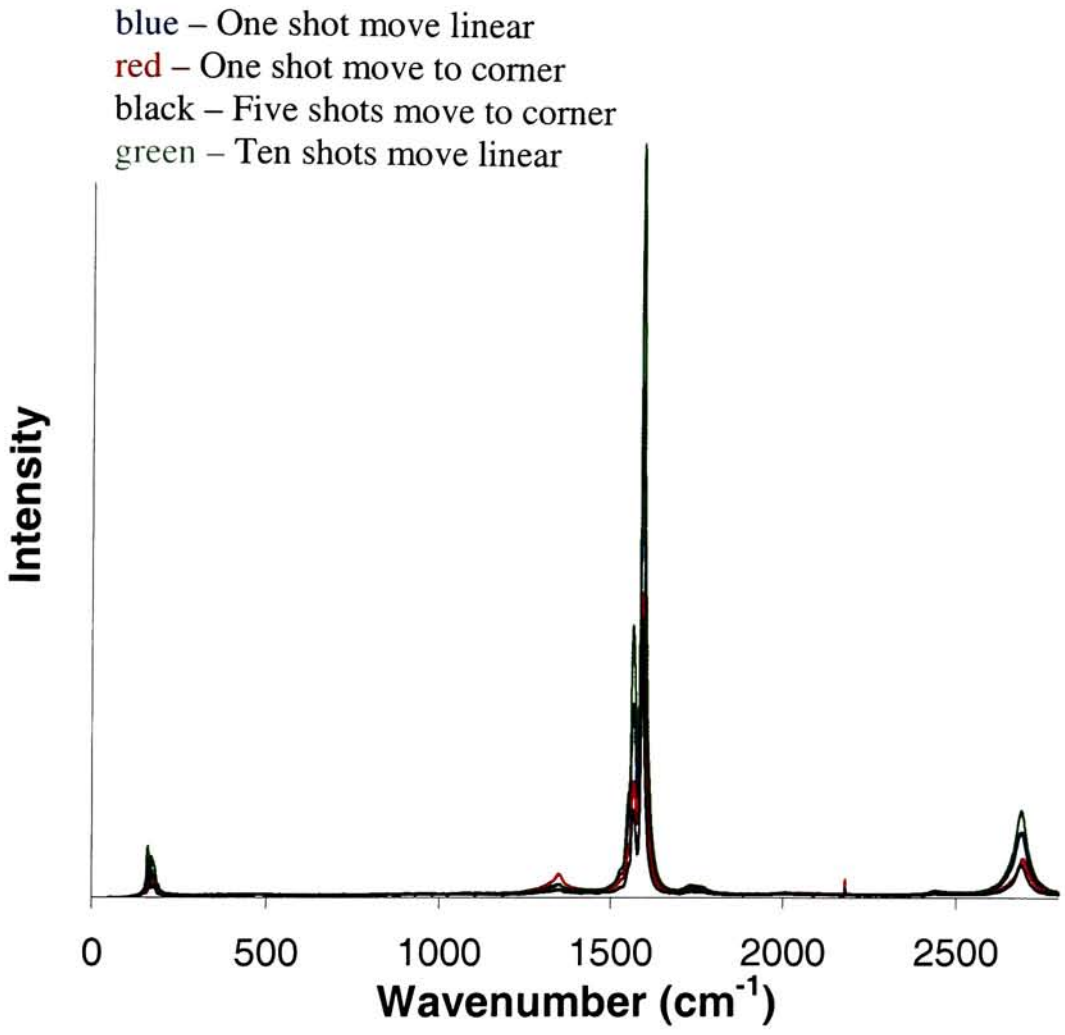

Figure 19: Overlay of Raman spectra taken of SWNT materials synthesized with different raster patterns. Excitation wavelength = 488 nm.

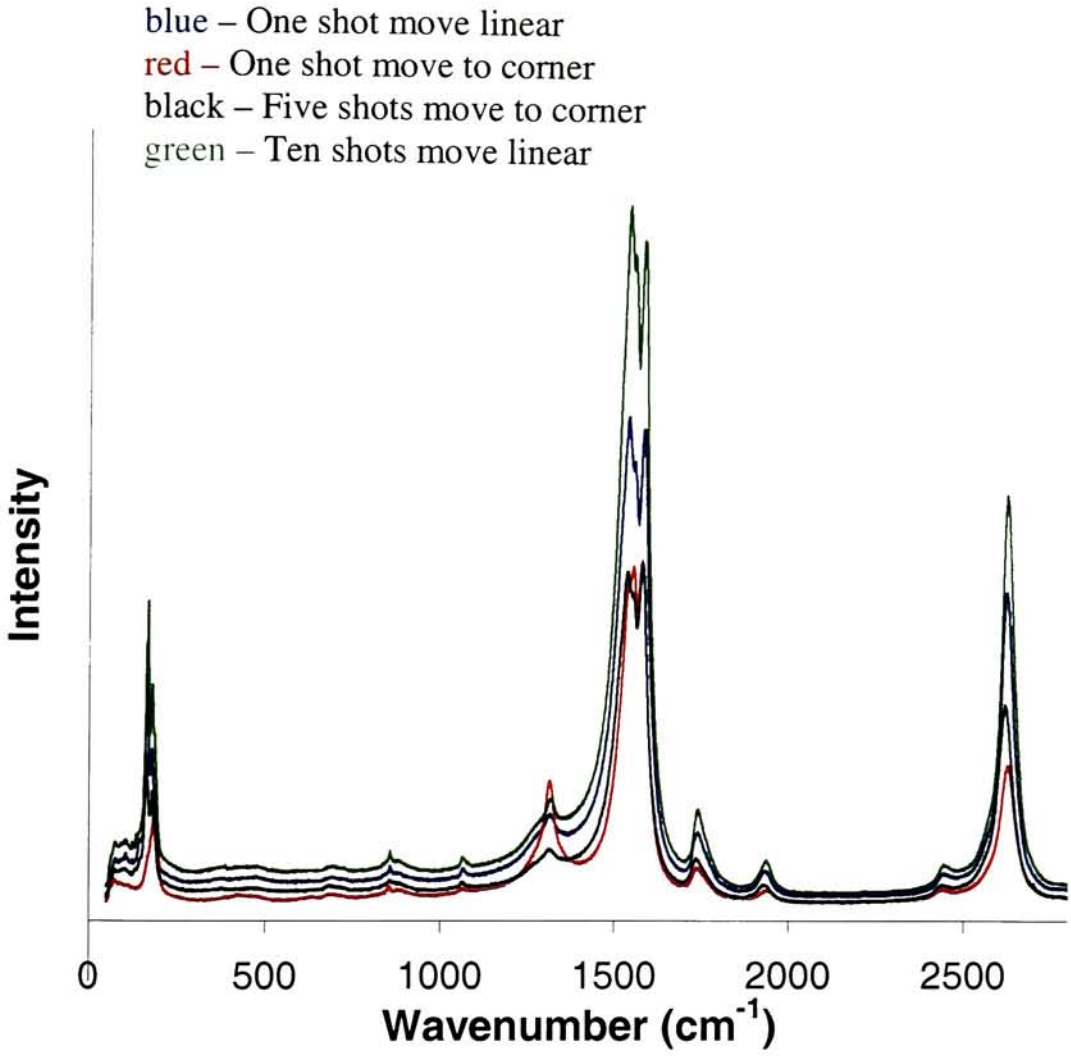

Figure 20: Overlay of Raman spectra taken of SWNT materials synthesized with different raster patterns. Excitation wavelength = 633 nm.

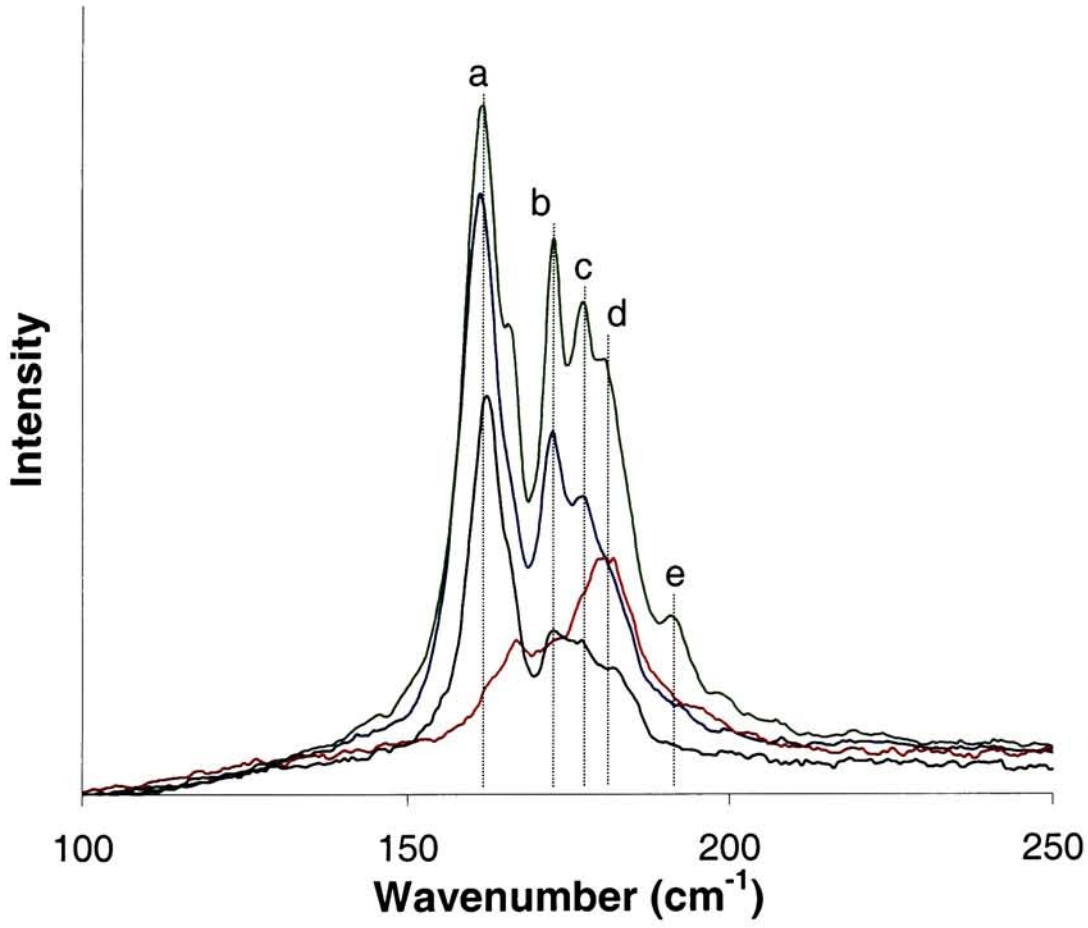

Figure 21: Raman RBM overlay for SWNTs synthesized using various raster patterns. Excitation wavelength = 488 nm.

Peak	Wavenumber (cm^{-1})	Corresponding diameter[59] (nm)
a	161.8	1.38
b	172.6	1.30
c	177.7	1.26
d	181.5	1.23
e	191.6	1.17

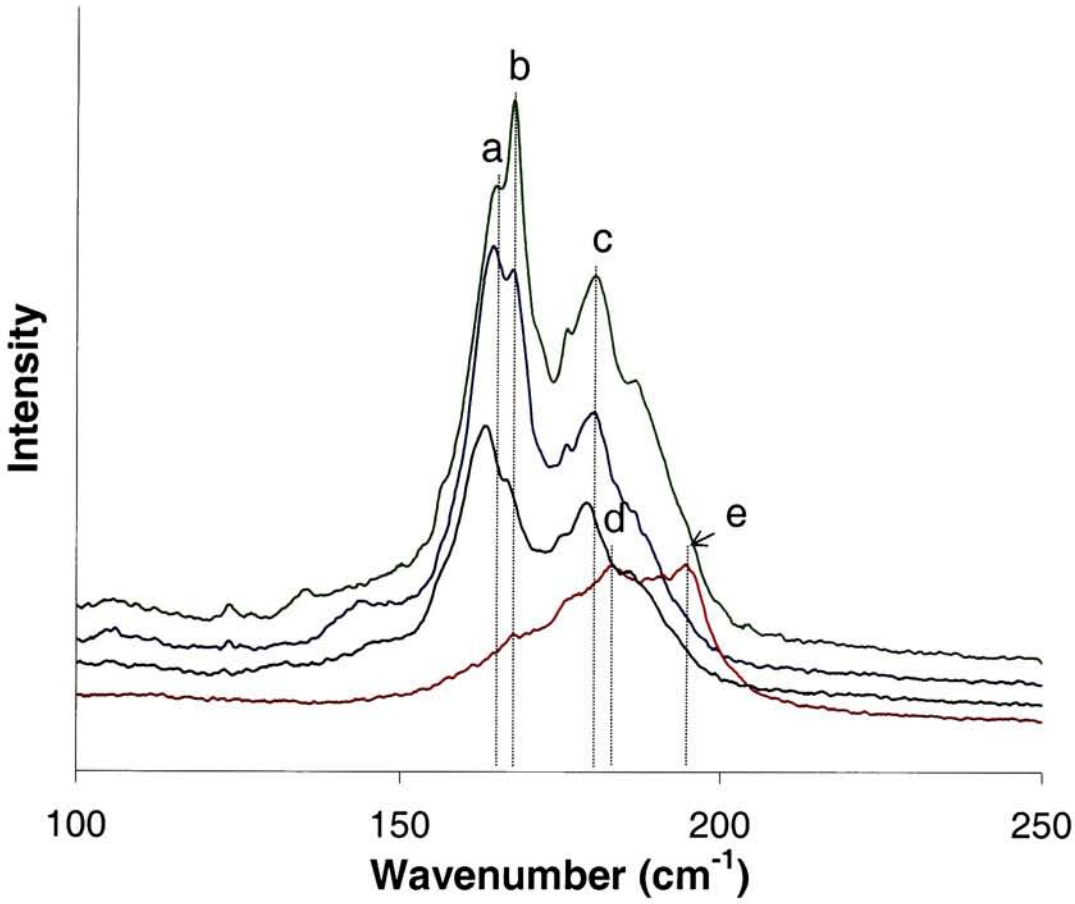

Figure 22: Raman RBM overlay for SWNTs synthesized using different raster patterns. Excitation wavelength = 633 nm.

Peak	Wavenumber (cm^{-1})	Corresponding diameter[59] (nm)
a	165.3	1.35
b	167.6	1.34
c	181.0	1.24
d	184.0	1.22
e	195.3	1.15

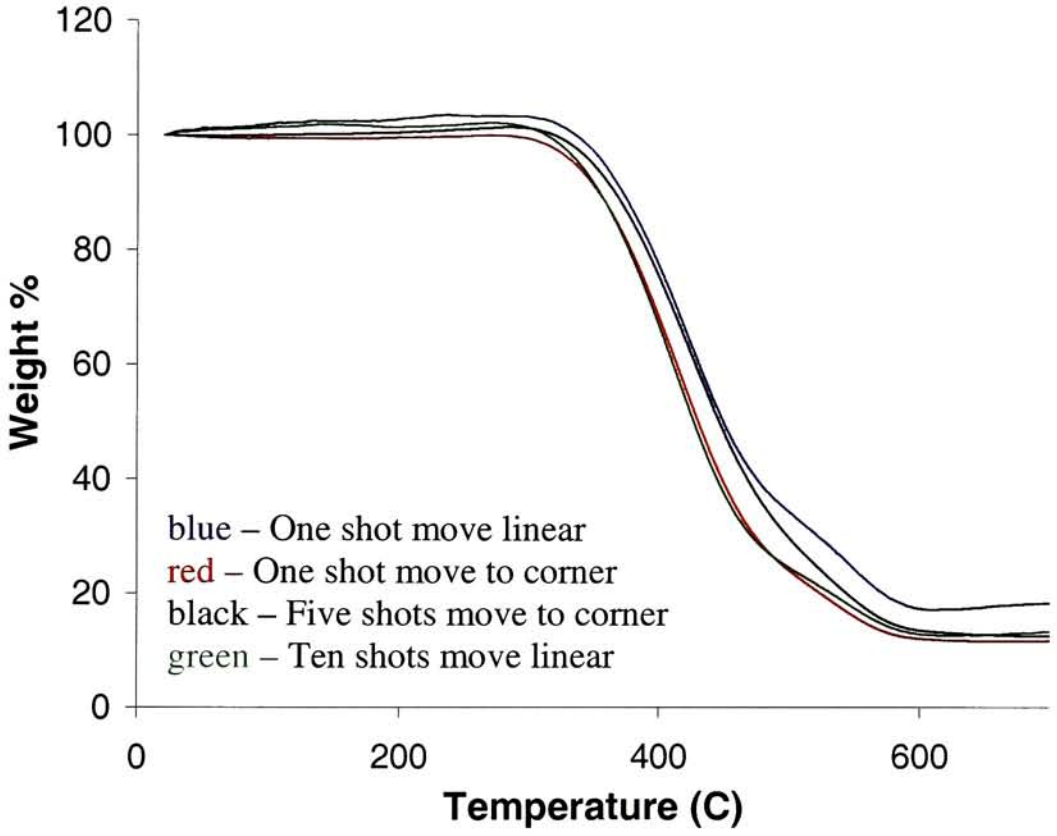

Figure 23: TGA overlay for SWNTs produced using different raster patterns.

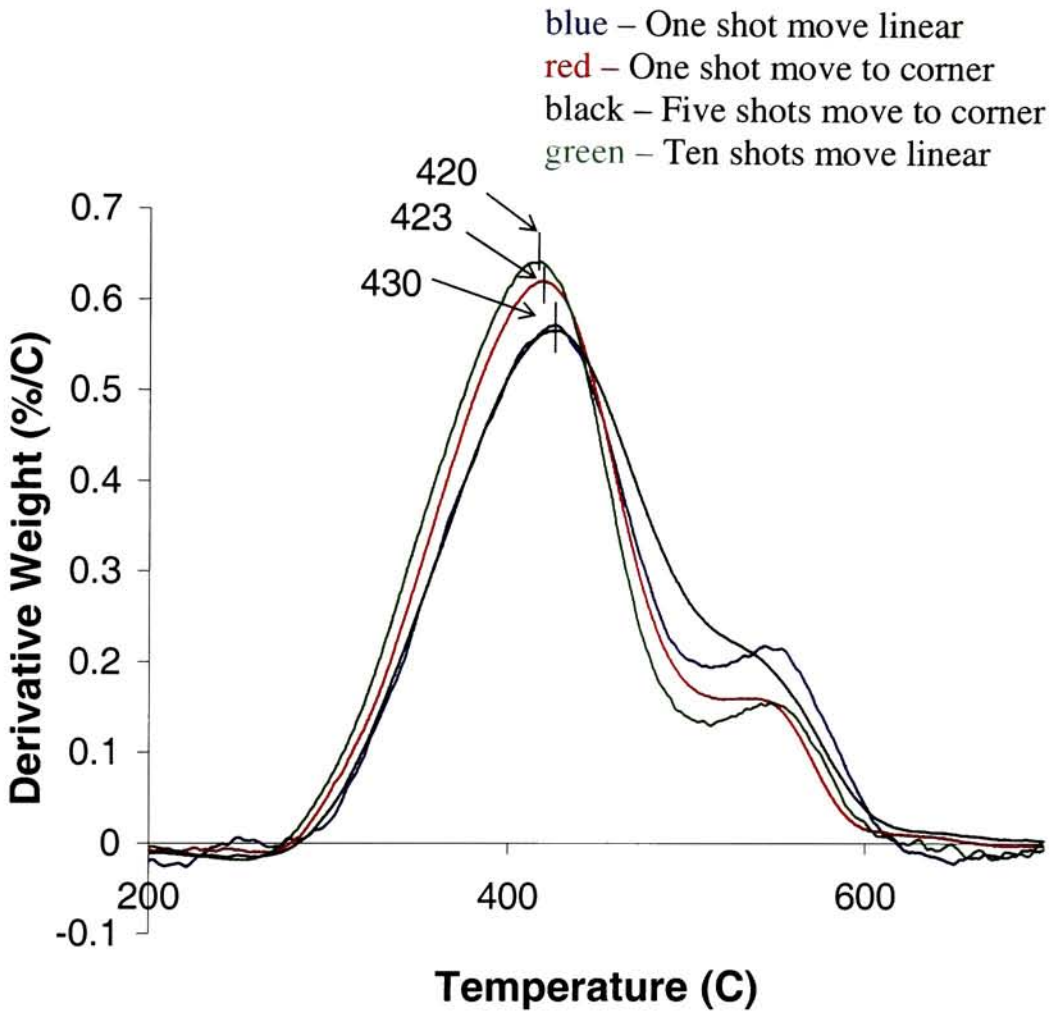

Figure 24: First derivative TGA overlay for as-produced SWNTs produced using different raster patterns.

corner and ten shots move linear display the earliest onset of thermal decomposition. The one shot move linear contains the highest metal content. The first derivative plot demonstrates that the peak corresponding to SWNTs increases in the order one shot move linear < five shots move to corner < one shot move to corner ≈ ten shots move linear. The UV-Vis-NIR spectra for these materials are displayed in Figure 25. The material synthesized using the ten shots move linear raster pattern displays the highest wavelength first Van Hove peak and largest corresponding diameter. The one shot move linear raster pattern demonstrates the lowest wavelength first Van Hove peak and similarly the smallest corresponding diameter. The trends shown in the UV-Vis-NIR spectra are similarly displayed in the RBM portion of the Raman spectra. The five shots move to corner raster pattern demonstrates similar results to the one shot move linear raster pattern in all data acquired. The D/G ratios for these materials are displayed in Table 5. The five shots move to corner raster pattern displays the lowest D/G ratio for both excitation wavelengths. Similarly the highest D/G ratio occurs with the one shot move to corner raster pattern. One possible explanation for the increase in the D/G ratio for the corner to corner raster pattern is that the vaporized material in the plume is not annealed by successive laser pulses. Since the subsequent pulses in the corner to corner pattern are directed toward another location on the surface of the target, the plume has much less exposure to these subsequent pulses. The SEM micrographs for these materials can be seen in Figure 26. SWNT bundles and amorphous carbon are present in all samples.

The spectroscopic results indicate that smaller diameter SWNTs are produced with the one shot corner to corner raster pattern. This trend is consistent with the reduction of ambient temperature during the synthesis. For example, smaller diameter

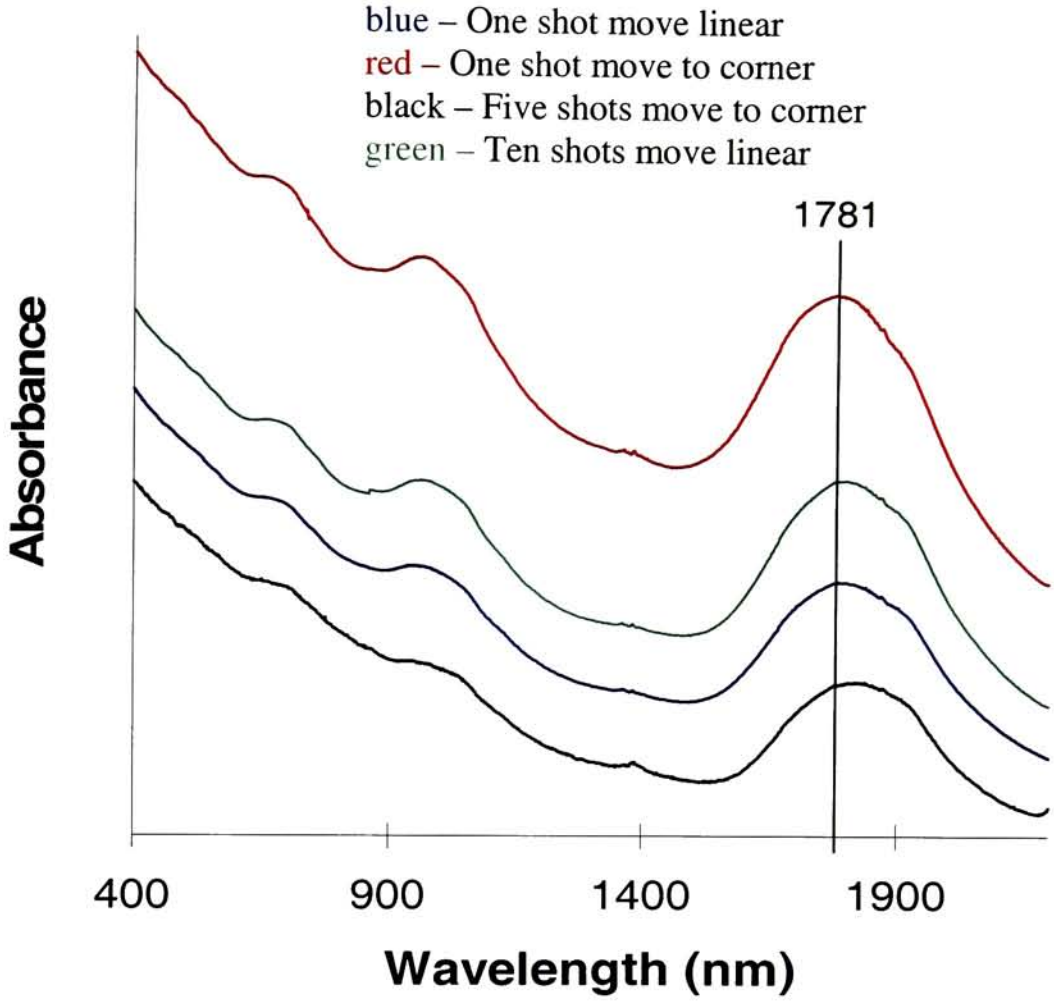

Figure 25: UV-Vis-NIR spectra taken from as-produced SWNTs synthesized using different raster patterns.

Raster pattern	First Van Hove peak (nm)	Corresponding diameter[16] (nm)
One shot move linear	1781	1.43
One shot move to corner	1798	1.44
Five shots move to corner	1789	1.45
Ten shots move linear	1822	1.47

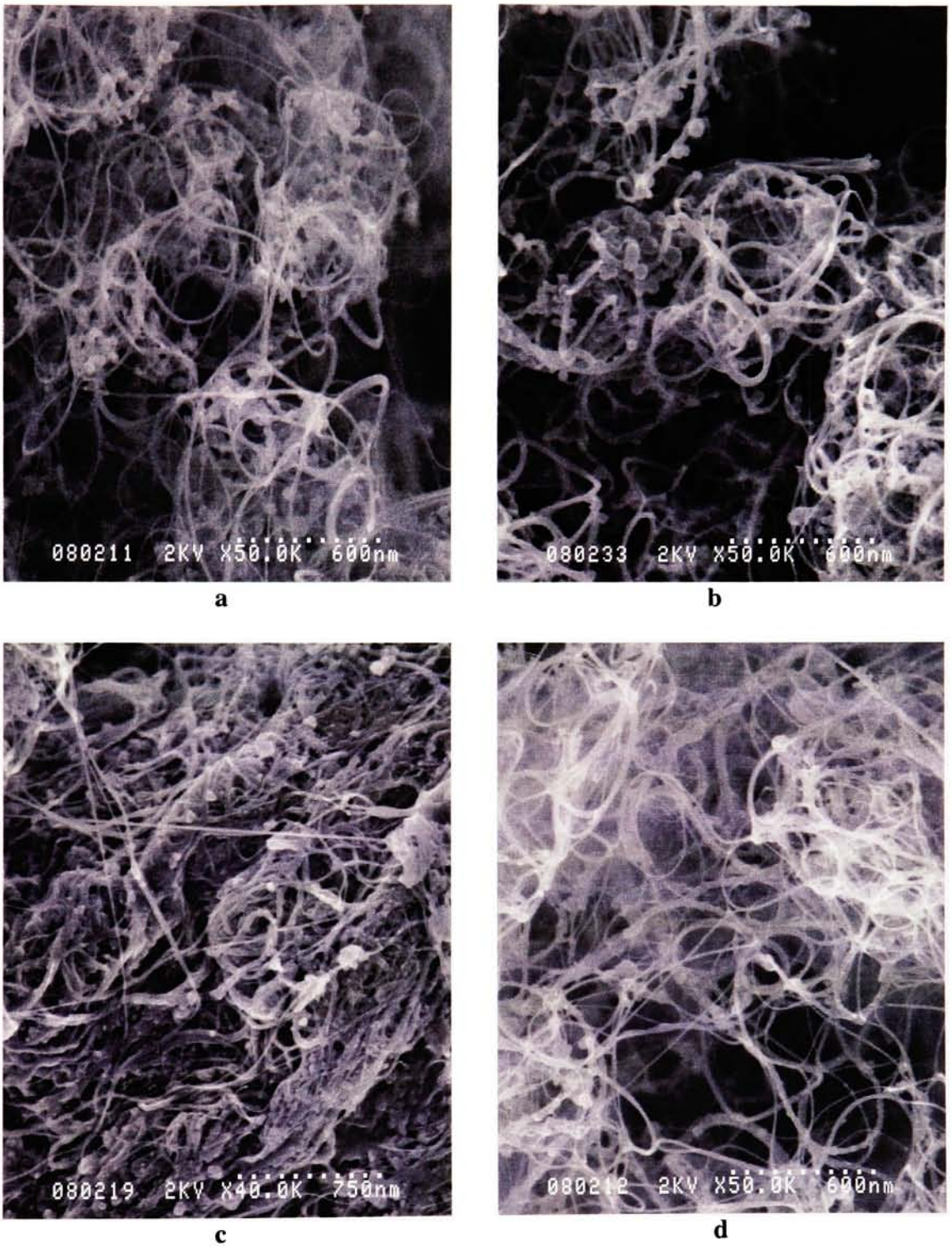

Figure 26: SEM micrographs of SWNTs produced using different raster patterns. a) one shot move linear b) one shot move to corner c) five shots move to corner d) ten shots move linear.

SWNTs are synthesized at lower temperatures (see section 3.2). The observation of smaller diameters synthesized with a corner to corner raster pattern is similar to the effects of lowering synthesis temperatures. It is therefore likely that by employing a corner to corner type raster the localized heating due to the laser pulses is reduced. The surface segregation of the metal catalyst is similarly reduced. Figure 27 displays an image of the target surface, taken with a light microscope, of the target surface after using the corner to corner raster pattern compared to the linear type raster pattern. The presence of cones has been eliminated from the surface subsequent to synthesis.

Table 5: D/G ratios for materials synthesized using various raster patterns.

Raster Pattern	488 nm Excitation			633 nm Excitation		
	D	**G**	**D/G**	**D**	**G**	**D/G**
one shot linear	472.3	17329.3	0.02725	1760.	8317	0.2116
one shot corner	820.0	10324.7	0.07942	2324	5972.7	0.3891
five shots corner	470.1	25544.8	0.01840	2036	11828	0.1721
ten shots linear	276.7	9517.3	0.02907	1191	5896	0.2020

3.2 Variation in Reactor Chamber Temperature

Previous experiments have demonstrated that SWNT diameters decrease with decreasing reactor chamber temperature.[59] Four synthesis temperatures of 900°C, 1000°C, 1100°C, and 1200°C were studied to observe this influence of temperature on the final SWNT product. The Raman spectra (figures 28 – 31) indicate that the results show agreement with the trend of decreasing SWNT diameters with decreasing synthesis temperature. The RBM portions of the spectra clearly display a shift to higher wavenumbers, therefore smaller diameters, for lower temperature syntheses. In the RBM portion of the spectrum acquired at 633 nm excitation the predominant SWNT diameters are 1.36 nm and 1.33 nm for 1200°C and 1.17 nm and 1.01 nm for 900°C. Similarly, at

a)

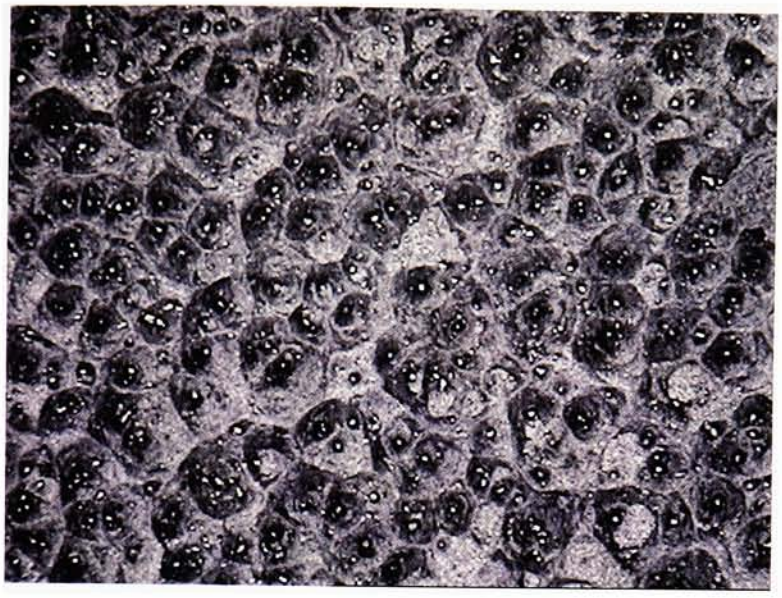

b)

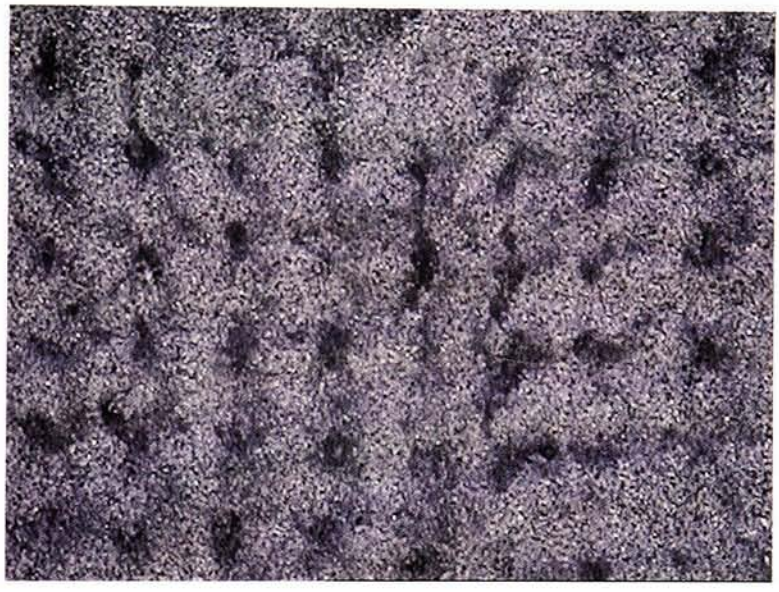

Figure 27: a) Target surface after using "ten shot move linear" raster pattern. Cone formation is clearly visible at 100X magnification.
b) Target surface after using a "one shot move to corner" raster pattern. The surface is smooth and homogeneous.

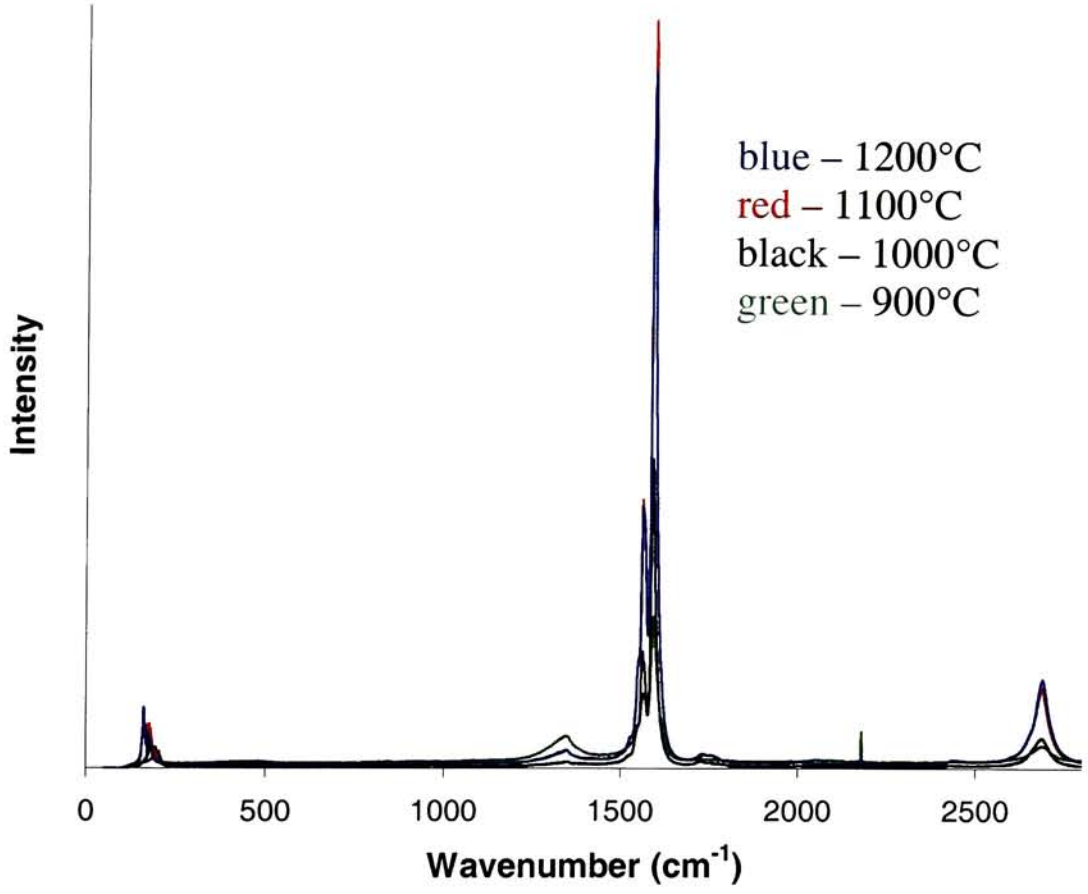

Figure 28: Overlay of Raman spectra taken of SWNT materials synthesized at various temperatures. Excitation wavelength = 488 nm.

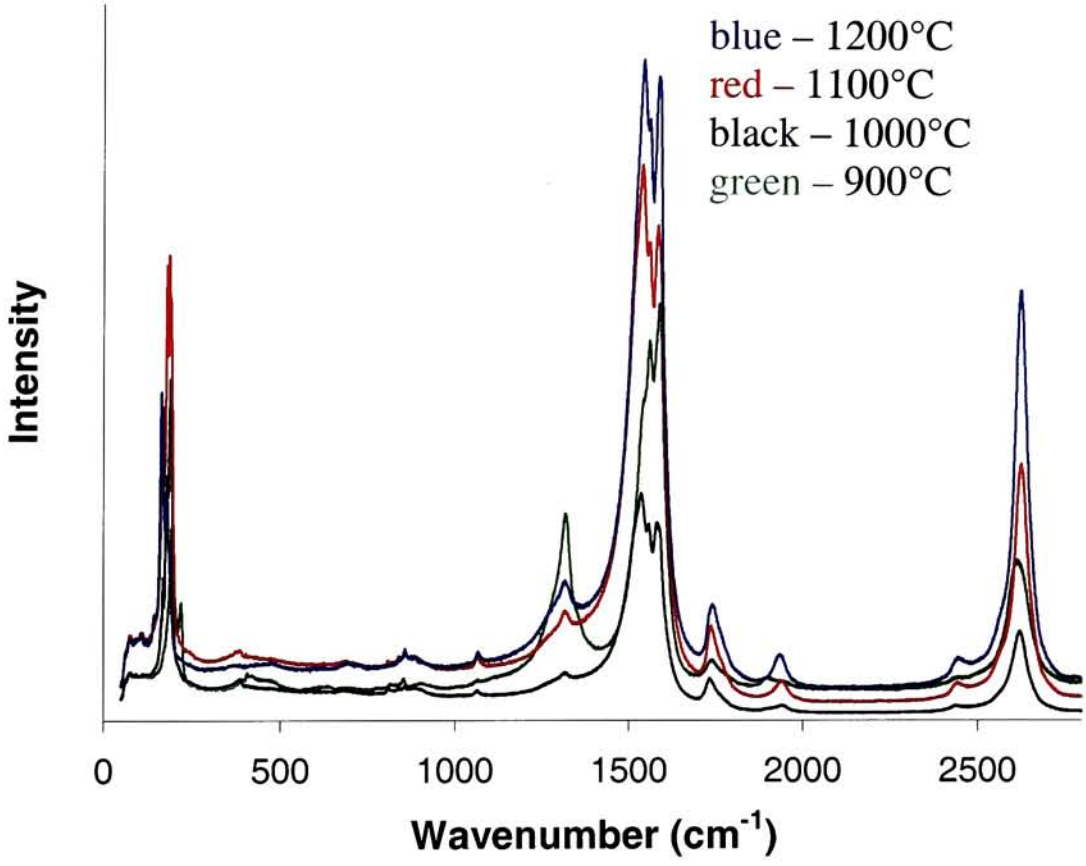

Figure 29: Overlay of Raman spectra taken of SWNT materials synthesized at various temperatures. Excitation wavelength = 633 nm.

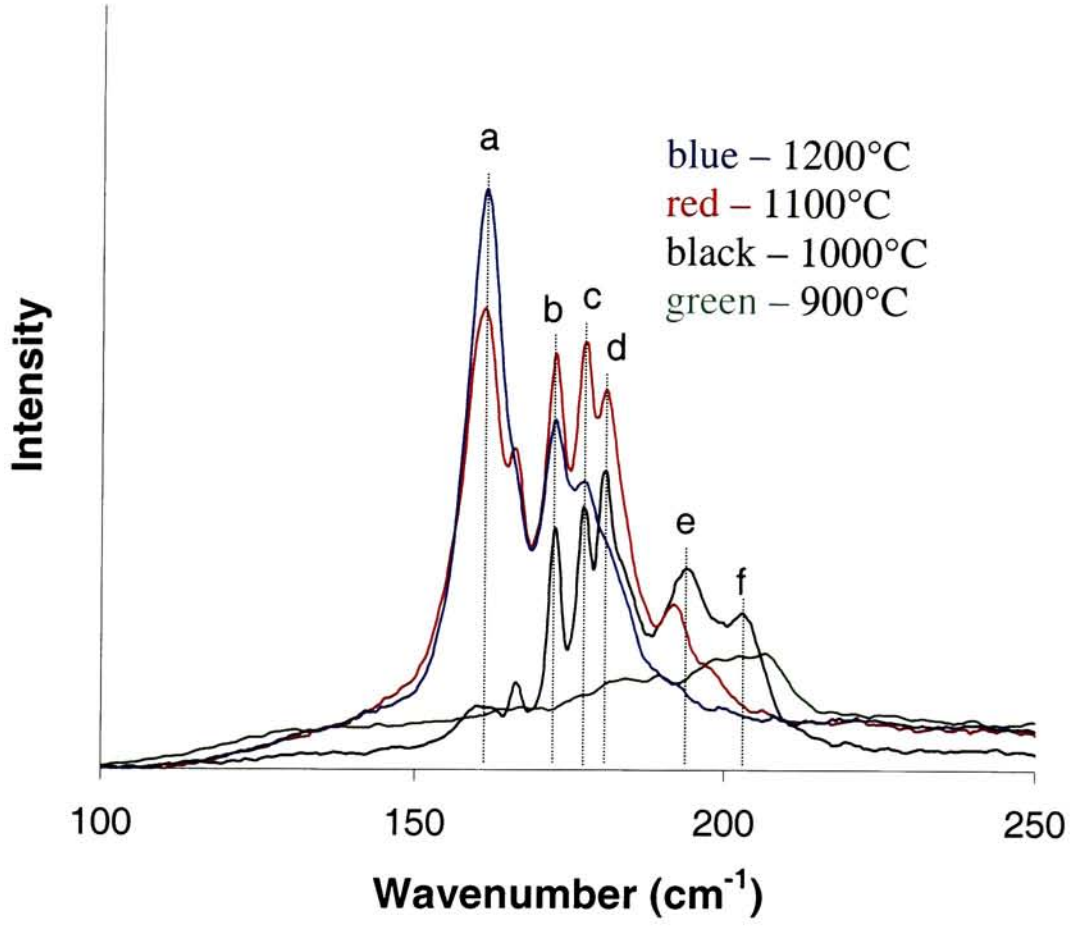

Figure 30: RBM region of Raman spectra for SWNT material synthesized at various temperatures. Excitation wavelength = 488 nm. Higher synthesis temperatures yield material with peaks at lower wave numbers indicating larger diameter.

Peak	Wavenumber (cm^{-1})	Corresponding diameter[59] (nm)
a	161.8	1.38
b	172.6	1.30
c	177.7	1.26
d	180.8	1.24
e	194.8	1.15
f	203.6	1.10

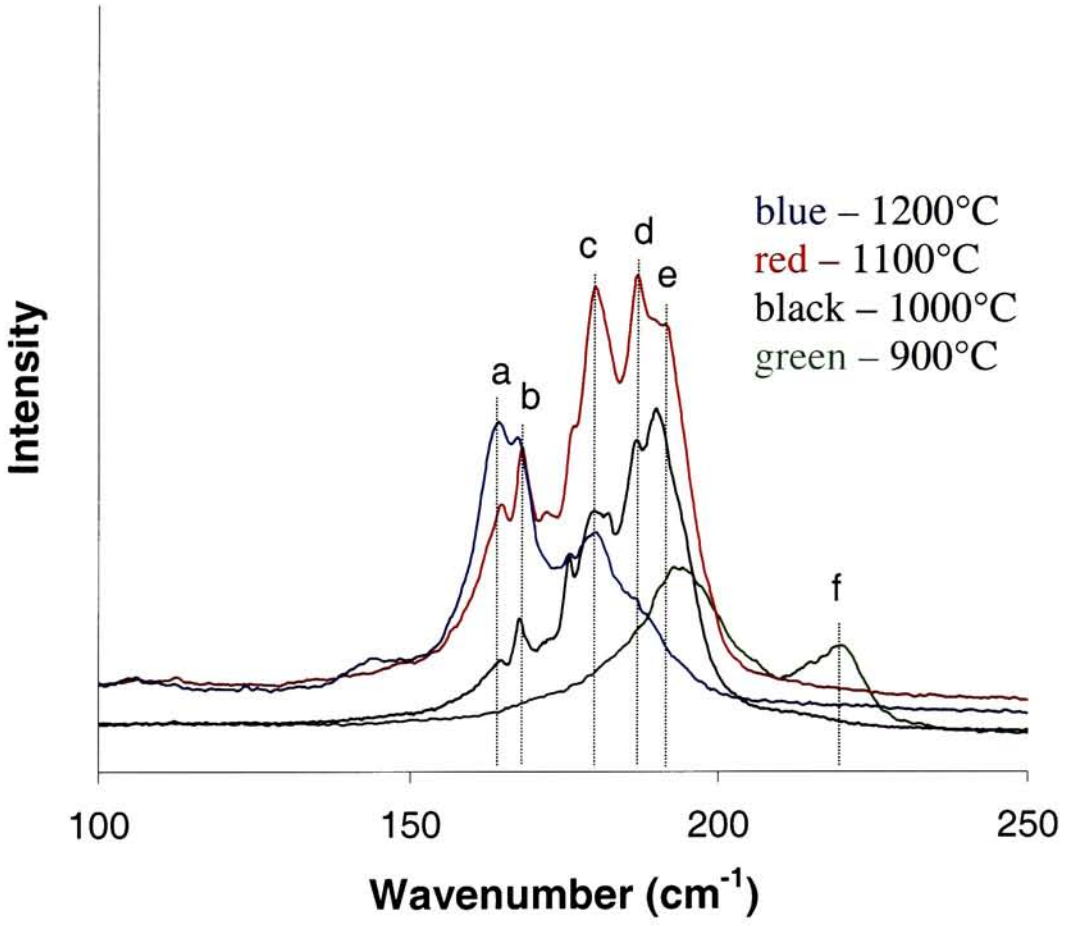

Figure 31: RBM region of Raman spectra for SWNT material synthesized at various temperatures. Excitation wavelength = 633 nm. Metallic SWNTs similarly show shifts to lower wave numbers for higher synthesis temperatures indicating larger diameters.

Peak	Wavenumber (cm^{-1})	Corresponding diameter[59] (nm)
a	164.9	1.36
b	168.3	1.33
c	180.3	1.24
d	187.0	1.20
e	192.0	1.17
f	221.1	1.01

488 nm excitation the predominant diameters for the 1200°C synthesis are 1.38 nm and 1.30 nm whereas for the 900°C synthesis the predominant diameter is around 1.10 nm. The D/G ratios, shown in Table 6, indicate the largest amount of disordered sp^2 carbon for 900°C.

Table 6: D/G ratios for materials synthesized using temperature variation

Temperature	488 nm Excitation			633 nm Excitation		
(°C)	**D**	**G**	**D/G**	**D**	**G**	**D/G**
900	824.6	3705.9	0.2225	2561	5223.3	0.4903
1000	165.3	7723.7	0.02140	606.2	2835.6	0.2138
1100	464.9	18708.3	0.02485	1378	6998.4	0.1969
1200	472.3	17329.3	0.02725	1760.	8317	0.2116

Figures 32 and 33 display the results of the TGA thermograms of SWNTs produced under these temperatures. The onset of thermal decomposition tends to occur at lower temperatures for materials synthesized at lower temperatures. The synthesis temperature that produces SWNTs that decompose at the highest temperature is 1100°C. Spectroscopic results indicate that an increase in reactor temperature results in increase in SWNT diameters. The UV-vis-NIR spectra, shown in Figure 34, clearly demonstrate the shift to lower wavelength in the first Van Hove peak with decreasing temperature. Spectra taken from the sample synthesized at 900°C has substantially less peak definition and clarity. The most likely reasons for the attenuation of signal in both types of spectra is lower yield and higher defect densities. The SEM micrographs shown in Figure 35 show a significantly reduced number of SWNT bundles at 900°C compared with the other synthesis temperatures. Although SEM probes only an extremely small portion of the total material produced, the images presented provide support along with the spectra obtained.

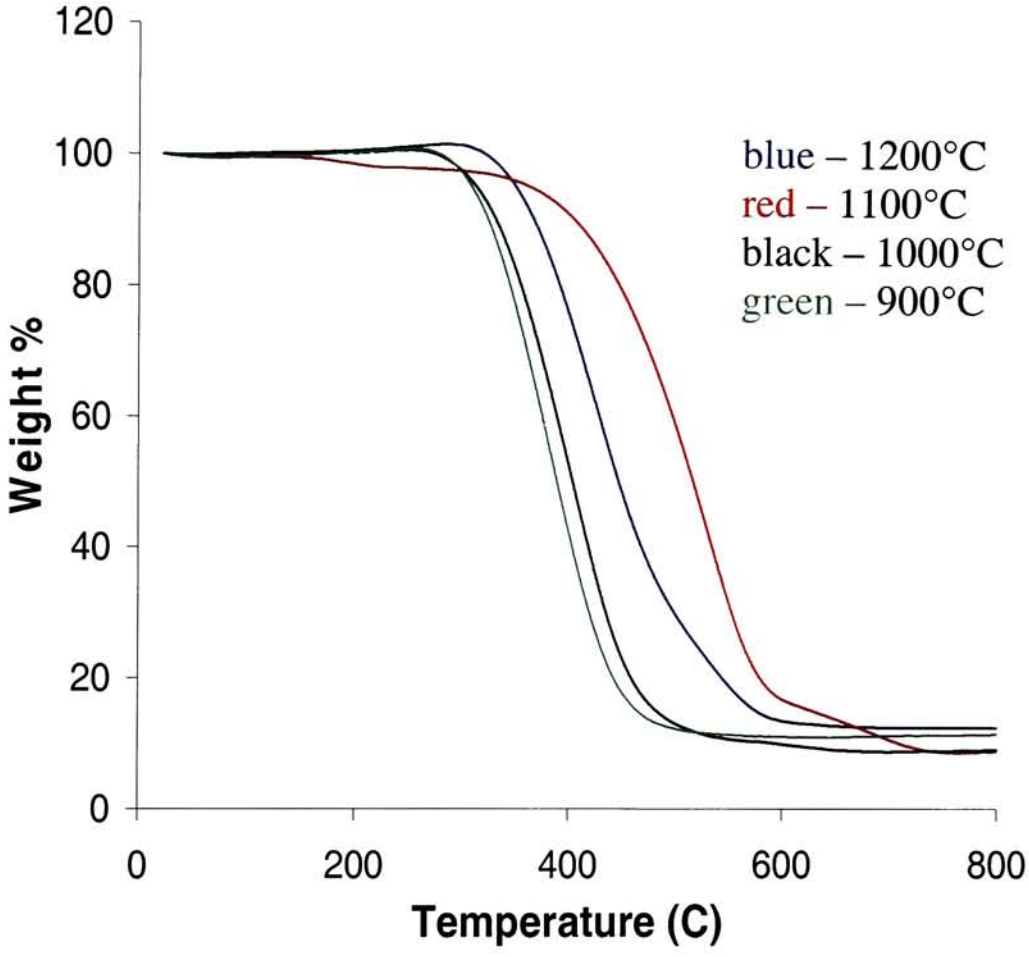

Figure 32: TGA overlay of as-produced SWNT materials at 900, 1000, 1100, and 1200°C. This overlay represents thermal oxidation at the specified temperatures.

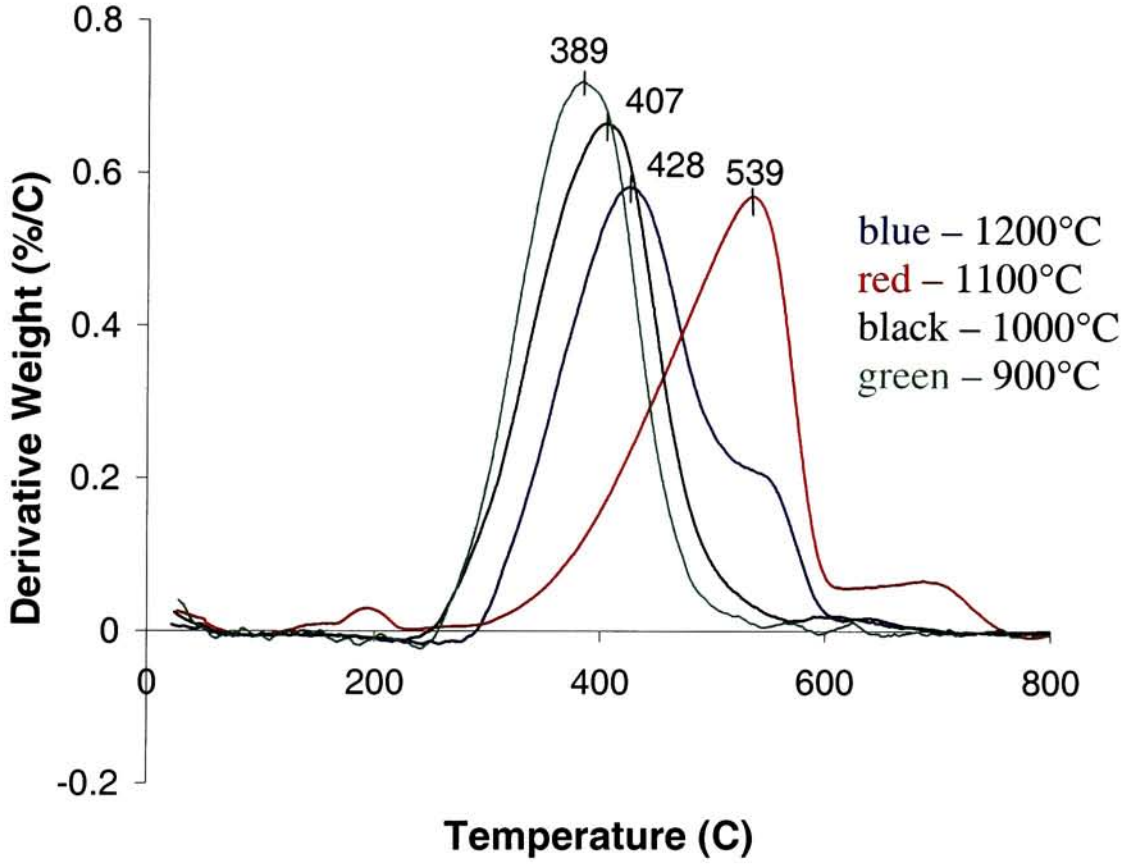

Figure 33: Overlay of the first derivative plots from the TGA data of synthesis carried out at various temperatures.

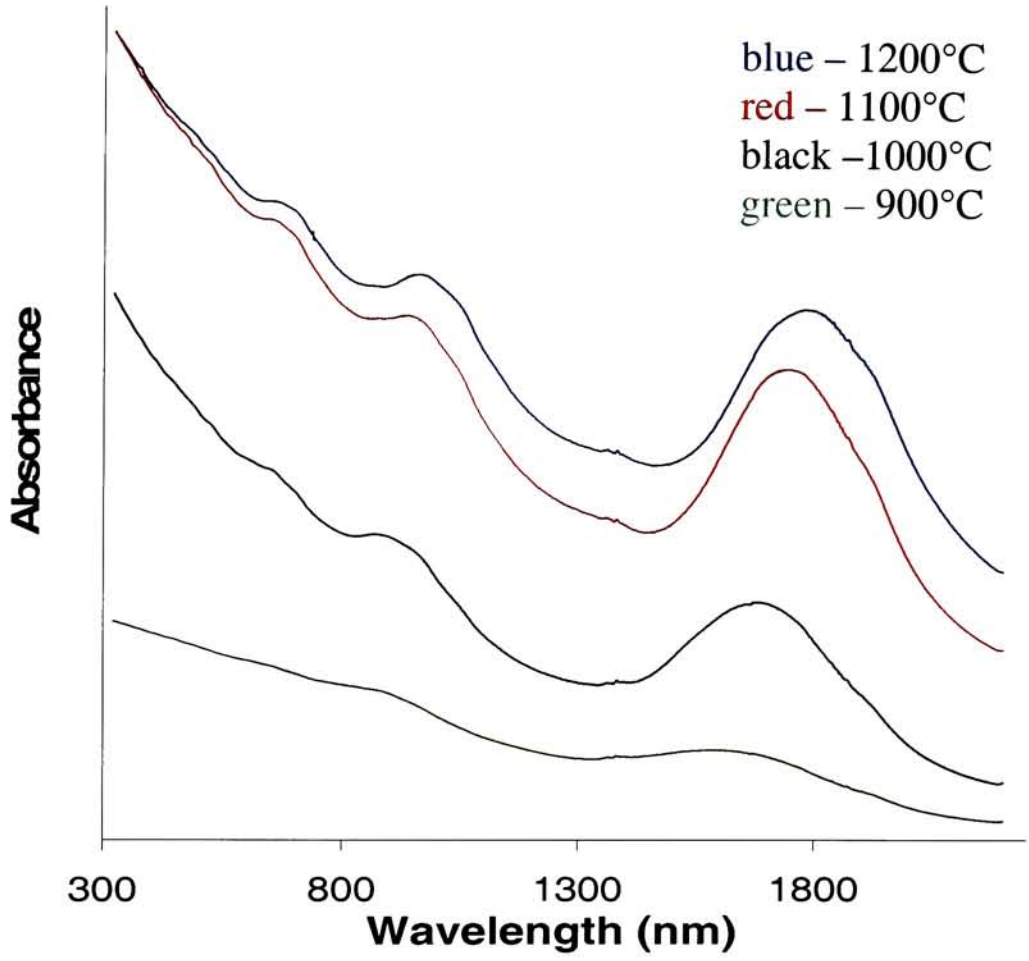

Figure 34: Overlay of UV-vis-NIR spectra of as-produced SWNT material synthesized at various temperatures.

Temperature (°C)	First Van Hove peak (nm)	Corresponding diameter[16] (nm)
900	1820	1.46
1000	1758	1.41
1100	1687	1.36
1200	1599	1.29

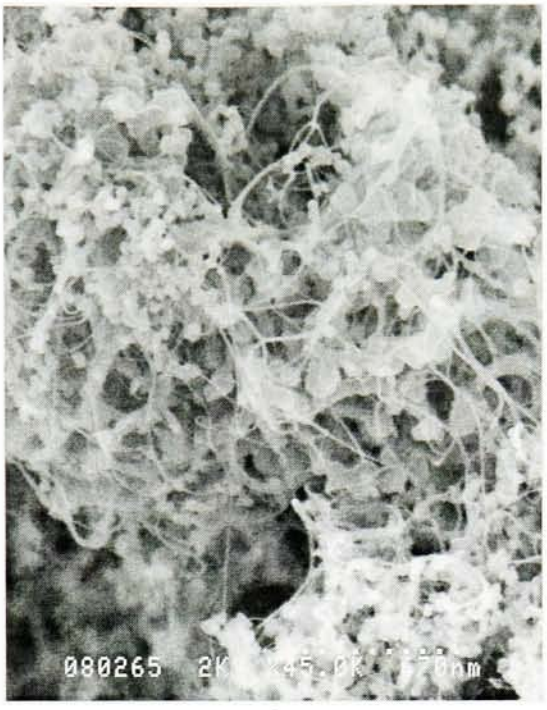

a

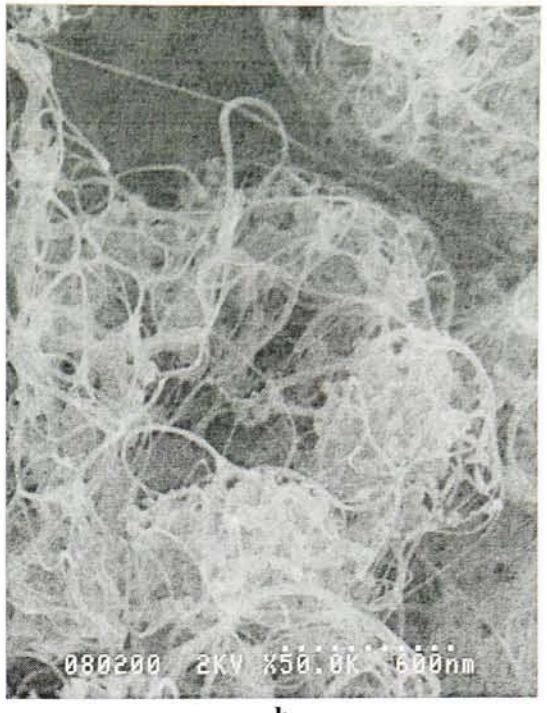

b

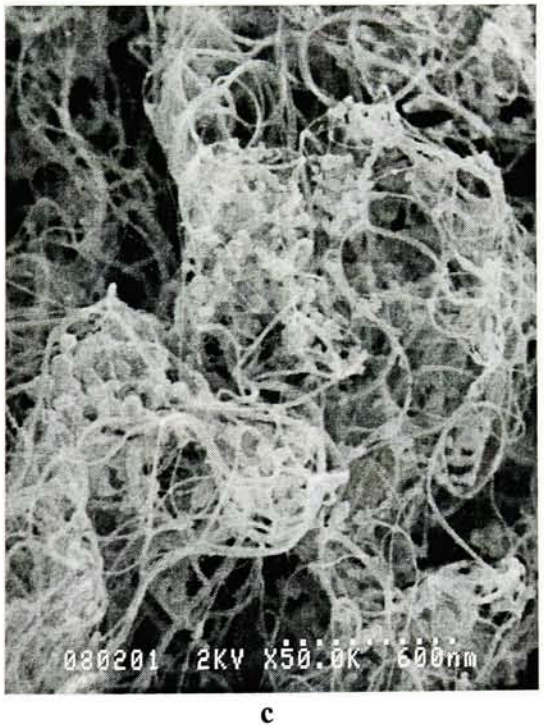

c

d

Figure 35: Representative SEM micrographs of as-produced SWNT material synthesized at various temperatures. a) 900°C b) 1000°C c) 1100°C d) 1200°C.

3.3 Variation in Graphite Particle Size

Effects of the particle size of graphite in the target were examined in order to determine variability in production rate, yield, and amount of graphitic material in the product. Two different graphite particle sizes were investigated along with a 1:1 mixture of both particles sizes. The targets studied, therefore, consisted of graphite with a particle size of 1-2 μm, 45 μm, and a 1:1 mixture of both 1-2 μm and 45 μm. Raman spectra of the SWNT materials produced from these syntheses (Figures 36-39) show similar diameter distributions for material synthesized with 1-2 μm graphite and a 1:1 mixture of 1-2 μm and 45 μm. Spectra acquired at both 488 nm and 633 nm are similar in their RBM portion, however, there is a slight shift to higher wavenumbers for the 45 μm graphite. In the spectrum acquired at 488 nm the predominant diameters from all of the SWNTs are in the range of 1.26-1.39 nm. The material synthesized with 1-2 μm graphite displays its largest peak corresponding to 1.39 nm and the material synthesized with 45 μm graphite displays its largest peak corresponding to 1.30 nm. Similarly, in the spectrum acquired at 633 nm the 1-2 nm graphite displays a predominant peak corresponding to SWNTs with a diameter of 1.36 nm with a small shoulder peak corresponding to 1.54 nm. The material synthesized with 45 μm graphite displays a predominant peak corresponding to 1.34 nm. The D/G ratios found in these Raman spectra are displayed in Table 7. The greatest D/G ratio for the 488 nm excitation is for the 45 μm size graphite. For 633 nm excitation, however, the 50/50 mixture shows the greatest value. In both cases the 1-2 μm graphite yields the material with the smallest amount of disordered carbon.

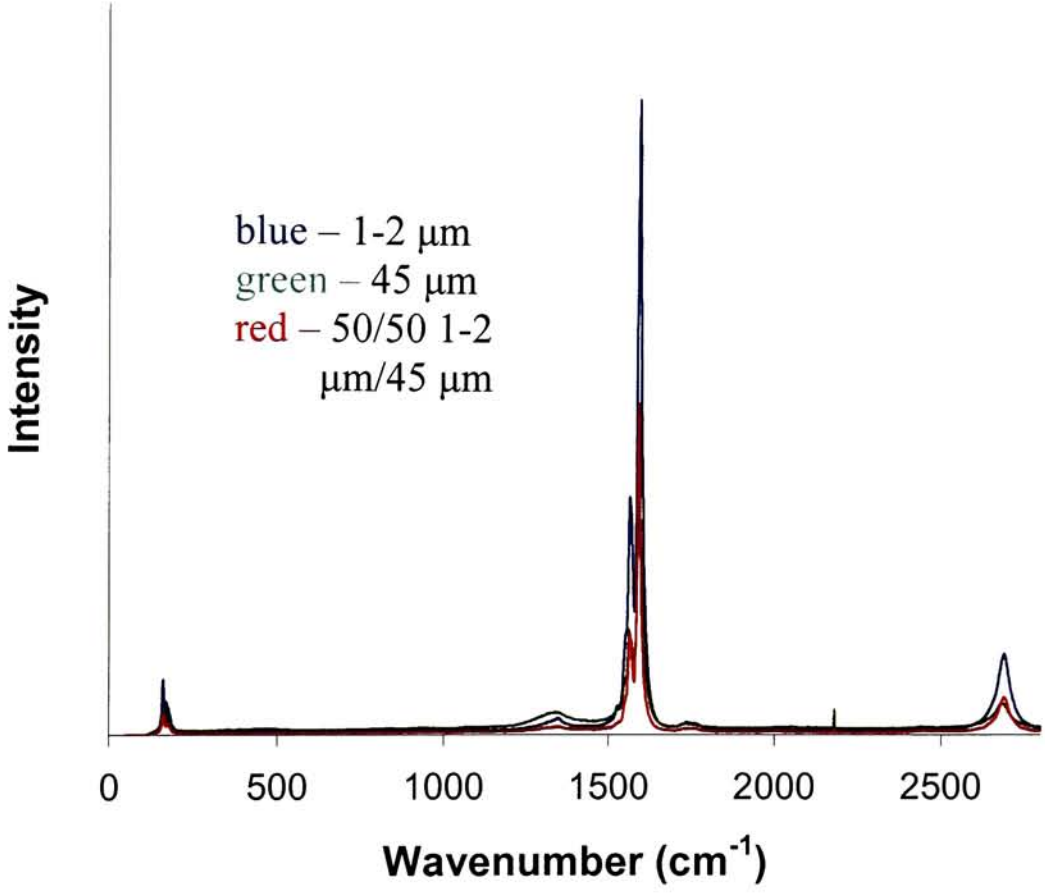

Figure 36: Overlay of Raman spectra taken of SWNT materials synthesized with varying graphite particle sizes. Excitation wavelength = 488 nm.

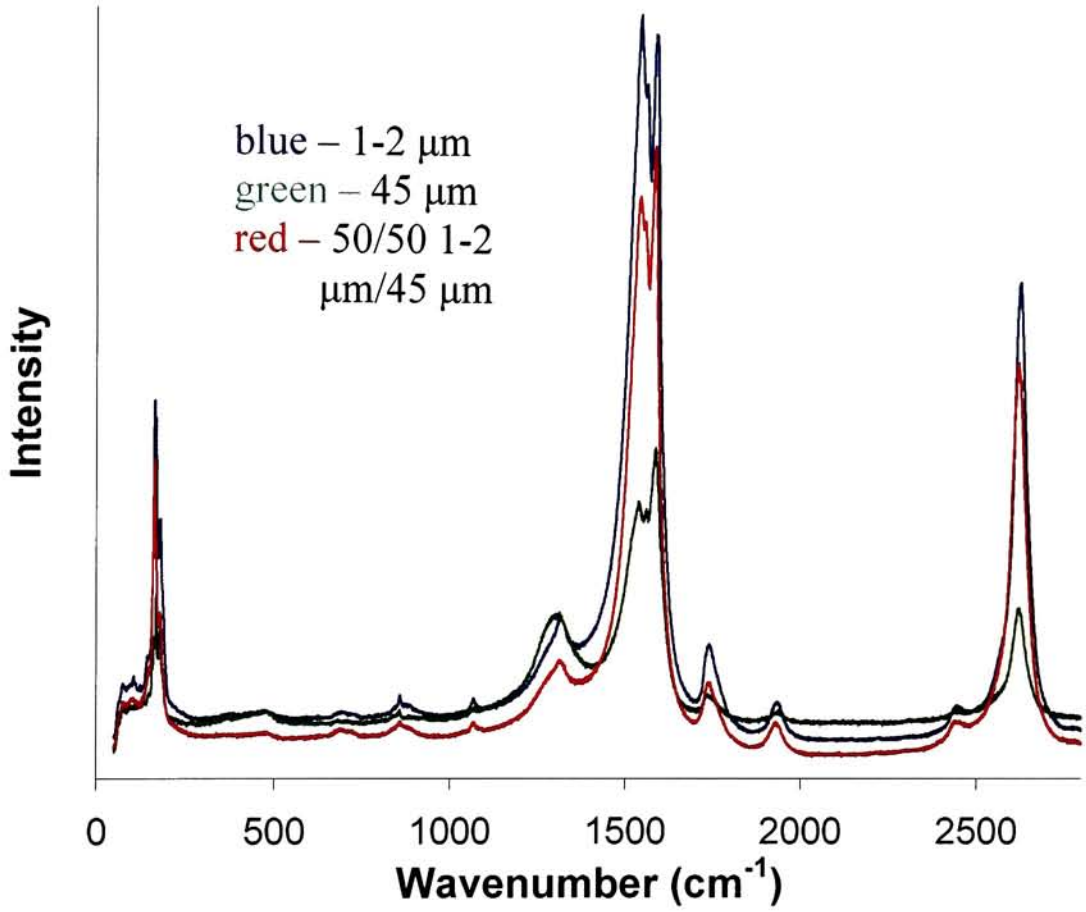

Figure 37: Overlay of Raman spectra taken of SWNT materials synthesized with varying graphite particle sizes. Excitation wavelength = 633 nm.

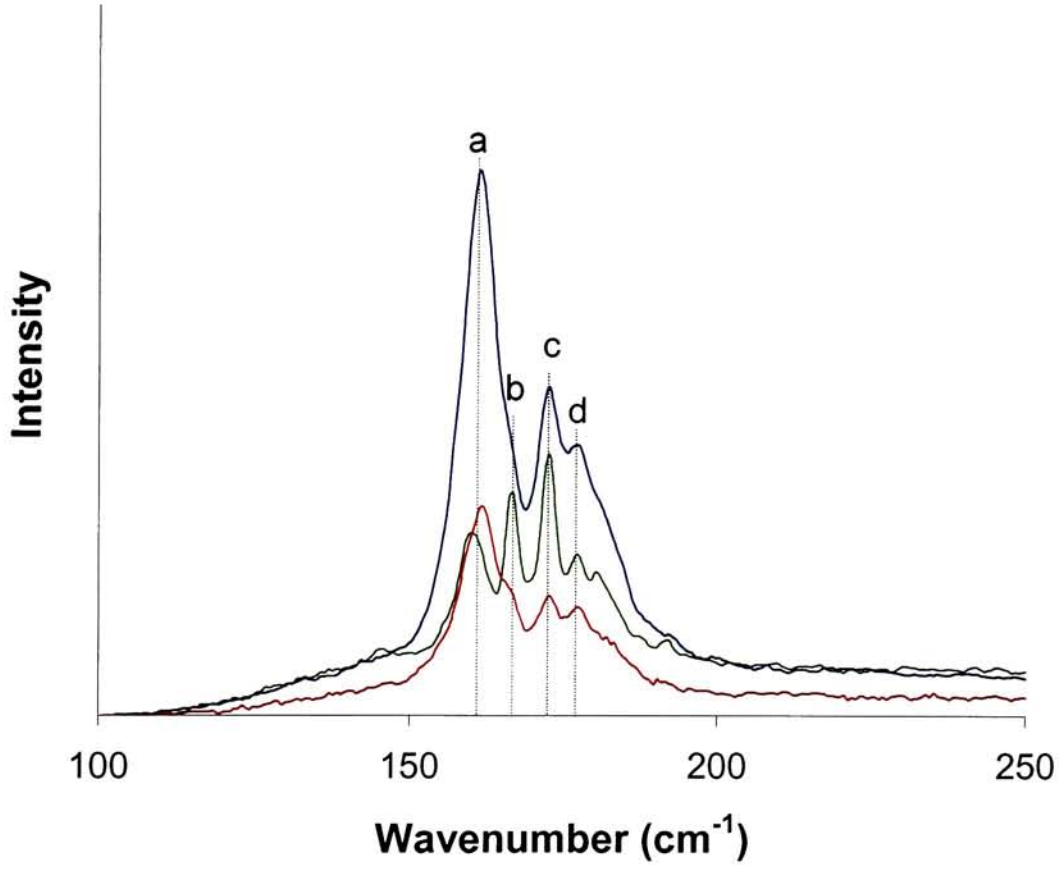

Figure 38: Raman RBM overlay for materials synthesized with different graphite particle sizes. Excitation wavelength = 488 nm.

Peak	Wavenumber (cm^{-1})	Corresponding diameter[59] (nm)
a	161.2	1.39
b	166.9	1.34
c	172.6	1.30
d	177.7	1.26

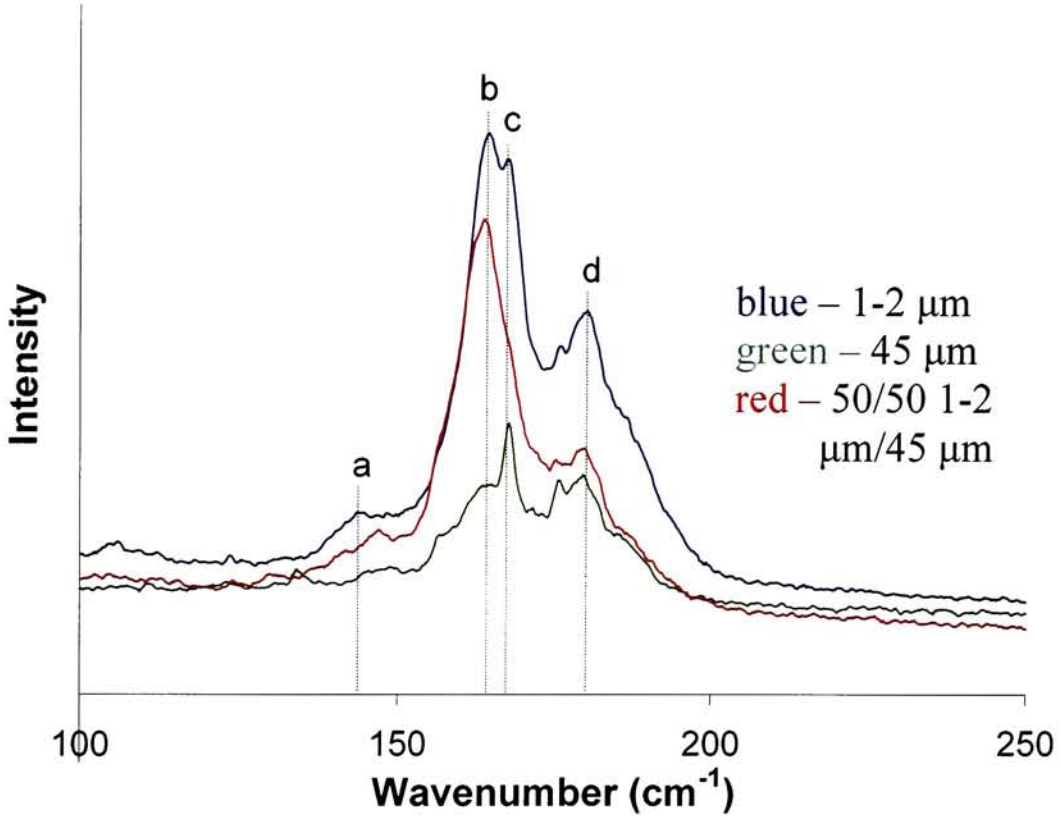

Figure 39: Raman RBM overlay for material synthesized with different graphite particle sizes. Excitation wavelength = 633 nm.

Peak	Wavenumber (cm^{-1})	Corresponding diameter[59] (nm)
a	145.2	1.54
b	165.0	1.36
c	167.6	1.34
d	180.6	1.24

Table 7: D/G ratios for graphite particle size variation

Particle Size (μm)	488 nm Excitation			633 nm Excitation		
	D	G	D/G	D	G	D/G
1-2	472.3	17329.3	0.02725	1760.	8317	0.2116
45	637.6	6840.	0.09322	1086	4162	0.2609
50/50 mix	236.0	9052.6	0.02607	787.3	2185	0.3603

The TGA thermograms (Figures 40 and 41) indicate the onset and course of thermal decomposition is quite similar for all these variations. The first derivative overlay shows a well defined transition corresponding to SWNTs for the 1-2 μm graphite at a temperature of about 550°C. The 1-2 μm graphite also displays a larger metal oxide residue after the thermal oxidation has taken place. The UV-Vis-NIR spectra (Figure 42) show the most well defined peaks for the 1-2 μm graphite. Similarly, there is no appreciable shift in the first Van Hove peak indicating that a change in diameter distribution is not detectable using UV-Vis-NIR spectroscopy. SEM images of the materials synthesized with different graphite particle sizes (Figure 43) show that nanotube bundles are present for all three syntheses.

3.4 Variation in Reactor Chamber Configuration

3.4.1 Chamber Volume

Variation in reactor chamber volume was investigated in order to ascertain the effect on the quality and yield of the synthesized SWNTs. It was thought that a reduction in the size of the chamber would lead to a decreased volume available to the plume and therefore less time would be spent by the plume in the chamber before condensation. The volume of the chamber was reduced from 2.4 L to 1.6 L for this study. The Raman spectra of the SWNT materials synthesized using these two chamber volumes (Figures 44-47) show that the diameter distributions of these two materials are similar. The RBM

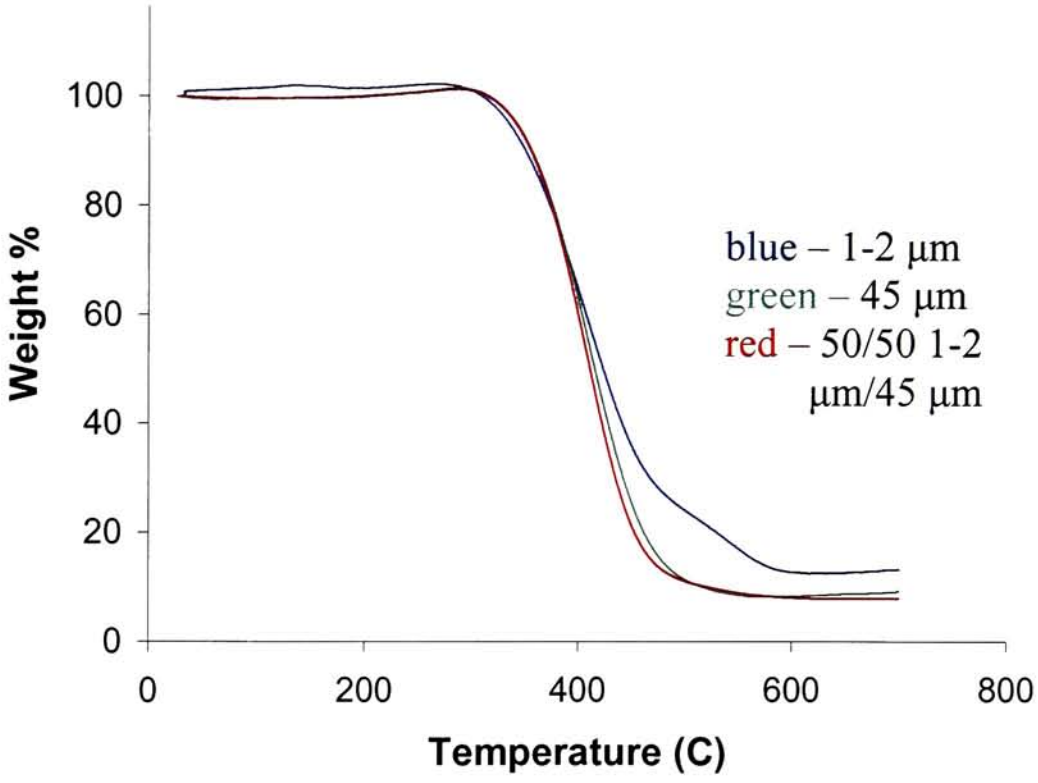

Figure 40: TGA overlay for material produced with varying graphite particle size.

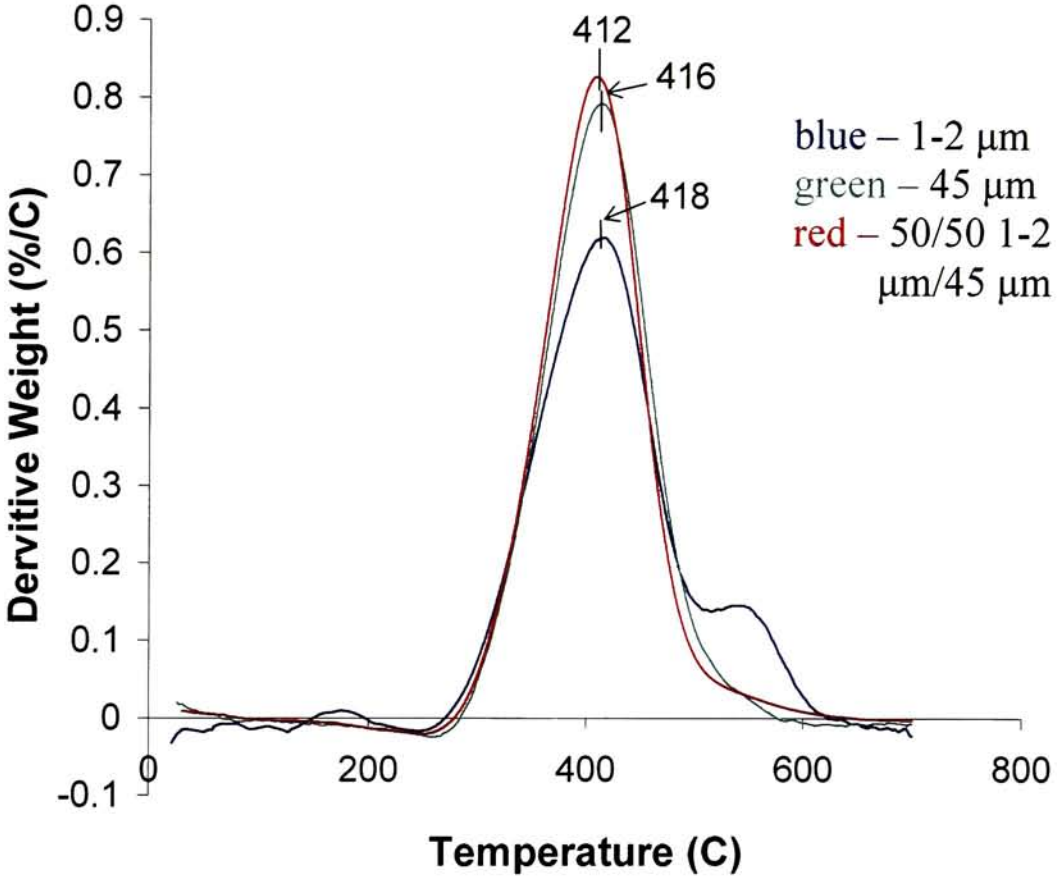

Figure 41: First derivative TGA overlay for materials synthesized with different graphite particle sizes.

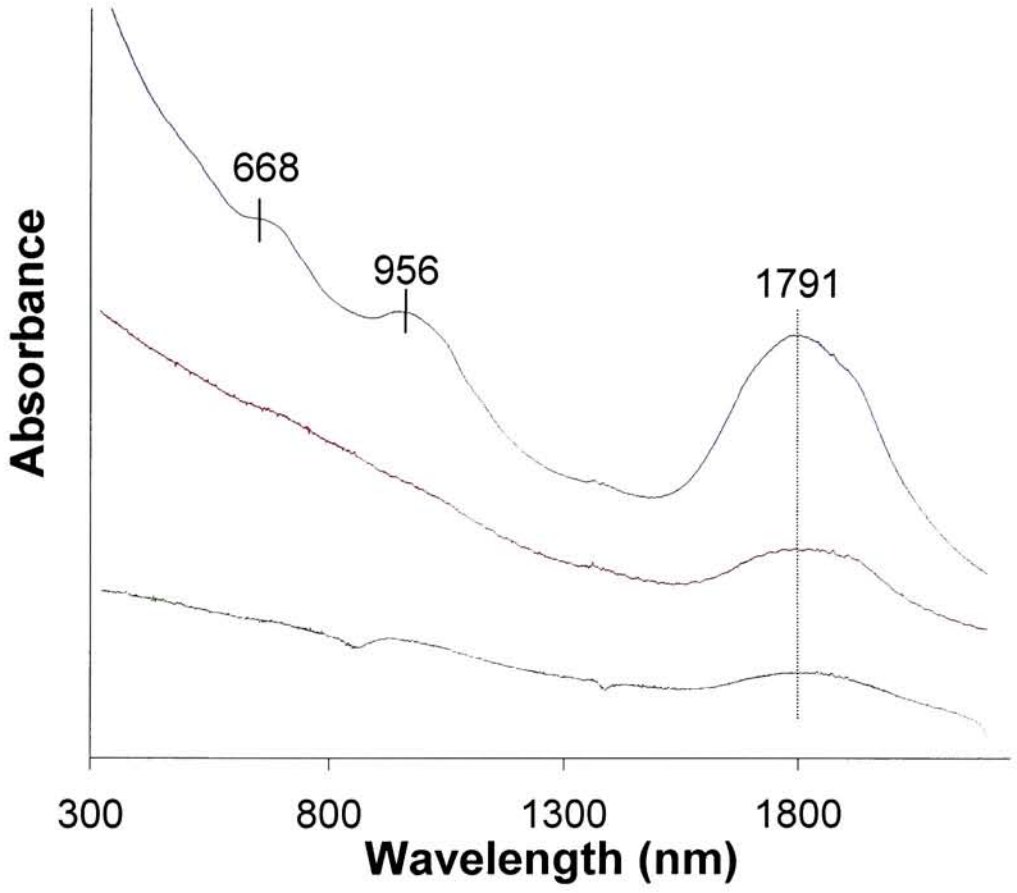

Figure 42: Overlay of UV-Vis-NIR spectra from materials synthesized with varying graphite particle size.

Particle Size (μm)	First Van Hove Peak (nm)	Corresponding diameter[16] (nm)
1-2, 45, 1:1 mixture	1791	1.44

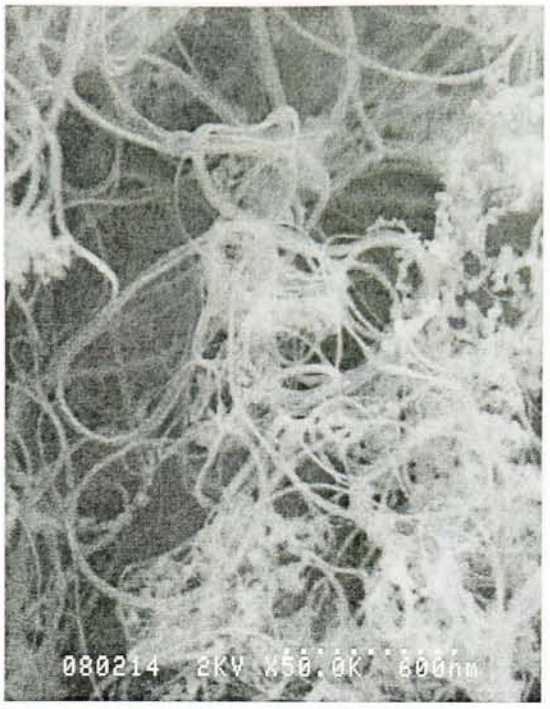

a

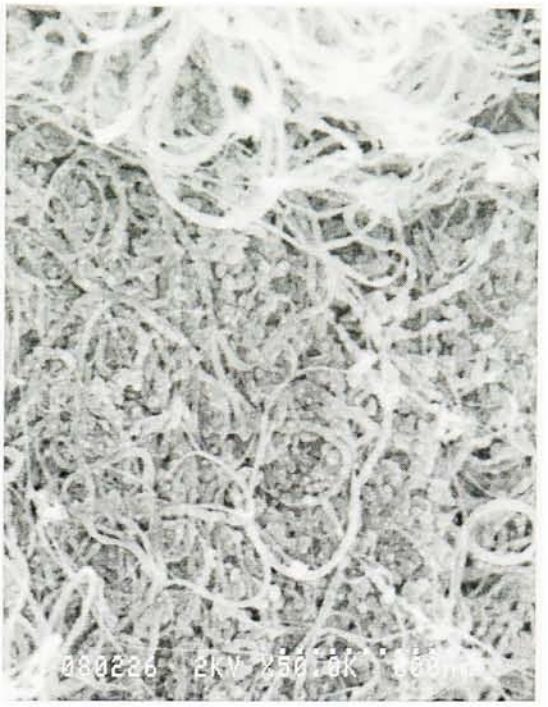

b

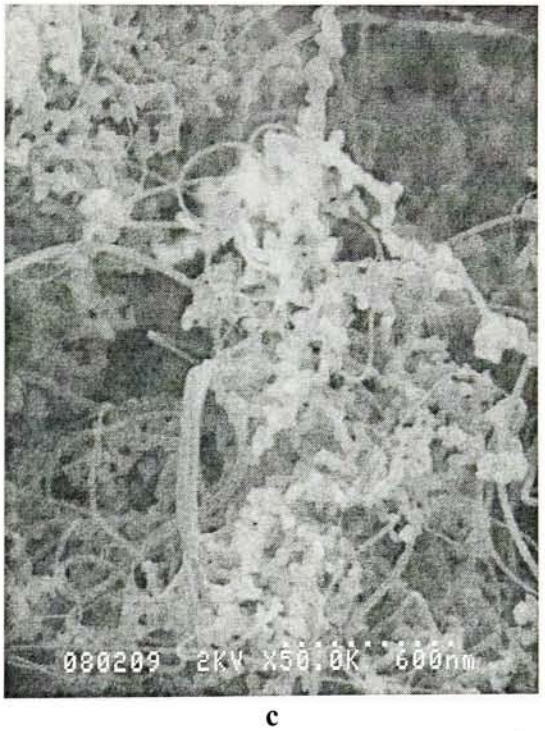

c

Figure 43: Representative SEM micrographs of material synthesized with various graphite particle sizes. a) 1-2 μm b) 45 μm c) 50/50 mixture

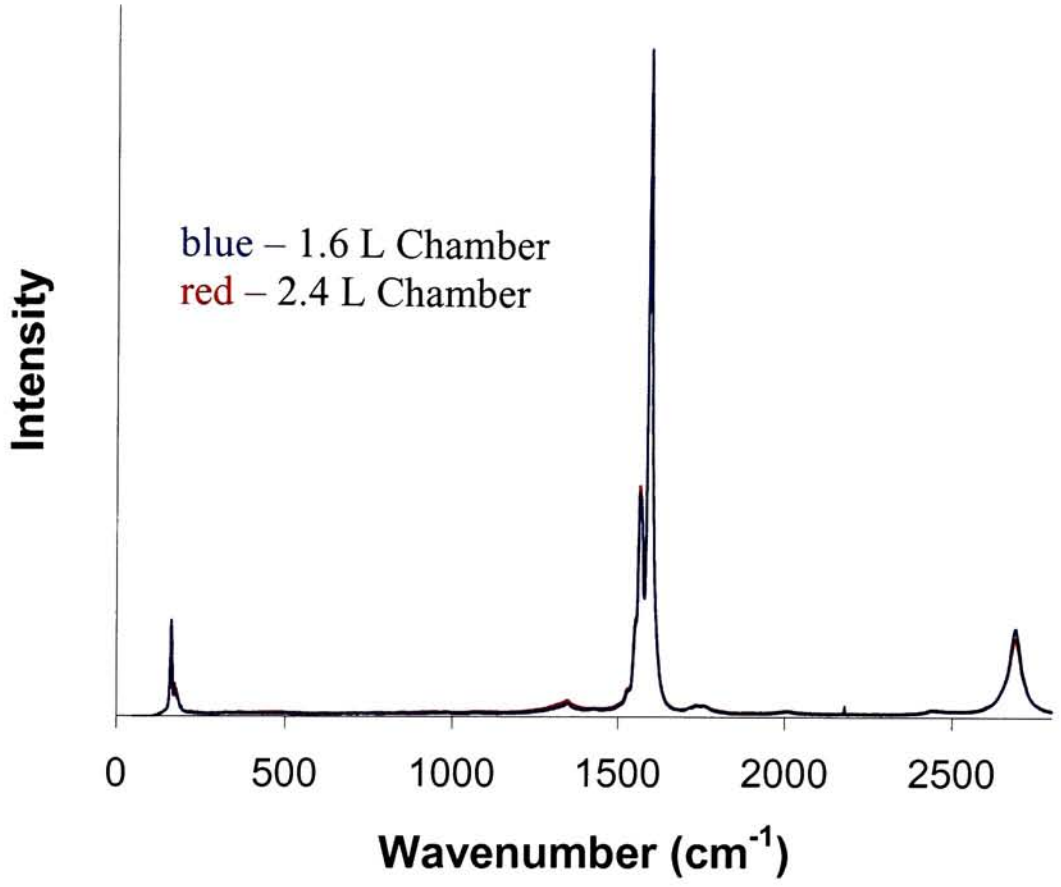

Figure 44: Overlay of Raman spectra taken of SWNT materials synthesized with varying chamber volumes. Excitation wavelength = 488 nm.

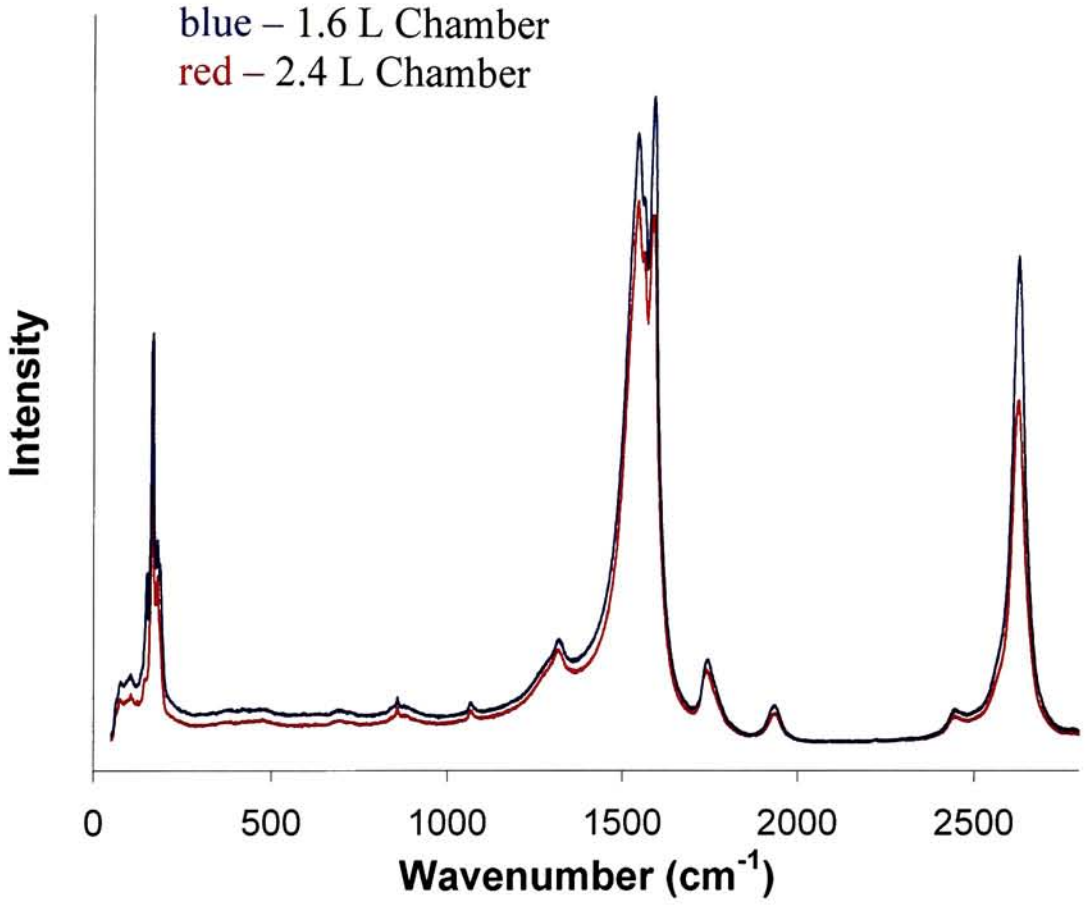

Figure 45: Overlay of Raman spectra taken of SWNT materials synthesized with varying chamber volumes. Excitation wavelength = 633 nm.

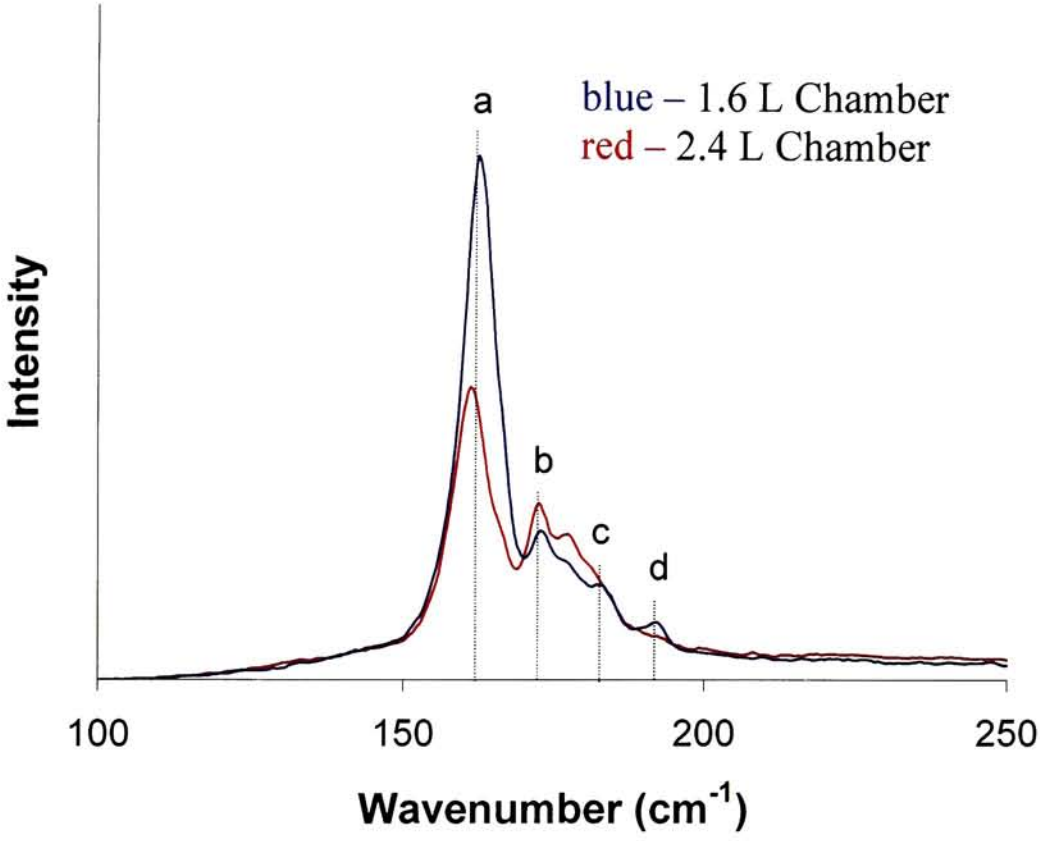

Figure 46: Raman RBM overlay for material synthesized using different chamber volumes. Excitation wavelength = 488 nm.

Peak	Wavenumber (cm^{-1})	Corresponding diameter[59] (nm)
a	162.4	1.38
b	173.2	1.29
c	184.0	1.22
d	192.9	1.16

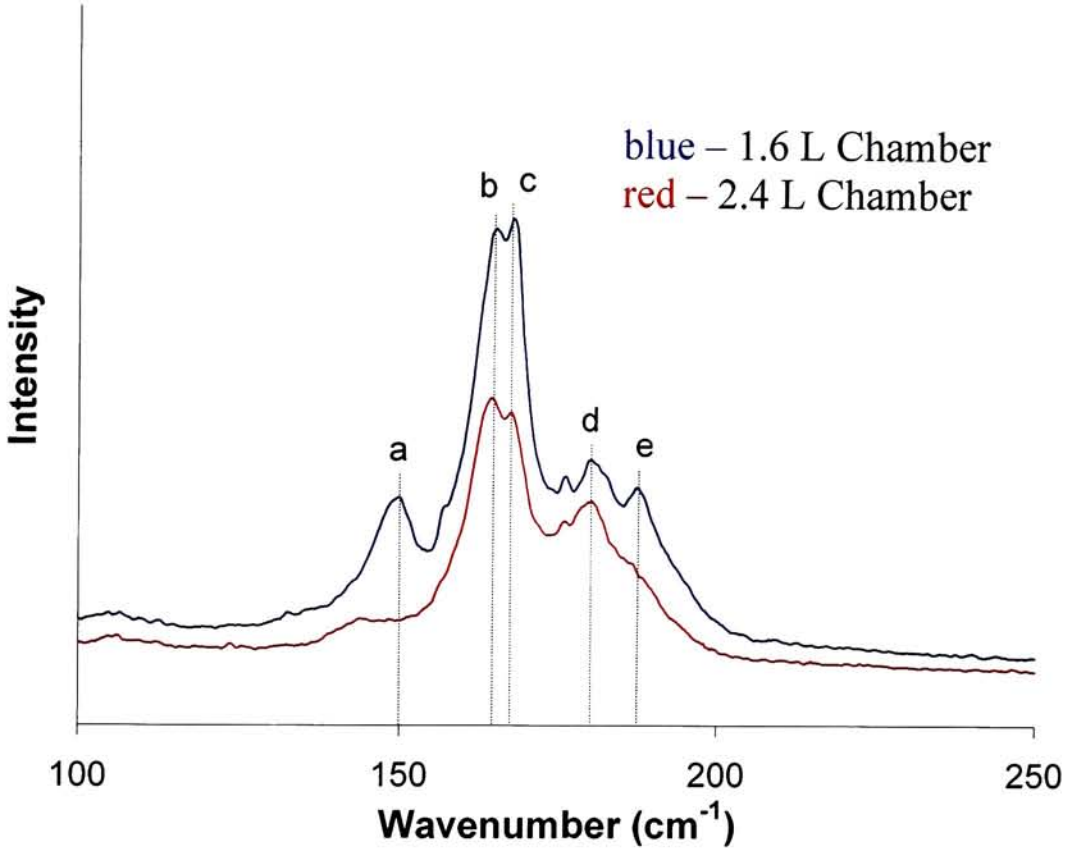

Figure 47: Raman RBM overlay of SWNTs synthesized with different chamber volumes. Excitation wavelength = 633 nm.

Peak	Wavenumber (cm^{-1})	Corresponding diameter[59] (nm)
a	150.2	1.49
b	165.6	1.35
c	168.0	1.33
d	180.6	1.24
e	188.0	1.19

portion of the spectrum for 488 nm excitation shows a narrow distribution of diameters with the peak corresponding to 1.38 nm, at 162.4 cm^{-1}, being the most prominent for the 1.6 L chamber synthesis. The 2.4 L chamber similarly has its predominant peak corresponding to 1.38 nm, however, another peak corresponding to 1.29 nm is present. The RBM portion of the spectra for 633 nm excitation shows broader distributions of diameters than the 488 nm spectra. The diameter distributions both show predominant diameters of 1.24, 1.33, and 1.35 nm for both diameters. D/G ratios for these materials synthesized using two different reactor chamber volumes are shown in Table 8. Spectra acquired at both excitation wavelengths indicate a higher amount of disordered carbon for the 2.4 L chamber synthesis.

Table 8: D/G ratios for materials synthesized with different reactor chamber volumes

Chamber Volume (L)	488 nm Excitation			633 nm Excitation		
	D	**G**	**D/G**	**D**	**G**	**D/G**
1.6	380.2	18759.2	0.02027	1912	9861.7	0.1939
2.4	472.3	17329.3	0.02725	1760.	8317	0.2116

TGA thermograms (Figures 48 and 49) of the materials synthesized with different chamber volumes show the onset of thermal decomposition occurs at about 300°C for both samples. The metal residue present for the 2.4 L chamber is twice the amount of metal residue for the 1.6 L chamber. The first derivative curves show a shoulder peak for the 2.4 L chamber volume, whereas the 1.6 L chamber displays only one peak. Figure 50 displays the UV-Vis-NIR spectra for both of these SWNT samples. The first Van Hove peaks for both samples are at 1790 nm, corresponding to an SWNT diameter of 1.44 nm. These data correspond well with the Raman data to conclude that reducing the chamber volume to 1.6 L does not change the SWNT diameters to any appreciable extent. SEM

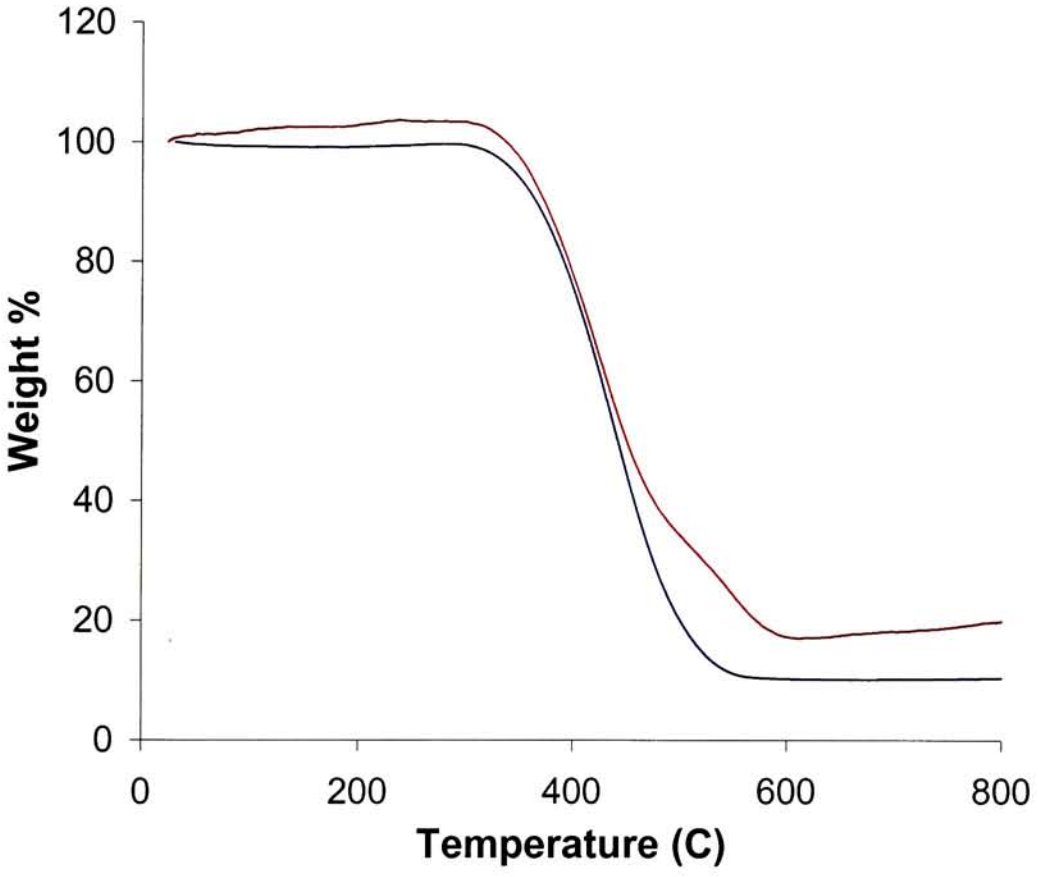

Figure 48: TGA overlay for SWNTs synthesized using different chamber volumes.

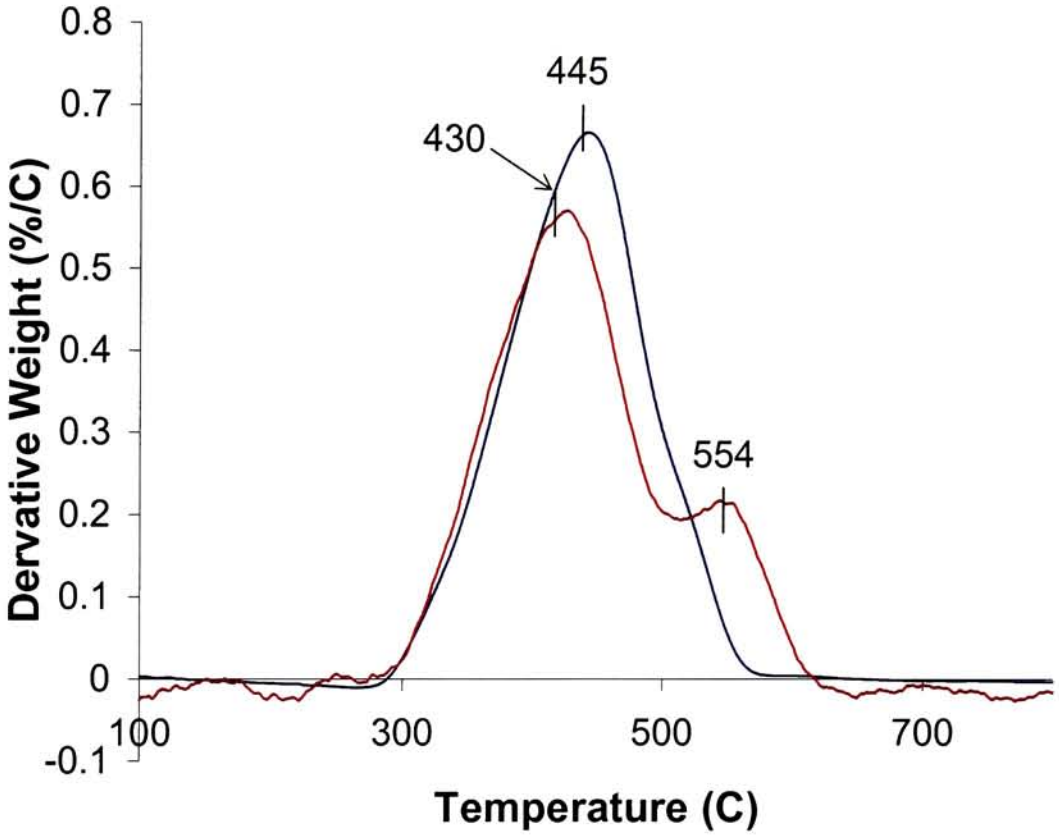

Figure 49: First derivative TGA overlay for SWNTs synthesized at different reactor chamber volumes.

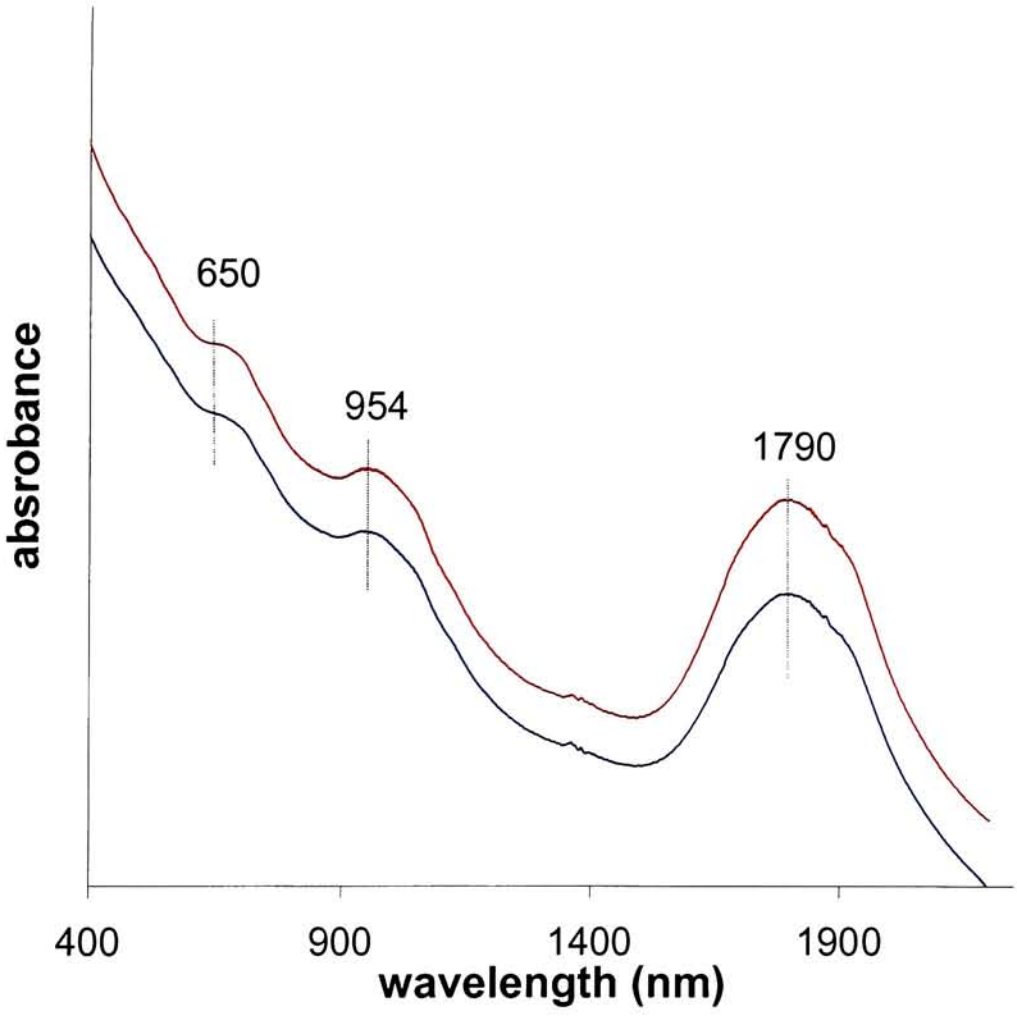

Figure 50: UV-Vis-NIR spectra for SWNT material produced using different chamber volumes.

Chamber Volume (L)	First Van Hove Peak (nm)	Corresponding diameter[16] (nm)
1.6, 2.4	1790	1.44

images of the materials synthesized at 1.6 L and 2.4 L chamber volumes are shown in Figure 51. SWNT bundles are present in both samples.

3.4.2 Various Collection Regions

In an attempt to confine the plume in front of the target so that subsequent laser pulses anneal and promote further SWNT growth, a second smaller inner quartz flow tube was introduced inside of the main reactor quartz tube. With the inner flow tube, the ejected material from the surface of the target will spend more time in the reactor chamber and further heating will occur. The inner diameter of this smaller quartz tube is 30 mm which matches the diameter of the target. One synthesis was performed in this manner. During the course of the synthesis portions of product were deposited in the front of the flow tube and in main reactor tube in addition to the main location at the rear of the reactor tube. Figure 52 displays a schematic of the setup of the dual reactor tubes used for this synthesis. The respective production rates are 40 mg/hr for the rear (carpet), 5 mg/hr at the front, and 2 mg/hr in the main tube (coil). Analysis was performed on the SWNT material collected from each of these regions.

Raman spectra of the SWNT materials collected from these different regions (Figures 53-56) indicate a similar diameter distribution in all of the samples. The RBM portion of the spectra for 488 nm excitation shows predominant diameters in the range of 1.24 to 1.39 nm for all samples. The spectra acquired at 633 nm show the SWNT diameters in the range of 1.20 to 1.36 nm. Table 9 displays the D/G ratios for the various collection regions. The TGA data, displayed in Figures 57 and 58, show drastically different behavior in the thermal decomposition for each collection region. The onset of thermal decomposition occurs earliest for the traditional carpet material. The material

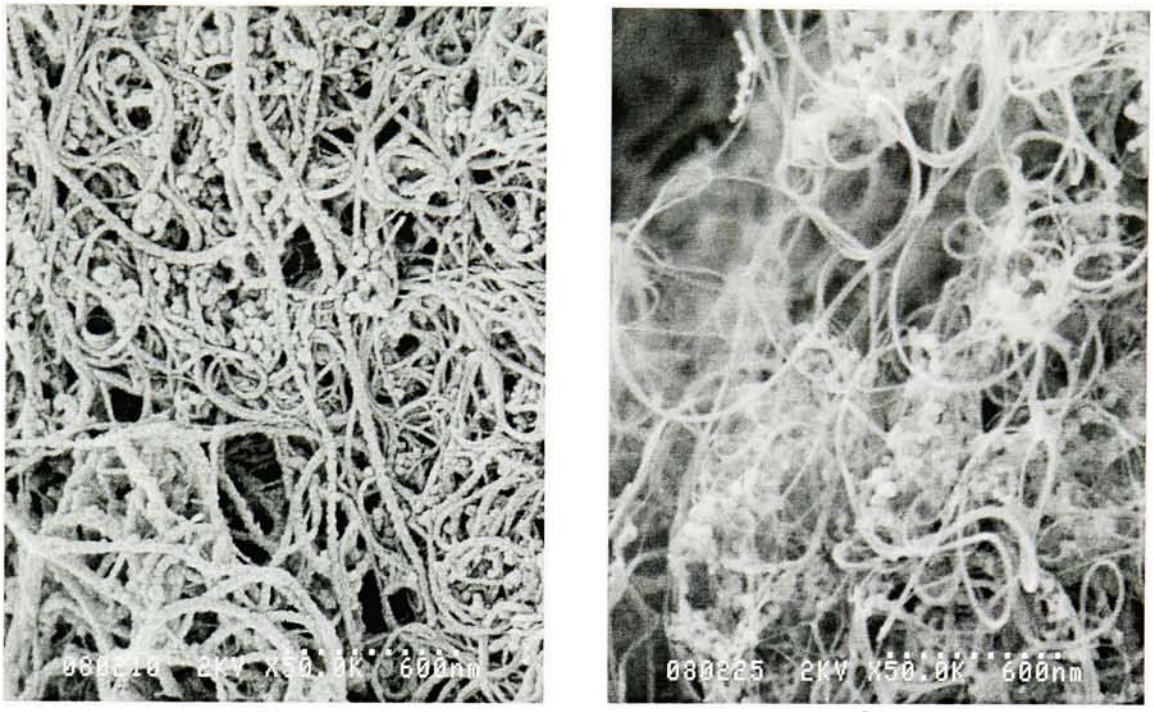

a b

Figure 51: Representative SEM micrographs of SWNTs produced using a variation in reactor chamber volume. a) 1.6 L chamber b) 2.4 L chamber

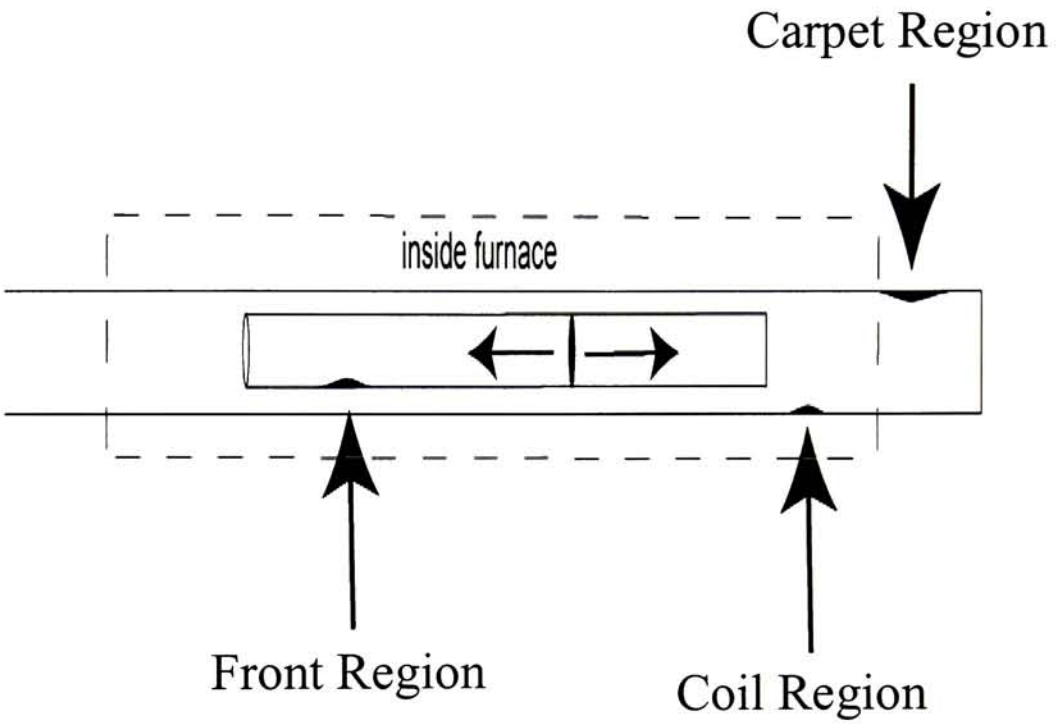

Figure 52: Diagram of the collection regions in the reactor chamber.

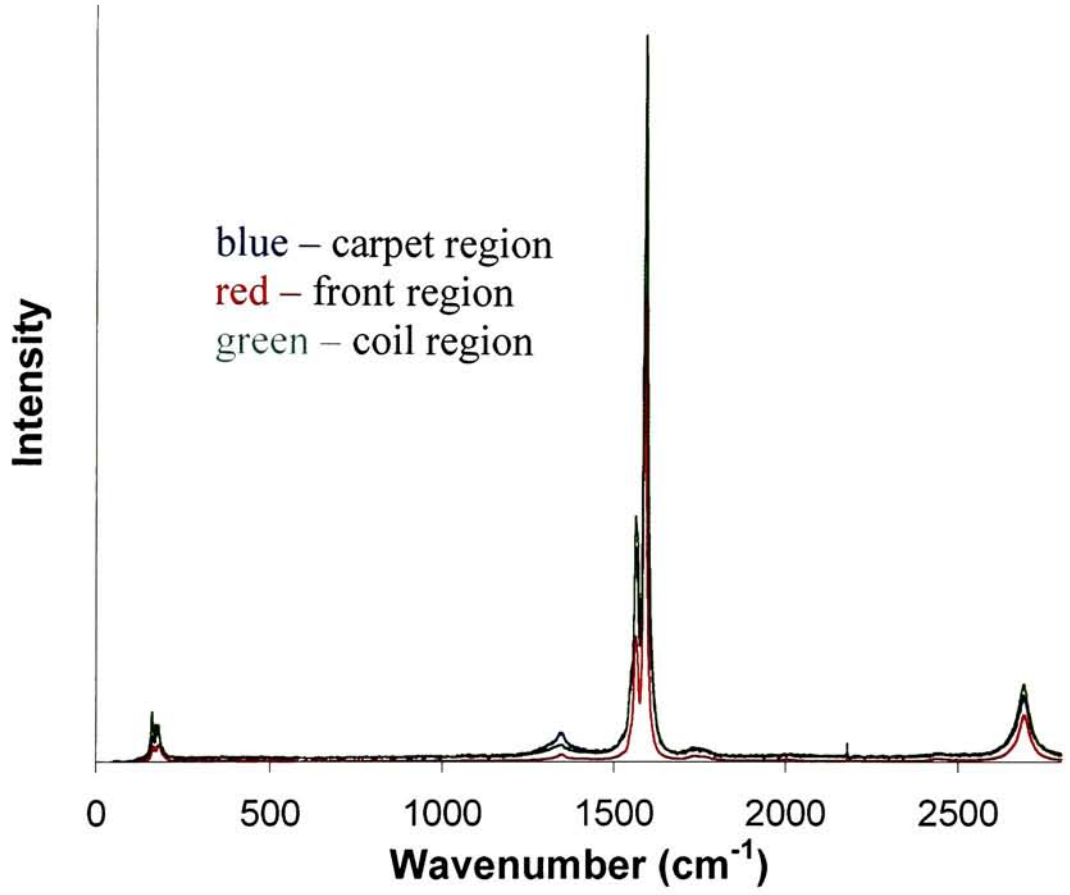

Figure 53: Overlay of Raman spectra taken of SWNT materials collected from different chamber regions. Excitation wavelength = 488 nm.

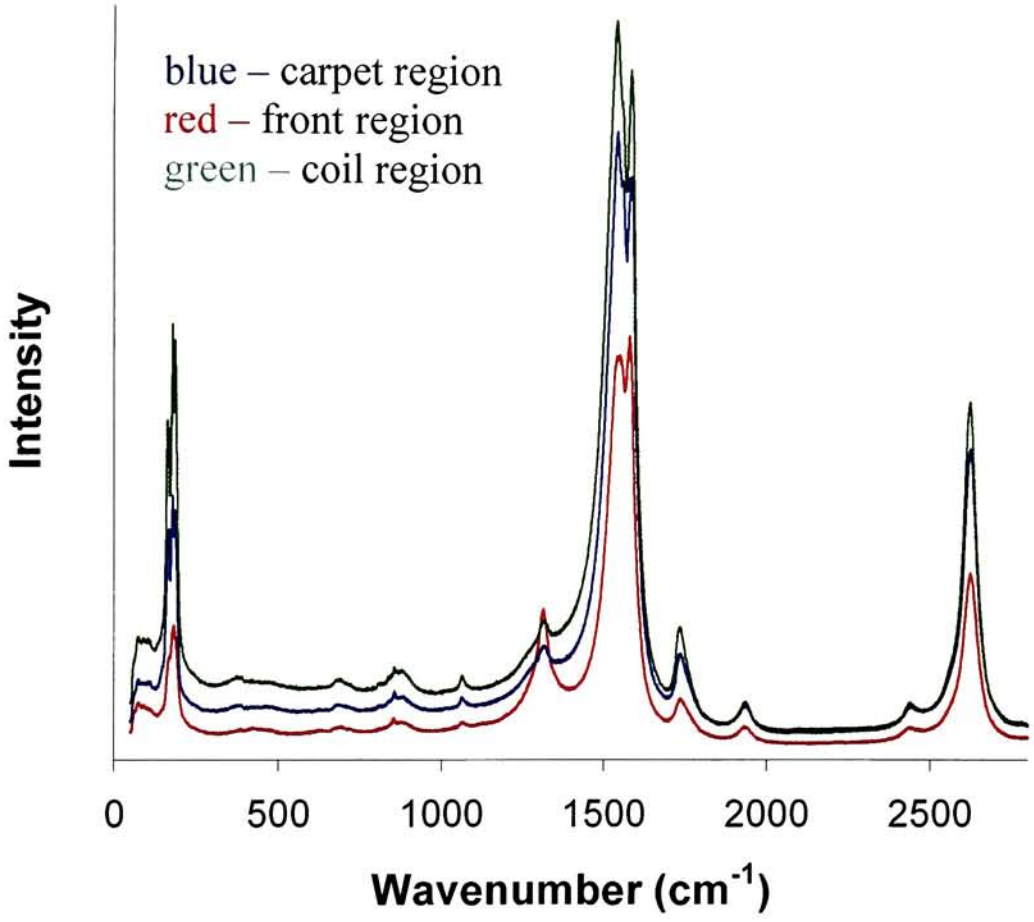

Figure 54: Overlay of Raman spectra taken of SWNT materials collected from different chamber regions. Excitation wavelength = 633 nm.

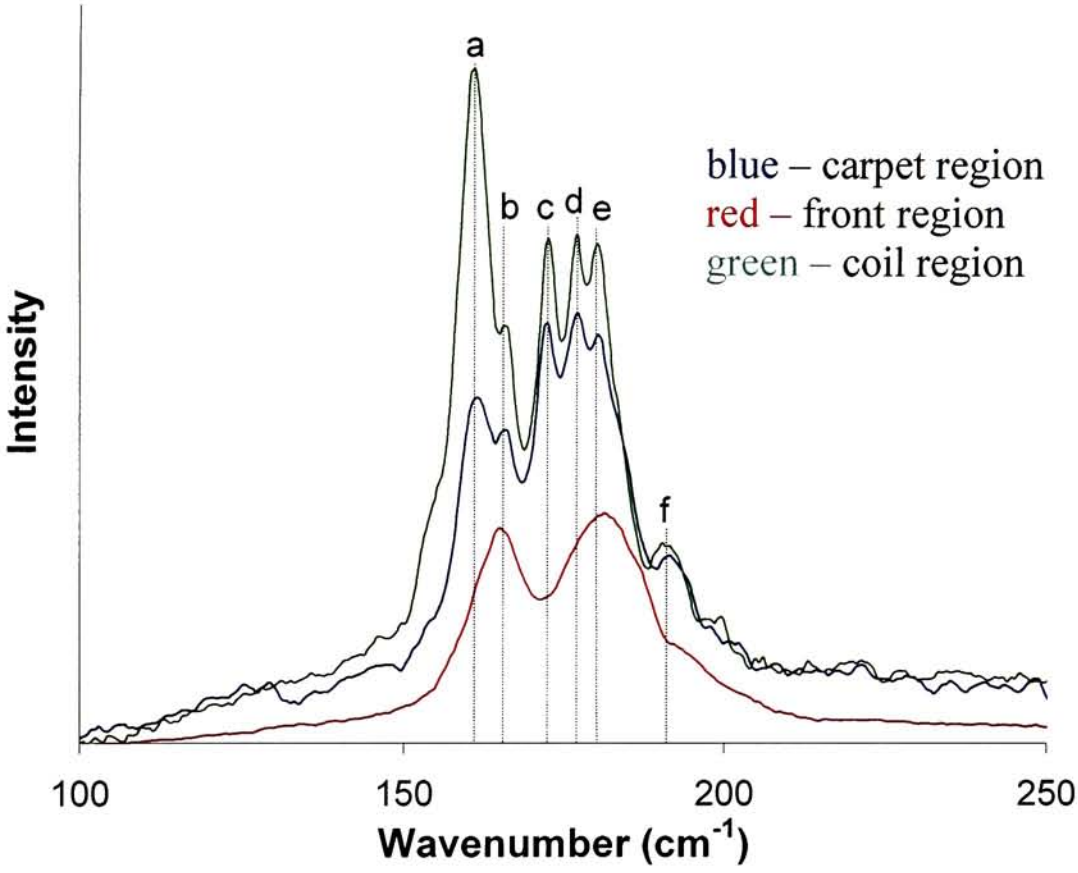

Figure 55: Raman RBM of as-produced SWNTs from the same synthesis, taken from different collection regions. Excitation wavelength = 488 nm.

Peak	Wavenumber (cm^{-1})	Corresponding diameter[59] (nm)
a	161.2	1.39
b	165.0	1.36
c	172.6	1.30
d	177.0	1.26
e	180.2	1.24
f	191.0	1.17

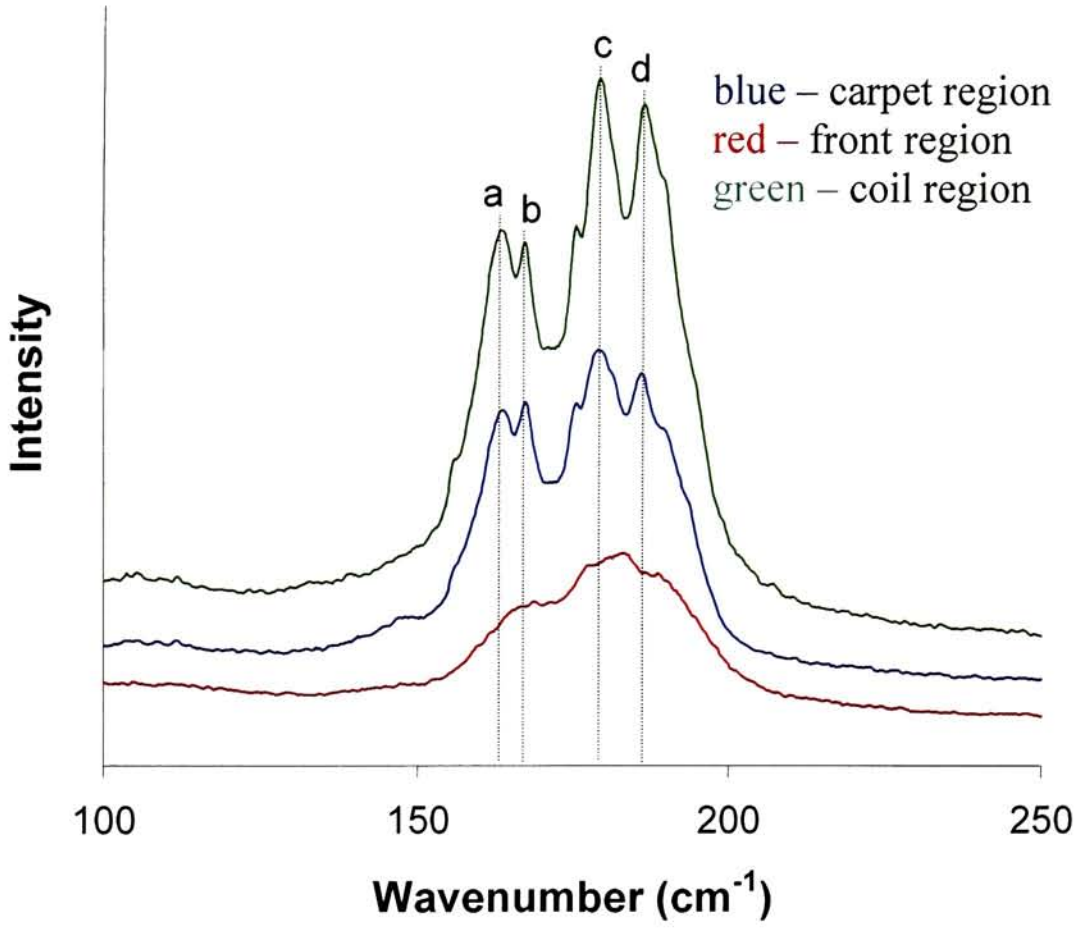

Figure 56: Raman RBM of as-produced SWNTs from the same synthesis, taken from different collection regions. Excitation wavelength = 633 nm.

Peak	Wavenumber (cm^{-1})	Corresponding diameter[59] (nm)
a	164.0	1.36
b	167.3	1.34
c	179.6	1.25
d	186.6	1.20

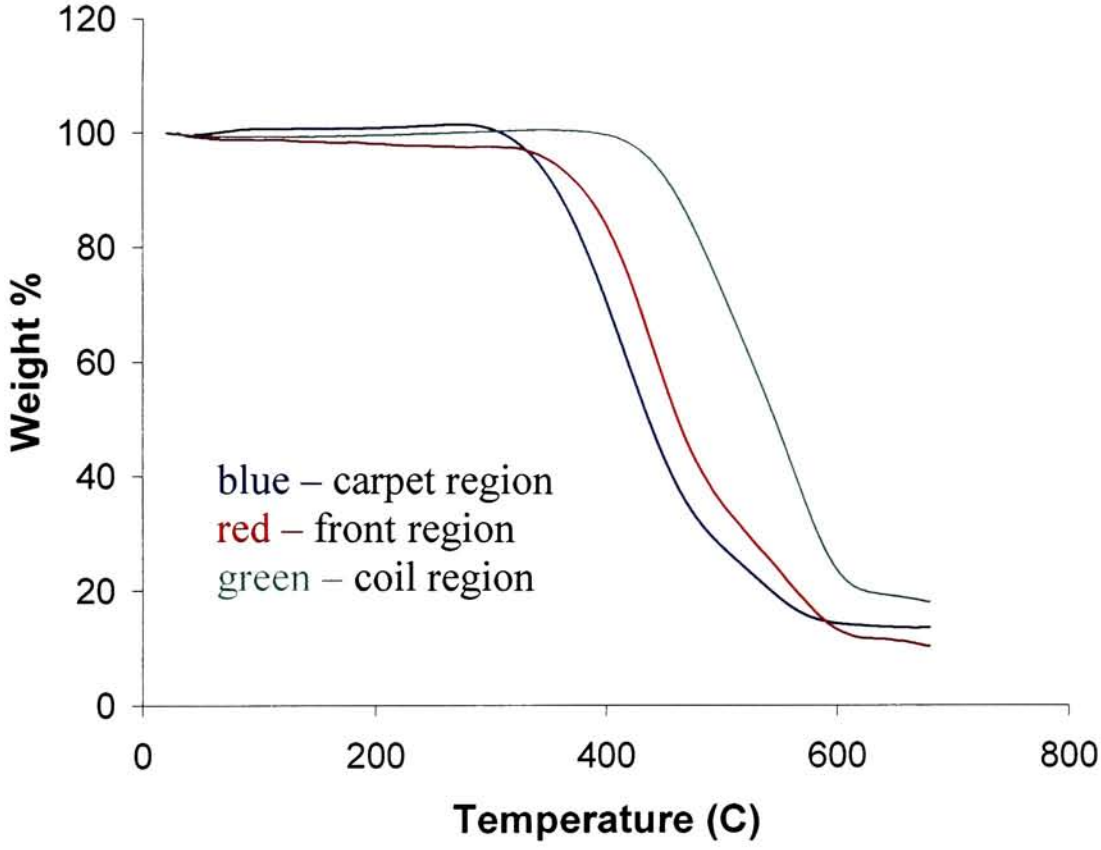

Figure 57: TGA overlay for products collected from different regions of the reaction chamber from the same synthesis.

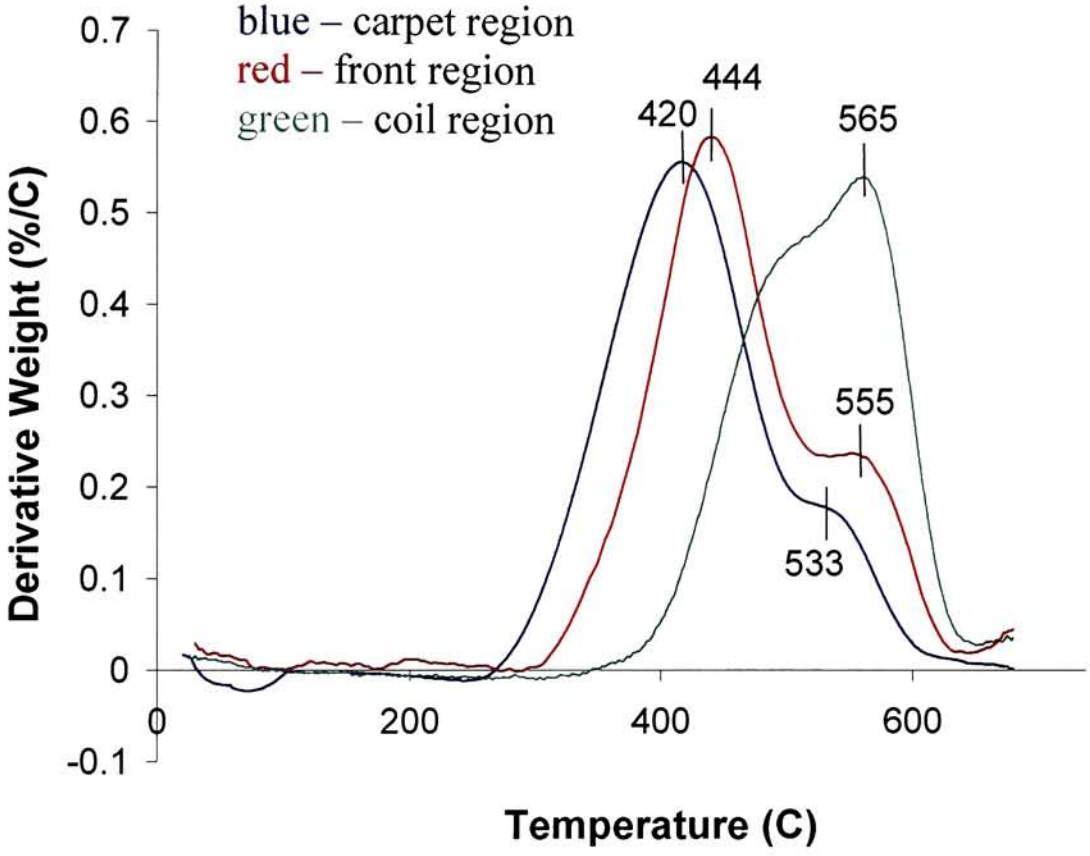

Figure 58: First derivative TGA overlay for products collected from different regions of the reactor chamber from the same synthesis.

collected from the coil region show the latest onset of thermal decomposition. The first derivative curves show that the material collected from the front region displays a second transition peak larger than that of the carpet. The coil material, however, displays a first derivative peak shifted to a much higher temperature. As a result the coil material likely contains the largest proportion of SWNTs to impurities of all the collection regions. Similarly, the coil region material also demonstrates the greatest metal content for the various collection regions. Although there is significantly enhanced yield of SWNTs in the coil region, there is greater metal impurity content and a much slower production rate compared with the carpet material.

The UV-Vis-NIR spectra are similar for the three collection regions (Figure 59). The peak corresponding to the first Van Hove singularity is located at 1779 nm, which correlates to an SWNT diameter of 1.43 nm. The second and third Van Hove peaks are located at 940 nm and 646 nm respectively for all three samples. Both the UV-Vis-NIR spectra and Raman spectra indicate an absence of shift in diameter distribution for the different collection regions. SEM images for the samples taken from different collection regions are displayed in Figure 60. SWNT bundles are present in each of these samples.

3.6 Variation in Power Density

Effects of the incident laser beam power density on SWNT diameters and yield were investigated. Three syntheses were performed with power densities of 100, 200, and 300 W/cm^2 using a corner to corner raster pattern. Raman spectra from these three syntheses (Figures 61-64) show a significant shift in the diameter distributions between the samples. The RBM portion of the spectra at 488 nm excitation show predominant peaks at 161.2, 177.7, and 180.8 wavenumbers, which correspond to SWNT diameters of

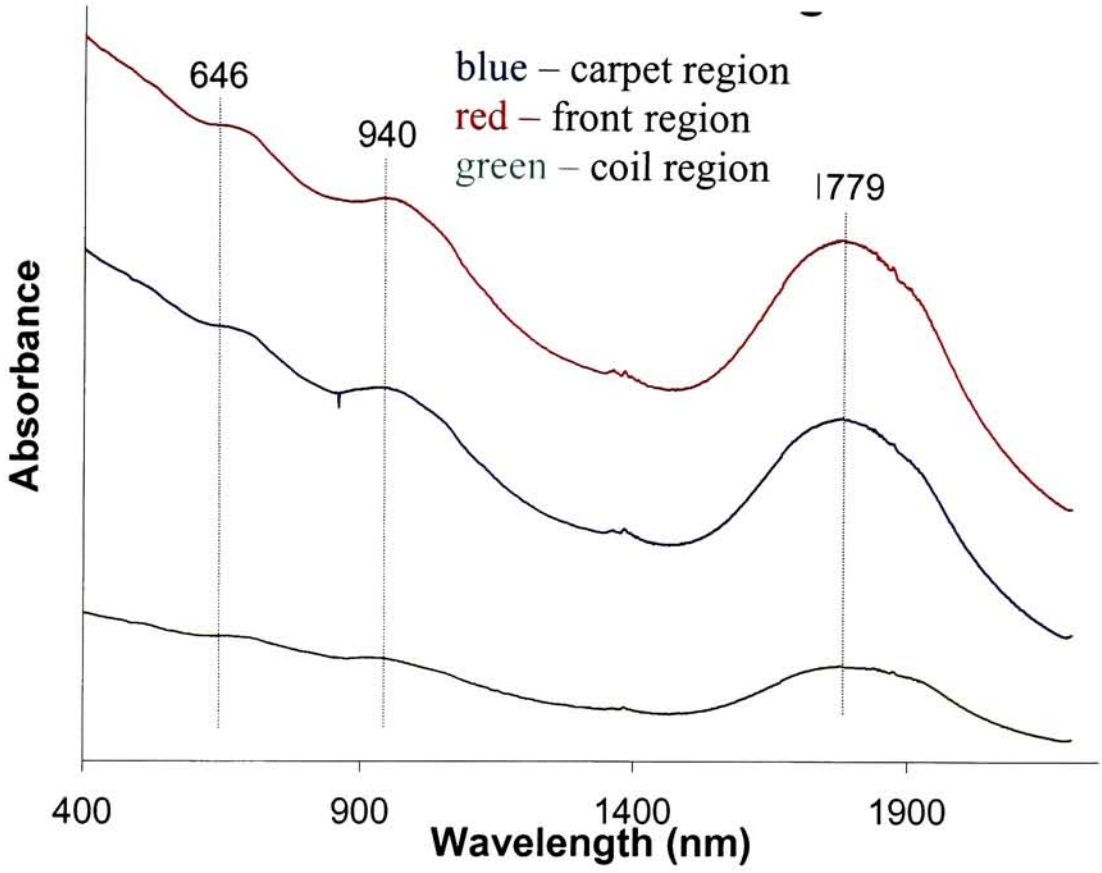

Figure 59: UV-Vis-NIR spectra taken from as-produced SWNTs from various collection regions from the same synthesis.

Region	First Van Hove Peak (nm)	Corresponding diameter[16] (nm)
Front, Coil, Carpet	1779	1.43

a

b

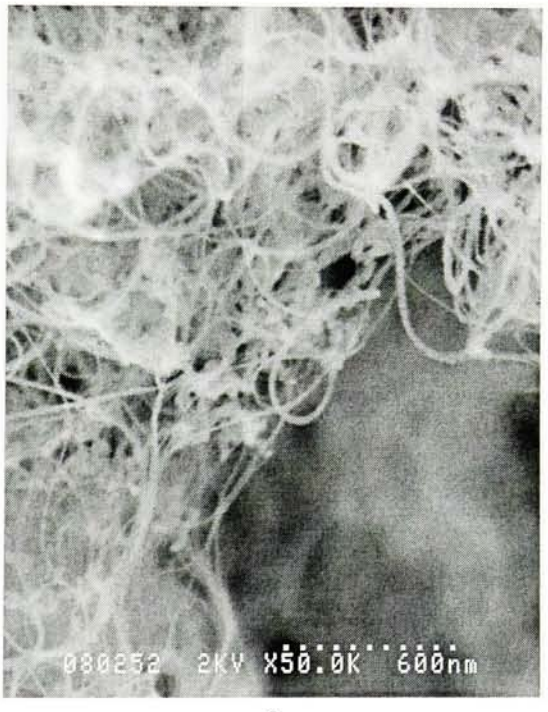

c

Figure 60: SEM micrographs of material produced and collected from different regions of the reactor chamber. a) Carpet region b) Front region c) Coil region.

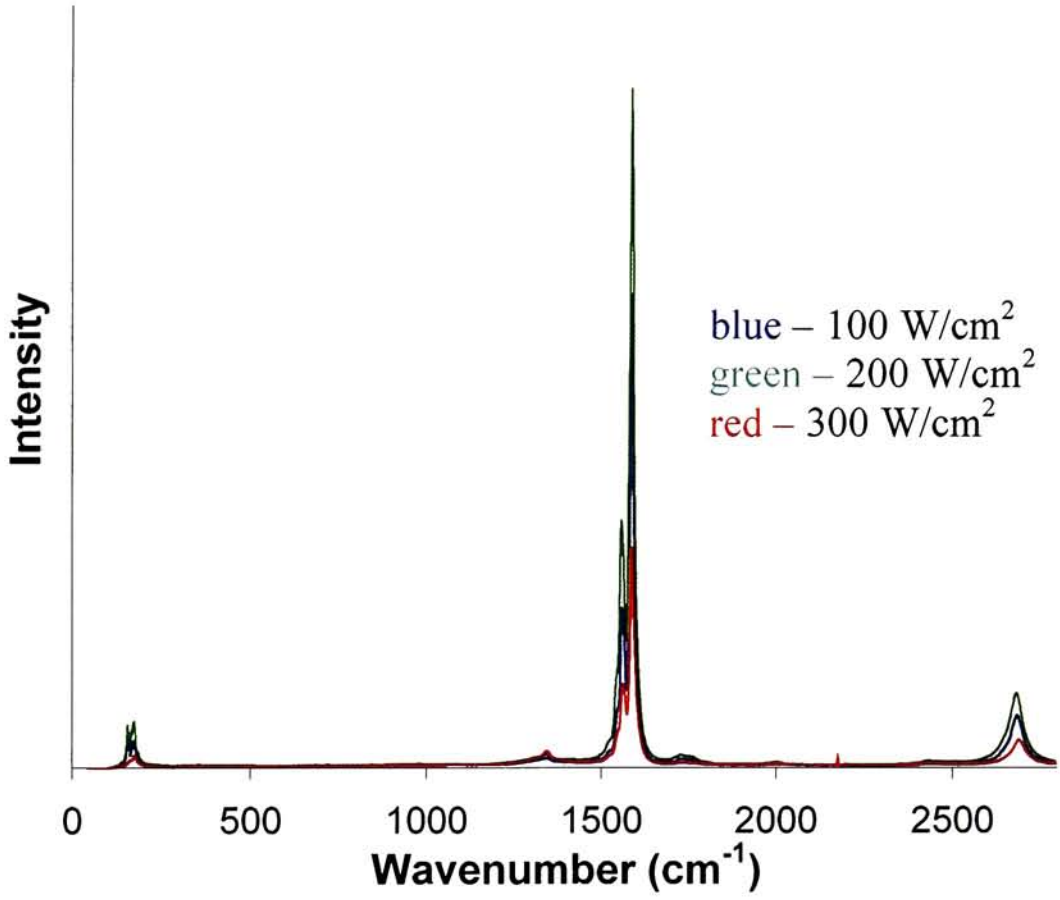

Figure 61: Overlay of Raman spectra taken of SWNT materials synthesized with various power densities. Excitation wavelength = 488 nm.

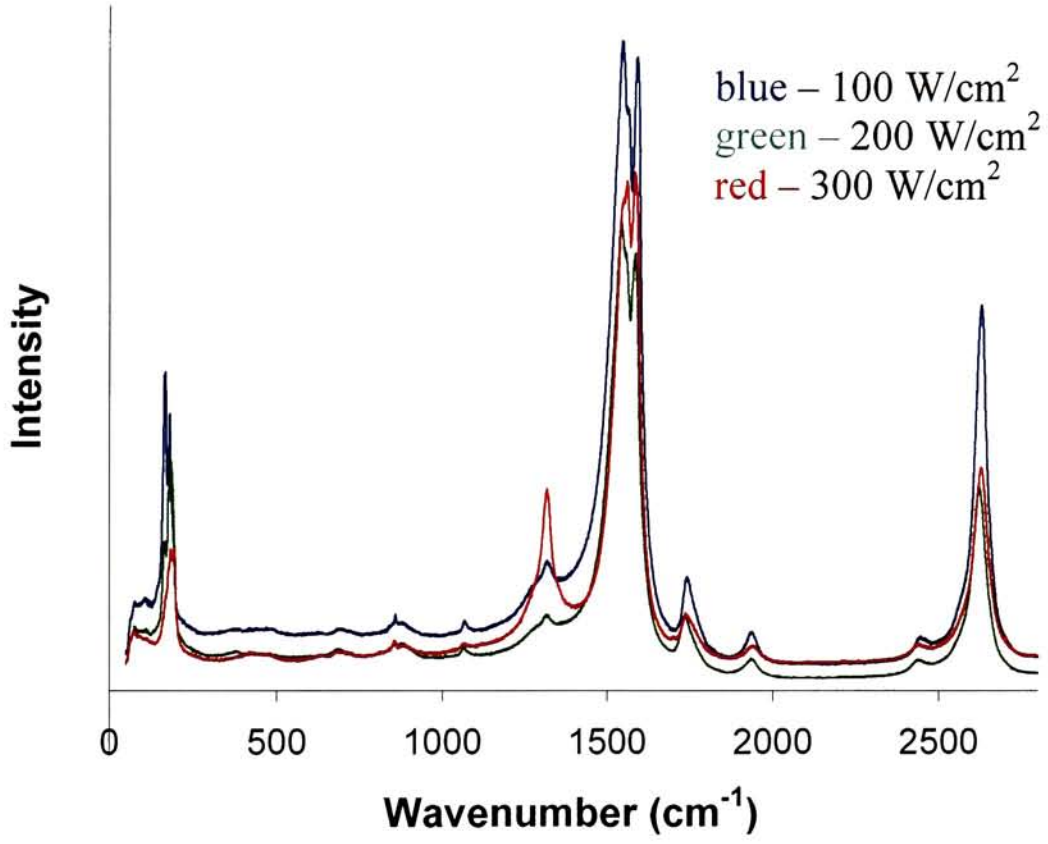

Figure 62: Overlay of Raman spectra taken of SWNT materials synthesized with various power densities. Excitation wavelength = 633 nm.

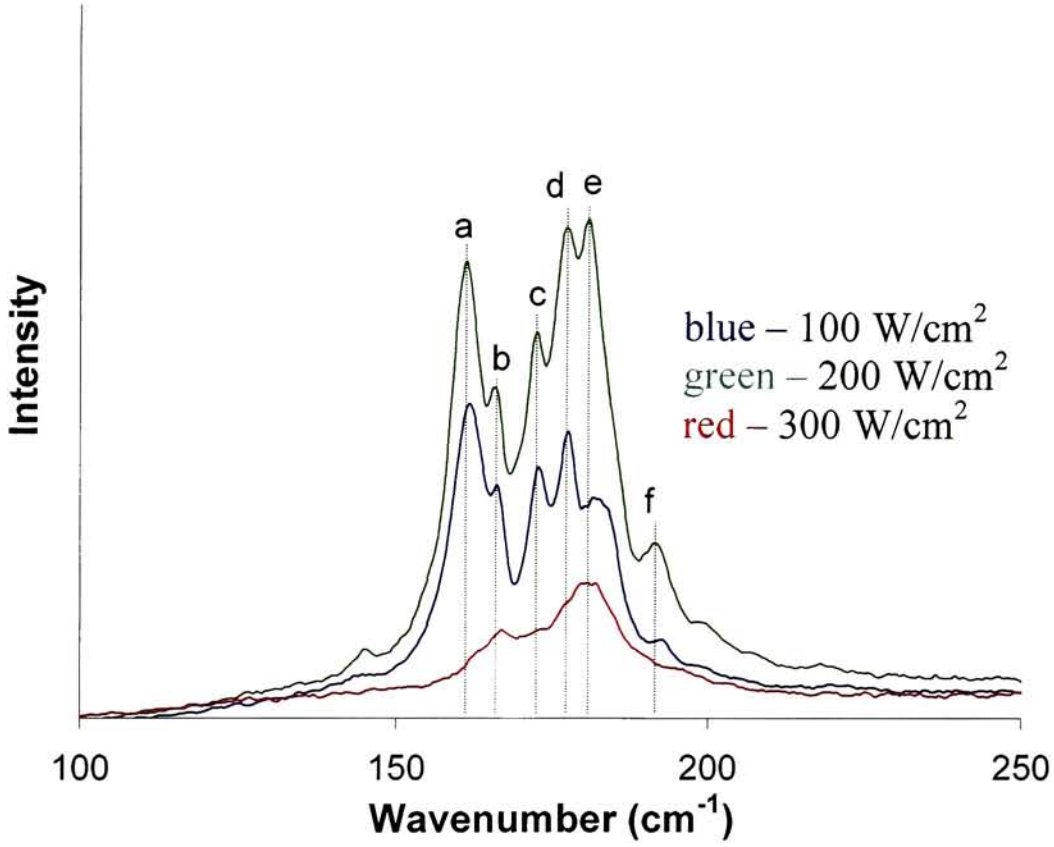

Figure 63: Raman overlay of RBM given by materials synthesized at various power densities. Excitation wavelength = 488 nm.

Peak	Wavenumber (cm^{-1})	Corresponding diameter[59] (nm)
a	161.2	1.39
b	166.2	1.35
c	172.6	1.30
d	177.7	1.26
e	180.8	1.24
f	192.2	1.16

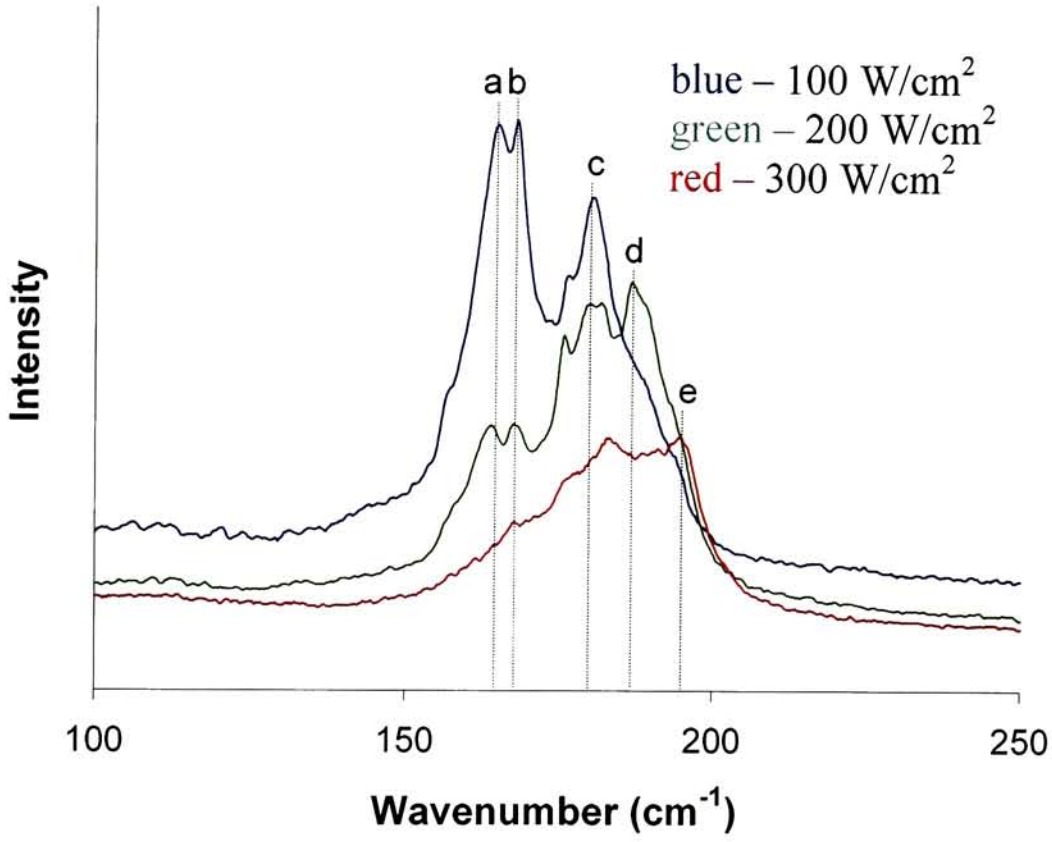

Figure 64: Raman overlay of the RBM from materials synthesized at various power densities. Excitation wavelength = 633 nm.

Peak	Wavenumber (cm^{-1})	Corresponding diameter[59](nm)
a	165.3	1.35
b	168.0	1.33
c	180.6	1.24
d	187.3	1.19
e	195.0	1.15

1.39, 1.26, and 1.24 nm respectively for both 100 and 200 W/cm^2. The spectrum of the 300 W/cm^2 material shows a peak corresponding to a diameter of 1.24 nm as its predominant peak. The Raman spectra acquired at 633 nm excitation display a more pronounced trend it the RBM. The SWNT material synthesized at 100 W/cm^2 has its predominant peaks corresponding to 1.33 and 1.35 nm. The 200 W/cm^2 material contains small amounts of 1.33 and 1.35 nm SWNTs, but has a more intense peak corresponding to 1.19 nm. The 300 W/cm^2 has its most intense peak shifted to 1.15 nm. The Raman results therefore indicate that higher power densities give smaller diameter SWNTs. The D/G ratios for these materials are displayed in Table 9.

Table 9: D/G ratios for materials synthesized using various power densities

Power (W/cm^2)	488 nm Excitation			633 nm Excitation		
	D	**G**	**D/G**	**D**	**G**	**D/G**
100	235.7	15759.4	0.01496	2030.	10067	0.2016
200	322.7	11062.3	0.02917	1197	7504.7	0.1595
300	409.7	5124	0.07996	3137	7961.4	0.3940

The TGA thermograms (Figures 65 and 66) indicate similar thermal decomposition patterns for materials synthesized using various power densities. The first derivative overlay, however, indicates an increasing area in the shoulder peak at 542°C with decreasing power density. SWNTs, therefore, likely become more coated in the final product at lower power densities. The UV-Vis-NIR spectra (Figure 67) indicate the least amount of peak definition for the 300 W/cm^2 spectrum. It is likely that this reduction in definition is due to reduction in SWNT yield. The first Van Hove peaks in the UV-Vis-NIR spectra do not demonstrate large shifts from one another. SEM images are displayed in Figure 68. SWNT bundles are present in all samples.

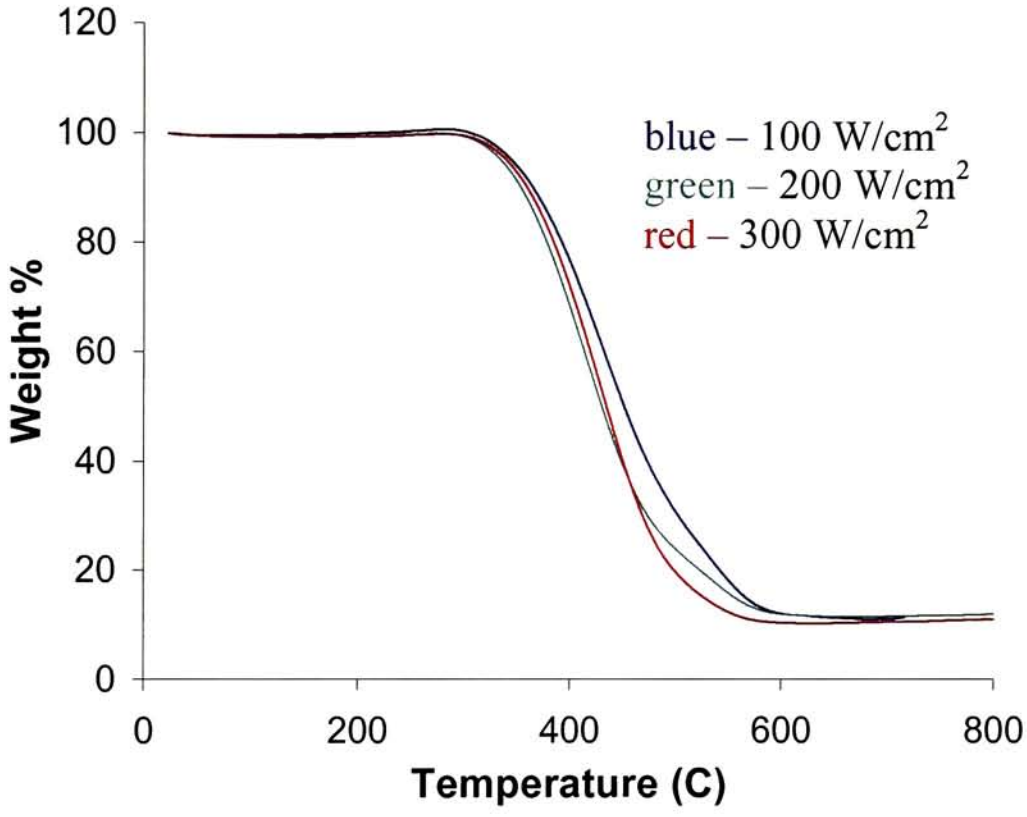

Figure 65: TGA overlay for material synthesized at various power densities.

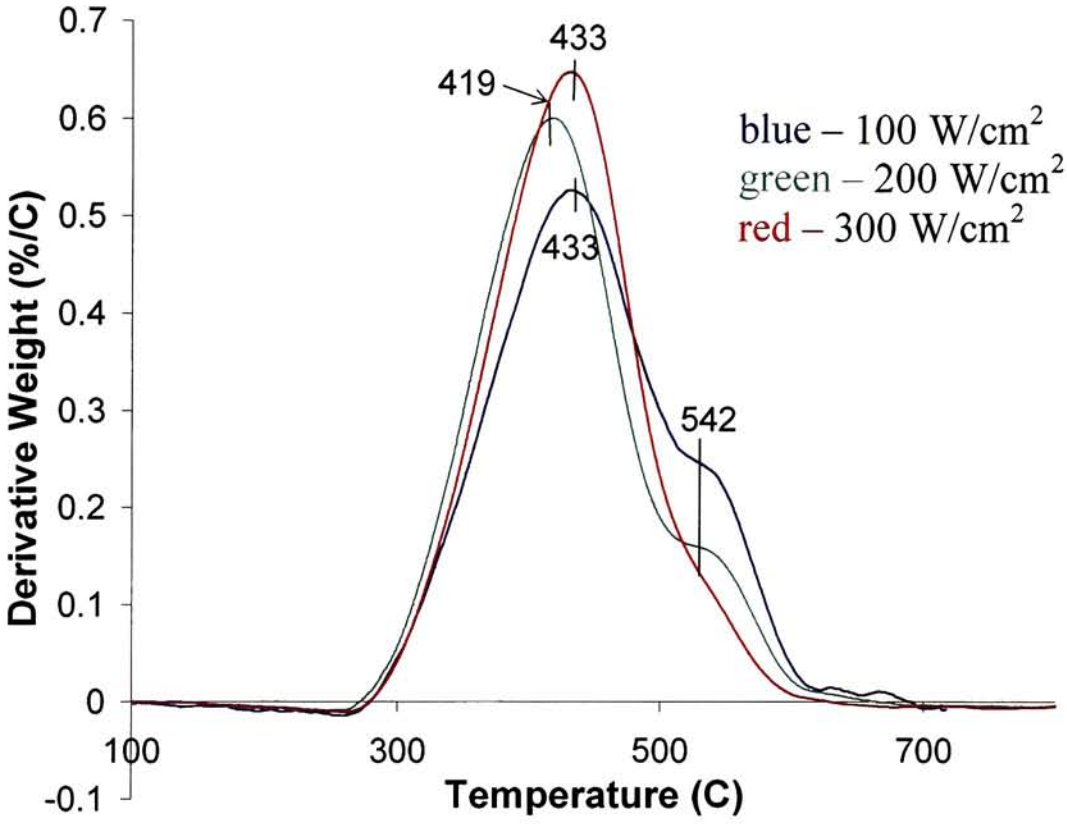

Figure 66: First derivative TGA overlay for materials synthesized at various power densities.

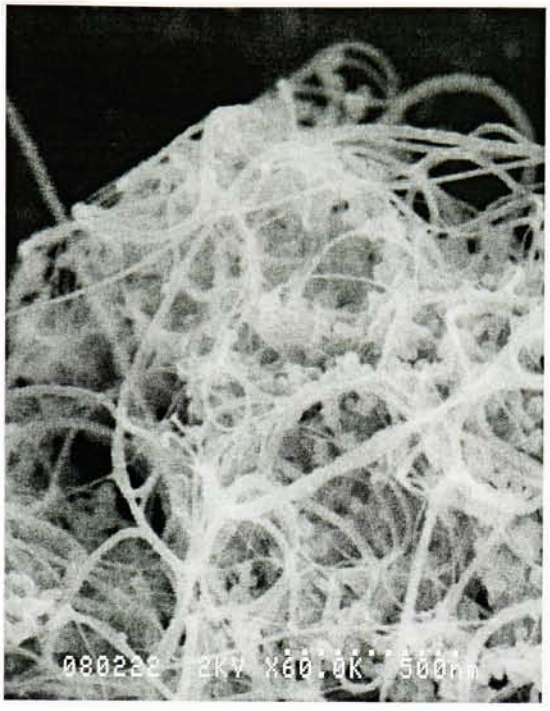

a

b

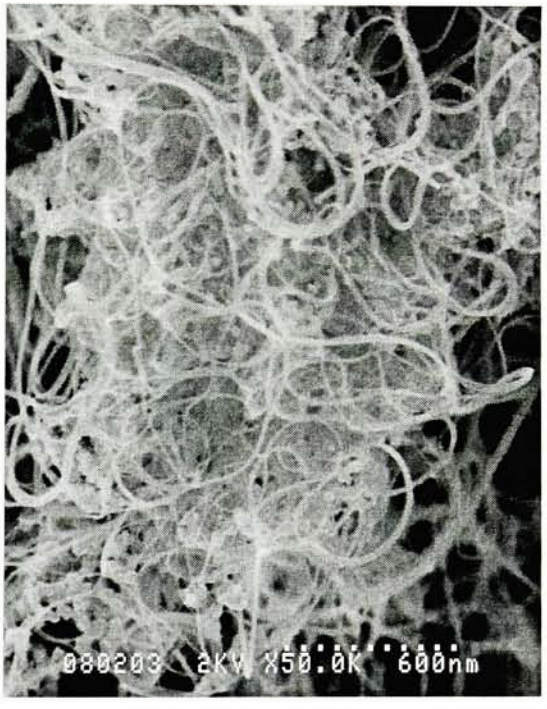

c

Figure 67: Representative SEM micrographs of material synthesized at various power densities. a) 100 W/cm^2 b) 200 W/cm^2 c) 300 W/cm^2

4.0 Conclusion

Results from the syntheses of SWNTs show that by varying experimental conditions, it is possible to dramatically influence the properties of the final products. By systematically varying five experimental parameters, further insight was gained into how control of SWNT properties can be achieved for laser vaporization synthesis. The most profound set of results obtained in these studies involved using the corner to corner raster pattern. Using a one shot corner to corner raster pattern, several important differences are observed in comparison with a linear raster pattern. A drastic reduction of segregation of the metal at the surface of the doped graphite target is accomplished by using a corner to corner raster pattern. This reduces the amount of metal impurities in the final sample as well as increasing production rates. The lack of metal enrichment at the target surface is the result of a reduction of the localized heating typically caused by repeatedly striking the same area on the target with laser pulses. This localized heating in the target causes a combination of melting, migration, and agglomeration of the catalyst to the target surface. In addition a smaller diameter distribution was present in the SWNT with the one shot corner to corner raster pattern as compared to a linear raster. This result is further evidence of the reduced temperature at the target surface.

An increase in production rate was also reported by Yudasaka when using two separate targets, (one carbon, one metal catalyst) for SWNT synthesis.[78] However the relative purity of the materials was not discussed, so a true comparison of nanotube production rates cannot be determined. However from the Raman analysis, it appears our materials have less defects and less nanostructured graphite. Eklund et. al. reported a series of interesting results utilizing a rotating target with ultrafast laser pulses.[69] A

significant increase in production rate was observed, as well as preservation of target surface uniformity. While the results from this work mirror the results from our rapid raster experiments, the system is extremely expensive and will not be available to most nanotube synthetic chemists.

Control over SWNT product was also achieved through variation in reactor chamber temperature. Similar results were obtained to those in the literature by varying reactor chamber temperature. The most obvious influence of temperature is the reduction of SWNT diameters with a decrease in reactor chamber temperature. This reduction in diameter is consistent throughout the temperature range of 900-1200°C. A decrease in chamber temperature also results in a decrease in SWNT yield within the as-produced soot. The amount of disordered carbon increases with decreasing reactor chamber temperature as well. Variation in graphite particle size led to changes in SWNT yields and a varied diameter distribution. Smaller graphite particles sizes led to increased SWNT yields in the as-produced material. Although the corresponding SWNT diameters present within the distribution remained the same when graphite particle size was varied, the ratio of those diameters changed. Smaller graphite particles sizes yielded smaller diameters within the diameter distribution.

Alterations made in the reactor chamber influenced the final SWNT products. A variation in reactor chamber volume influenced SWNT diameter distribution as well as yields. By using the smaller 1.6 L chamber in the synthesis the diameters of SWNTs present were increased compared to the 2.4 L chamber. The corresponding SWNT diameters present were similar for both chamber volumes, however, the ratios of these diameters were altered. The 2.4 L chamber was found to give better SWNT yields within

the as-produced soot. The 1.6 L chamber, however, gave material with a lower amount of disordered carbon. Chamber configuration was also investigated by using an inner quartz flow tube. This flow tube allowed for material to be collected from three different regions in the reactor chamber. Material generated in the coil region showed a significantly enhanced yield of SWNTs within the as-produced soot. The coil region, however, also showed an increase in metal catalyst content and a greater amount of disordered carbon. Material collected from the front region also contained a greater SWNT yield as compared with the traditional carpet material. Investigation in to variation in laser beam power density gave results that an increase in power density gives SWNTs with smaller diameters. Similarly an increase in power density gives an increase in production rate.

In summary, five experimental variables were investigated to evaluate the influence on the final SWNT product. These experiments provided valuable insight as to the extent of control available in laser vaporization synthesis. Through alterations in experimental variables, SWNT products can be synthesized with particular desired specifications.

5.0 References

(1) Iijima, S.; Ichihashi, T. *Nature* **1993**, *363*, 603.

(2) Bethune, D. S.; Kiang, C. H.; S., D. M.; Gorman, G.; Savoy, R.; Vazquez, J.; Beyers, R. *Nature* **1993**, *363*, 605.

(3) Odom, T. W.; Huang, J.; Kim, P.; Lieber, C. M. *J. Phys. Chem. B* **2000**, *104*, 2794.

(4) Ajayan, P. M. *Chem. Rev.* **1999**, *99*, 1787.

(5) de Heer, W. A. *Curr. Opinion Solid State Mater. Sci.* **1999**, *4*, 355.

(6) Dai, H. *Surf. Sci.* **2002**, *500*, 218.

(7) Dai, H. *Accts. Chem. Res.* **2002**, *35*, 1035.

(8) Odom, T. W.; Huang, J.; Kim, P.; Lieber, C. M. *Nature* **1998**, *391*, 62.

(9) Salvetat-Delmotte, J.; Rubio, A. *Carbon* **2002**, *40*, 1729.

(10) Guo, T.; Nikolaev, P.; Thess, A.; Colbert, D. T.; Smalley, R. E. *Chem. Phys. Lett.* **1995**, *243*, 49.

(11) Dai, H.; Rinzler, A. G.; Nikolaev, P.; Thess, A.; Colbert, D. T.; Smalley, R. E. *Chem. Phys. Lett.* **1996**, *260*, 471.

(12) Nikolaev, P.; Bronikowski, M. J.; Bradley, R. K.; Rohmund, F.; Colbert, D. T.; Smith, K. A.; Smalley, R. E. *Chem. Phys. Lett.* **1999**, *313*, 91.

(13) Harutyunyan, A. R.; Bhabendra, P. K.; Chang, J.; Chen, G.; Eklund, P. C. *J. Phys. Chem. B* **2002**, *106*, 8671.

(14) Huang, S.; Dai, L. *J. Phys. Chem. B* **2002**, *106*, 3543.

(15) Huang, H.; Kajiura, H.; Yamada, A.; Ata, M. *Chem. Phys. Lett.* **2002**, *356*, 567.

(16) Chiang, I. W.; Brinson, B. E.; Smalley, R. E.; Margrave, J. L.; Hauge, R. H. *J. Phys. Chem. B* **2001**, *105*, 1157.

(17) Chiang, I. W.; Brinson, B. E.; Huang, A. Y.; Willis, P. A.; Bronikowski, M. J.; Margrave, J. L.; Smalley, R. E.; Hauge, R. H. *J. Phys. Chem. B* **2001**, *105*, 8297.

(18) Dillon, A. C.; Gennett, T.; Jones, K. M.; Alleman, J. L.; Parilla, P. A.; Heben, M. J. *Adv. Mater.* **1999**, *11*, 1354.

(19) Rinzler, A. G.; Liu, J.; Dai, H.; Nikolaev, P.; Huffman, C. B.; Rodriguez-Macias, F. J.; Boul, P. J.; Lu, A. H.; Heymann, D.; Colbert, D. T.; Lee, R. S.; Fischer, J. E.; Rao, A. M.; Eklund, P. C.; Smalley, R. E. *Appl. Phys. A.* **1998**, *67*, 29.

(20) Lambin, P.; Loiseau, A.; Culot, C.; Biro, L. P. *Carbon* **2002**, *40*, 1635.

(21) Rosenblatt, S.; Yaish, Y.; Park, J.; Gore, J.; Sazonova, V.; McEuen, P. L. *Nano Lett.* **2002**, *2*, 869.

(22) Lefebvre, J.; Antonov, R. D.; Radosavljevic, M.; Lynch, J. F.; Llaguno, M.; Johnson, A. T. *Carbon* **2000**, *38*, 1745.

(23) Avouris, P. *Chem. Phys.* **2002**, *281*, 429.

(24) Tsukagoshi, K.; Yoneya, N.; S., U.; Aoyagi, Y.; Kanda, A.; Ootuka, Y.; Alphenaar, B. W. *Physica B* **2002**, *323*, 107.

(25) Kroto, H. W.; Heath, J. R.; S., O. B.; Curl, R. F.; Smalley, R. E. *Nature* **1985**, *318*, 162.

(26) Smalley, R. E., 2003; Vol. 2003.

(27) Dresselhaus, M. S.; Dresselhaus, G.; Eklund, P. C. *Science of Fullerenes and Carbon Nanotubes*; Academic Press: San Diego, 1996.

(28) Ugarte, D. *Nature* **1992**, *359*, 707.
(29) Iijima, S. *Nature* **1991**, *354*, 56.
(30) Zeng, X.; Sun, X.; Cheng, G.; Yan, X.; Xu, X. *Physica B* **2002**, *323*, 330.
(31) Dresselhaus, M. S.; Dresselhaus, G.; Saito, R. *Phys. Rev. B* **1992**, *45*, 6234.
(32) Saito, R.; Fujita, M.; Dresselhaus, G.; Dresselhaus, M. S. *Phys. Rev. B* **1992**, *46*, 1804.
(33) Hamada, N.; Sawada, S.; Oshiyama, A. *Phys. Rev. Lett.* **1992**, *68*, 1579.
(34) Mintmire, J. W.; Dunlap, B. I.; White, C. T. *Phys. Rev. Lett.* **1992**, *68*, 631.
(35) Euler, L. *Novi comm. acad. scientiarum imperialis petropolitanae* **1752**, *4*, 109.
(36) Lebedkin, S.; Schweiss, P.; Renker, B.; Malik, S.; Hennrich, F.; Neumaier, M.; Stoermer, C.; Kappes, M. M. *Carbon* **2002**, *40*, 417.
(37) Wang, N.; Tang, Z. K.; Li, G. D.; Chen, J. S. *Nature* **2000**, *408*, 50.
(38) Gennett, T.; Dillon, A. C.; Alleman, J. L.; Jones, K. M.; Hasson, F. S.; Heben, M. J. *Chem. Mater.* **2000**, *12*, 599.
(39) Li, F.; Cheng, H. M.; Bai, S.; Su, G.; Dresselhaus, M. S. *Appl. Phys. Lett.* **2000**, *77*, 3161.
(40) Journet, C.; Maser, W. K.; Bernier, P.; Loiseau, A.; Lamy de la Chapelle, M.; Lefrant, S.; Deniard, P.; Lee, R.; Fischer, J. E. *Nature* **1997**, *388*, 756.
(41) Thess, A.; Lee, R.; Nikolaev, P.; Dai, H.; Petit, P.; Robert, J.; Xu, C.; Lee, Y. H.; Kim, S. G.; Rinzler, A. G.; Colbert, D. T.; Scuseria, G. E.; Tomanek, D.; Fischer, J. E.; Smalley, R. E. *Science* **1996**, *273*, 483.
(42) Gavillet, J.; Loiseau, A.; Ducastelle, F.; Thair, S.; Bernier, P.; O., S.; Thibault, J.; Charlier, J.-C. *Carbon* **2002**, *40*, 1649.
(43) Metenier, K.; Bonnamy, S.; Beguin, F.; Journet, C.; Bernier, P.; Lamy de la Chapelle, M.; Chauvet, O.; Lefrant, S. *Carbon* **2002**, *40*, 1756.
(44) Saito, Y.; Nishikubo, K.; Kawabata, K.; Matsumoto, T. *J. Appl. Phys.* **1996**, *80*, 3062.
(45) Kiang, C. H. *J. Phys. Chem. A* **2000**, *104*, 2454.
(46) Qin, L.-C.; Zhao, X.; Hirahara, K.; Miyamoto, Y.; Ando, Y.; Iijima, S. *Nature* **2000**, *408*, 50.
(47) Duesberg, G. S.; Blau, W.; Byrne, H. J.; Muster, J.; Burghard, M.; Roth, S. *Syn. Met.* **1999**, *103*, 2484.
(48) Cassell, A. M.; Raymakers, J. A.; Kong, J.; Dai, H. *J. Phys. Chem. B* **1999**, *103*, 6484.
(49) Grujicic, M.; Cao, G.; Gersten, B. *Appl. Surface Sci.* **2002**, *191*, 223.
(50) Zheng, B.; Lu, C.; Gu, G.; Makarovski, A.; Finkelstein, G.; Liu, J. *Nano Lett.* **2002**, *2*, 895.
(51) Harutyunyan, A. R.; Pradhan, B. K.; Kim, U. J.; Chen, G.; Eklund, P. C. *Nano Lett.* **2002**, *2*, 525.
(52) Chen, B.; Parker, G. I.; Han, J.; Meyyappan, M.; Cassell, A. M. *Chem. Mater.* **2002**, *14*, 1891.
(53) Hornyak, G. L.; Grigorian, L.; Dillon, A. C.; Parilla, P. A.; Jones, K. M.; Heben, M. J. *J. Phys. Chem. B* **2002**.

(54) Cheung, C. L.; Kurtz, A.; Park, H.; Lieber, C. M. *J. Phys. Chem. B* **2002**.

(55) Coquay, P.; De Grave, E.; Peigney, A.; Vandenberghe, R. E.; Laurent, C. *J. Phys. Chem. B* **2002**, *106*, 13186.

(56) Coquay, P.; Peigney, A.; De Grave, E.; Vandenberghe, R. E.; Laurent, C. *J. Phys. Chem. B* **2002**, *106*, 13199.

(57) Liu, B. C.; Tang, S. H.; Yu, Z. L.; Zhang, B. L.; Chen, T.; Zhang, S. Y. *Chem. Phys. Lett.* **2002**, *357*, 297.

(58) Kukovitsky, E. F.; G., L. v. S.; Sainov, N. A.; Shustov, V. A.; Chernozatonskii, L. A. *Chem. Phys. Lett.* **2002**, *355*, 497.

(59) Su, M.; Li, Y.; Maynor, B.; Buldum, A.; Lu, J. P.; Liu, J. *J. Phys. Chem. B* **2000**, *104*, 6505.

(60) Bandow, S.; Asaka, S.; Saito, Y.; Rao, A. M.; Grigorian, L.; Richter, E.; Eklund, P. C. *Phys. Rev. Lett.* **1998**, *80*, 3779.

(61) Yudasaka, M.; Kokai, F.; Takahashi, K.; Yamada, R.; Sensui, N.; Ichihashi, T.; Iijima, S. *J. Phys. Chem. B* **1999**, *103*, 3576.

(62) Braidy, N.; El Khakani, M. A.; Botton, G. A. *Carbon* **2002**, *40*, 2835.

(63) Maser, W. K.; Munoz, E.; Martinez, M. T.; Benito, A. M.; de la Fuente, G. F. *Optical Mater.* **2001**, *17*, 331.

(64) Yudasaka, M.; Ichihashi, T.; Komatsu, T.; Iijima, S. *Chem. Phys. Lett.* **1999**, *299*, 91.

(65) Kichambare, P. D.; Chen, L. C.; Wang, C. T.; Ma, K. J.; Wu, C. T.; Chen, K. H. *Mater. Chem. Phys.* **2001**, *72*, 218.

(66) Kokai, F.; Takahashi, K.; Yudasaka, M.; Yamada, R.; Ichihashi, T.; Iijima, S. *J. Phys. Chem. B* **1999**, *103*, 4346.

(67) Gennett, T.; Dillon, A. C.; Alleman, J. L.; Jones, K. M.; Parilla, P. A.; Heben, M. J. In *Mater. Res. Soc. Symp. Proc.*, 2001; Vol. 633, p paper A2.3.

(68) Braidy, N.; El Khakani, M. A.; Botton, G. A. *Chem. Phys. Lett.* **2002**, *354*, 88.

(69) Eklund, P. C.; Pradhan, B. K.; Kim, U. J.; Xiong, Q.; Fischer, J. E.; Friedman, A. D.; Holloway, B. C.; Jordan, K.; Smith, M. W. *Nano Lett.* **2002**, *2*, 561.

(70) Zhang, Y.; Gu, H.; Iijima, S. *Appl. Phys. Lett.* **1998**, *73*, 3827.

(71) Munoz, E.; Maser, W. K.; Benito, A. M.; de la Fuente, G. F.; Martinez, M. T. *Syn. Met.* **1999**, *103*, 2490.

(72) Jost, O.; Gorbunov, A. A.; Moller, J.; Pompe, W.; Liu, X.; Georgi, P.; Dunsch, L.; Golden, M. S.; Fink, J. *J. Phys. Chem. B* **2002**, *106*, 2875.

(73) Gorbunov, A. A.; Friedlein, R.; Jost, O.; Golden, M. S.; Fink, J.; Pompe, W. *Appl. Phys. A.* **1999**, *69*, S593.

(74) Yudasaka, M.; Yamada, R.; Sensui, N.; Wilkins, T.; Ichihashi, T.; Iijima, S. *J. Phys. Chem. B* **1999**, *103*, 6224.

(75) Munoz, E.; Maser, W. K.; Benito, A. M.; Martinez, M. T.; de la Fuente, G. F.; Righi, A.; Anglaret, E.; Sauvajol, J. L. *Syn. Met.* **2001**, *121*, 1193.

(76) Kataura, H.; Kumazawa, Y.; Maniwa, Y.; Ohtsuka, Y.; Sen, R.; Suzuki, S.; Achiba, Y. *Carbon* **2000**, *38*, 1691.

(77) Scott, C. D.; Arepalli, S.; Nikolaev, P.; Smalley, R. E. *Appl. Phys. A.* **2001**, *72*, 573.

(78) Yudasaka, M.; Komatsu, T.; Ichihashi, T.; Iijima, S. *Chem. Phys. Lett.* **1997**, *278*, 102.

(79) Laplaze, D.; Alvarez, L.; Guillard, T.; Badie, J. M.; Flamant, G. *Carbon* **2002**, *40*, 1621.

(80) Yasuda, A.; Mizutani, W.; Shimizu, T.; Tokumoto, H. *Physica B* **2002**, *323*, 269.

(81) Sun, X.; C., L.; Wong, N.; Lee, C.; Lee, S.; Teo, B. *J. Am. Chem. Soc.* **2002**, *124*, 14856.

(82) Guo, T.; Nikolaev, P.; Rinzler, A. G.; Tomanek, D.; Colbert, D. T.; Smalley, R. E. *J. Phys. Chem.* **1995**, *99*, 10694.

(83) Geohegan, D. B.; Schittenhelm, H.; Fan, X.; Pennycook, S. J.; Puretzky, A. A.; Guillorn, M. A.; Blom, D. A.; Joy, D. C. *Appl. Phys. Lett.* **2001**, *78*, 3307.

(84) Puretzky, A. A.; Geohegan, D. B.; Schittenhelm, C. H.; Fan, X.; Guillorn, M. A. *Appl. Surface Sci.* **2002**, *197-198*, 552.

(85) Scott, C. D.; Arepalli, S.; Nikolaev, P.; Smalley, R. E. *Appl. Phys. A.* **2002**, *74*, 11.

(86) Dresselhaus, M. S. *Nature* **1998**, *391*, 19.

(87) Itkis, M. E.; Perea, D. E.; Niyogi, S.; Rickard, S. M.; Hamon, M. A.; Hu, H.; Zaho, B.; Haddon, R. C. *Nano Lett.* **2003**, *3*, 309.

(88) Alvarez, L.; Righi, A.; Guillard, T.; Rols, S.; Anglaret, E.; Laplaze, D.; Sauvajol, J. L. *Chem. Phys. Lett.* **2000**, *316*, 186.

(89) Kurti, J.; Zolyomi, V.; Gruneis, A.; Kuzmany, H. *Phys. Rev. B* **2002**, *65*, 165433.

(90) Jorio, A.; Saito, R.; Hafner, J. H.; Lieber, C. M.; Hunter, M.; McClure, T.; Dresselhaus, G.; Dresselhaus, M. S. *Phys. Rev. Lett.* **2001**, *86*, 1118.

(91) Dresselhaus, M. S.; Dresselhaus, G.; Jorio, A.; Souza Filho, A. G.; Saito, R. *Carbon* **2002**, *40*, 2043.

(92) Saito, R.; Grueneis, A.; Cancado, L. G.; Pimenta, M. A.; Jorio, A.; Souza Filho, A. G.; Dresselhaus, G.; Dresselhaus, M. S. In *Mater. Res. Soc. Symp. Proc.*, 2002; Vol. 706, p paper Z9.3.1.

(93) Tuinstra, F.; Koenig, J. L. *J. Chem. Phys.* **1970**, *53*, 1126.

(94) Saito, R.; Takeya, T.; Kimura, T.; Dresselhaus, G.; Dresselhaus, M. S. *Phys. Rev. B* **1998**, *57*, 4145.

(95) Tang, X.-P.; Kleinhammes, A.; Shimoda, H.; Fleming, L.; Bennoune, K. Y.; Sinha, S.; Bower, C.; Zhou, O.; Wu, Y. *Science* **2000**, *288*, 492.

(96) Pichler, T.; Knupfer, M. S.; Golden, M. S.; Fink, J.; Rinzler, A. G.; Smalley, R. E. *Phys. Rev. Lett.* **1998**, *80*, 4729.

(97) Venema, L. C.; G., W. J. W.; Dekker, C.; Rinzler, A. G.; Smalley, R. E. *Appl. Phys. A.* **1998**, *66*, S153.